Development of a low-mass and high-efficient charged particle detector for $K_L \to \pi^0 \nu\bar{\nu}$ search

Daichi Naito

Department of Physics, Graduate School of Science, Kyoto University

April, 2016

Abstract

The KOTO experiment is a dedicated experiment to observe the $K_L \to \pi^0\nu\bar{\nu}$ decay, which is one of the powerful tools for new physics search. The KOTO experiment is designed to achieve the single event sensitivity of 8×10^{-12}, and the number of expected signal is ~ 4 assuming the branching ratio predicted in the Standard Model (SM). To achieve the sensitivity, the K_L decays including charged particles should be rejected. Since the K_L decay with charged particles occurs approximately 3×10^{10} times more frequently than the signal, we develop the Charged Veto detector (CV) to achieve high detection efficiency for the charged particles. The K_L beam contains a large number of neutrons, and neutrons in the beam halo produce a serious background by interacting with the CV. The CV is designed to remove the K_L decays with charged particles and to reduce the neutron interactions.

The CV has two separated layers of plastic scintillators with wavelength shifting fibers embedded and Multi Pixel Photon Counters for readout. The thickness of the scintillator is 3 mm, where amount of the materials is minimized in order to reduce neutron interaction. To reject the background from the K_L decays including charged particles with thin scintillators, small inefficiency, high light yield, and good timing resolution are essential, and each component of the CV is developed to satisfy the three requirements. Light yield, timing resolution, and inefficiency of the constructed CV are evaluated in the special experimental setup. To measure the inefficiency of the CV at the level of $O(10^{-5})$, the charged tracks are carefully chosen by the drift-chambers and the fine-segmented CsI electromagnetic calorimeter. The light yield is measured to be 18.6 p.e./100 keV, while the requirement is larger than 10 p.e. The timing resolution is 1.2 ns, while the requirement is smaller than 3 ns. The inefficiency per layer for charged particles is less than 1.5×10^{-5}, while the requirement is smaller than 10^{-3}. The CV achieves high efficiency, high light yield, and good timing resolution with thin scintillators, and satisfies all the requirements in the KOTO experiment.

By using the evaluated performance of the CV, we discuss $K_L \to \pi^0\nu\bar{\nu}$ search. We compare the numbers of the neutron backgrounds between the first physics run of KOTO and the final result of KEK-PS E391a that is the pilot experiment of KOTO. There are no background events in KOTO, and the number of neutron events is found to be 1/100 smaller than that in E391a at least. For the K_L decay with charged particles, the number of the background events is estimated with a Monte Carlo simulation where realistic detector response is implemented. The estimated number of signal events is 2.6, while that of background events from the K_L decay is 0.6. We confirm that the CV is built as designed and the number of backgrounds from the K_L decay with charged particles is suppressed enough to achieve the sensitivity of $K_L \to \pi^0\nu\bar{\nu}$ predicted in the SM.

Acknowledgements

Accomplishment of this thesis consisted of a great deal of help and support from a lot of people. I would like to express my gratitude to them on this occasion.

First of all, I would like to express my sincere appreciation to Prof. Noboru Sasao, for giving me a great opportunity for the research of the kaon physics and the development of a challenging detector. He gave me a chance to take the important role in it. I always respect his deep knowledge of physics and inexhaustible inquiring mind. His knowledge helped me many times. I would like to express heartfelt gratitude to Prof. Tadashi Nomura, and Prof. Hajime Nanjo. Advice through discussions with them was very important to improve the research. I would never have reached this successful end without their support. I would like to extend my gratitude to all of the KOTO collaborators. I am deeply thankful to Prof. T. Yamanaka, the spokesperson of the KOTO experiment. The installation of the CV was completed with his great support. His strong leadership carried this experiment here, and I believe he leads the experiment toward the great success. I would like to extend my appreciation to Prof. T. K. Komatsubara. I respect his great effort for the KOTO experiment. His advice for the analysis and the collection of English helped me many times. I present my appreciation to Prof. Gei Youb Lim, Prof. Hiroaki Watanabe, for their help in the installation of the CV and the environment preparation at J-PARC. The performance test of the CV was performed with their perfect arrangements. I would like to appreciate Prof. Yasuhisa Tajima. He always helped us in many experiments carried out at the ELPH, and prepared various things required in the experiments. I would like to appreciate Dr. Hideki Morihi and Prof. Takahiko Masuda. They have taught me physics and experimental methods from basic knowledge to technical issues. I am also thankful to Prof. M. Campbell, Prof. J.K. Ahn, Prof. S. Suzuki and Prof. Y. W. Wah for the advice and correction of the the prepublication paper. I am also thankful to Prof. T. Matsumura, Prof. M. Togawa for their advice and help in my research. I am also grateful to Prof. J. Comfort, Prof. M. Tecchio, Dr. J. Ma, Dr. D. McFarlan, Dr. J. Xu, and Mr. Y. Sugiyama for their great work for the complicated DAQ. My gratitude goes to Dr. Y. Ri, Dr. E. Iwai, Prof. T. Shimogawa, Dr. Y. C. Tung, Dr. K. Sato, Prof. K. Shiomi, Dr. J. W. Lee, and Mr. N. Kawasaki for giving me invaluable support and advice, and encouragement. My special thanks to Mr. Y. Maeda for his contribution of the development of the CV and joint work for the production and construction of the

CV. I would like to express my gratitude to Ms. M. Sasaki, Mr. G. Takahashi, Mr. S. Seki, and Mr. T. Hineno for their great contributions to the beam test and the installation of the CV. I would like to express my gratitude to Ms. R. Murayama, Mr. Y. Nakaya, Ms. Y. Yanagida, Mr. Y. Odani, Mr. H. Yokota, Mr. T. Ota, Mr. S. Banno, Mr. T. Toyoda, Mr Takashima, Ms. M. Isoe, Mr. I. Kamiji, Mr. K. Nakagiri , and Mr. S. Shinohara for their past and future great work for the KOTO experiment. I am deeply grateful to all the members of the High Energy Physics Group in Kyoto University. Prof. T. Nakaya, Prof. A. K. Ichikawa, Prof. M. Ishino, Prof. A. Minamino, Prof. T. Sumida, Prof. M. Ikeda, Dr. K. Nitta, Dr. C. Bronner, Dr. P. Litchfield, Dr. K. MAHN, Dr. P. Nikhul, Dr. C. V. Son, Dr. B. Quilain, Dr. K. Nakamura, Prof. N. Taniguchi, Prof. K. Hiraide, Prof. Y. Kurimoto, Dr. Y. Nakajima, Prof. K. Matsuoka, Mr. H. Kubo, Mr. T. Usuki, Mr. N. Nagai, Dr. M. Otani, Dr. K. Ieki, Dr. A. Murakami, Dr. T. Kikawa, Dr. K. Suzuki, Mr. S. Takahashi, Mr. K Huang, Mr. T. Hiraki, Ms. S. Hirota, Mr. T. Yamauchi, Mr. K. Goda, Mr. T. Tashiro, Mr. T. Nagasaki, Mr. S. Akiyama, Mr. N. Kamo, Mr. K. Tateishi, Mr. Y. Ishiyama, Mr. T. Kunigo, Mr. M. Jiang, Mr. K. Nakamura, Mr. T. Hayashino, Mr. K. Yoshida, Mr. K. Kondo, Mr. K. Haneda, Mr. S. Ban, Ms. M. Yamamoto, Mr. R. Monden, Ms. S. Yanagita, Mr. S. Akatsuka, Mr Y. Ashida, Mr. S. Tanaka, Ms. Y. Nakanishi, Mr. Y. Noguchi, and Ms. A. Hiramoto. My life in the university have been always happy with them. At last but not the least, I would like to express my special appreciation to my parents for the infinite supports throughout my life.

Daichi Naito
Kyoto, Japan.
April, 2016

Contents

Chapter 1

Introduction

An imbalance between matter and antimatter in our universe is one of the big questions in the modern physics. The imbalance requires a violation of CP symmetry which is the symmetry between matter and anti-matter [1]. One mechanism of the CP violation is implemented in the Standard Model (SM) of the elementary particle physics. The source of the CP violation comes from a complex phase in the Cabibbo-Kobayashi-Maskawa matrix (CKM) which governs mixing between quarks [2]. The amplitude of the CP violation in the SM is too small to explain the imbalance [3]. We need an additional CP-violating process.

Various experiments were carried out in order to verify the SM precisely or to search for new physics. The E391a experiment [4], the KTeV experiment [5], and the E949 experiment [6] were carried out by using kaon decays, and any anomaly was not observed. We are performing the KOTO experiment to search for new physics with higher sensitivity. The goal of KOTO is to observe the $K_L \to \pi^0 \nu\bar{\nu}$ decay for the first time. This decay is a rare direct CP-violating decay process with a small theoretical uncertainty in the calculation of the branching ratio. The branching ratio of the decay is sensitive to new physics beyond the SM. Some new physics models predict a larger branching ratio than that in the SM [7]. To achieve the sensitivity of 3.0×10^{-11} [8] (the SM prediction), we upgrade the detector from the former pilot-experiment of E391a which sets the current upper limit of 1.4×10^{-9} [4], and we use a high intensity kaon beam at J-PARC [9].

1.1 CP violation in the SM

The mass eigen-states are not equal to the weak eigen-states in the quark sector of the SM. The relation between the two eigen-states are described,

$$\begin{pmatrix} d' \\ s' \\ b' \end{pmatrix} = \begin{pmatrix} V_{ud} & V_{us} & V_{ub} \\ V_{cd} & V_{cs} & V_{cb} \\ V_{td} & V_{ts} & V_{tb} \end{pmatrix} \begin{pmatrix} d \\ s \\ b \end{pmatrix} = V_{CKM} \begin{pmatrix} d \\ s \\ b \end{pmatrix}. \tag{1.1}$$

Here, d', s' , b' are the weak eigen-states, and d, s, b are the mass eigen-states. V_{ij} is an element of the CKM matrix (V_{CKM}). In the Wolfenstein parameterization, V_{CKM} is described with four parameters, λ, A, ρ, and η which represents the complex phase causing the CP violation [10],

$$V_{CKM} = \begin{pmatrix} 1 - \frac{1}{2}\lambda^2 & \lambda & A\lambda^3(\rho - i\eta) \\ -\lambda & 1 - \frac{1}{2}\lambda^2 & A\lambda^2 \\ A\lambda^3(1 - \rho - i\eta) & -A\lambda^2 & 1 \end{pmatrix} + O(\lambda^4). \tag{1.2}$$

In the SM, the CP violation arises through the parameter η, and η is found to be non zero [11].

1.2 $K_L \to \pi^0 \nu\bar{\nu}$

1.2.1 $K_L \to \pi^0 \nu\bar{\nu}$ in the SM

The $K_L \to \pi^0 \nu\bar{\nu}$ decay is the rare decay that directly violates CP symmetry. This decay is a flavor changing neutral current (FCNC) process, and is prohibited at the tree level interaction. The $K_L \to \pi^0 \nu\bar{\nu}$ decay occurs through loop diagrams and box diagrams as shown in Fig. 1.2.1. The diagrams are dominated by the contribution of the top quark, only which has a complex phase: the decay amplitude is proportional to $A(K^0 \to \pi^0 \nu\bar{\nu}) - A(\bar{K^0} \to \pi^0 \nu\bar{\nu})$ since $|K_L\rangle \approx (|K^0\rangle - |\bar{K^0}\rangle)/\sqrt{2}$, and other contributions of the quarks are canceled. The charm contribution is hence below 1 % in the calculation of the branching ratio. On the other hand, the contribution of the $\mathrm{Im}(\mathrm{V}_{ts}^* \mathrm{V}_{td})$ is dominant in the calculation of branching ratio because of the heavy mass of the top quark. The branching ratio of $K_L \to \pi^0 \nu\bar{\nu}$ is then written as,

$$\mathrm{Br}(K_L \to \pi^0 \nu\bar{\nu}) = \kappa_L \left(\frac{\mathrm{Im}(\mathrm{V}_{ts}^* \mathrm{V}_{td})}{\lambda^5} X_t \right)^2. \tag{1.3}$$

Here, the coefficient κ_L is relevant to the hadronic matrix element [12], and the function X_t is described with $x = m_t^2/M_W^2$ [13]. Here, m_t shows the mass of the top quark and M_W show the mass of the week boson. In the Wolfenstein parameterization, $\mathrm{Im}(\mathrm{V}_{ts}^* \mathrm{V}_{td})$ is calculated to be

$$\mathrm{Im}(\mathrm{V}_{ts}^* \mathrm{V}_{td}) \simeq A^2 \lambda^5 \eta. \tag{1.4}$$

The branching ratio is proportional to η^2. We then examine the amplitude of the CP violation by measuring the branching ratio. By using the currently obtained values of the CKM parameters, the $\mathrm{Br}(K_L \to \pi^0 \nu\bar{\nu})$ is predicted to be [8]

$$\mathrm{Br}(K_L \to \pi^0 \nu\bar{\nu}) = (3.0 \pm 0.3) \times 10^{-11}. \tag{1.5}$$

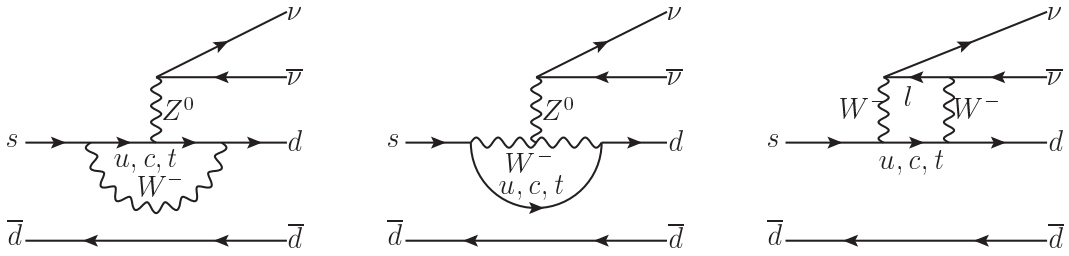

Figure 1.2.1: Feynman diagrams of the $K_L \to \pi^0 \nu\bar{\nu}$ decay.

1.2.2 Grossman-Nir limit

The $K_L \to \pi^0 \nu\bar{\nu}$ decay is strongly related to the $K^+ \to \pi^+ \nu\bar{\nu}$ decay from the information of the isospin symmetry. The upper limit to the $K_L \to \pi^0 \nu\bar{\nu}$ decay from this relation is called "Grossman-Nir (GN) limit ", and is described in the following equation [14].

$$\mathrm{Br}(K_L \to \pi^0 \nu\bar{\nu}) \leq 4.4 \times \mathrm{Br}(K^+ \to \pi^+ \nu\bar{\nu}). \tag{1.6}$$

The branching ratio of $K^+ \to \pi^+ \nu\bar{\nu}$ measured by the E949 experiment [6] is

$$\mathrm{Br}(K^+ \to \pi^+ \nu\bar{\nu}) = 14.7^{+13.0}_{-8.9} \times 10^{-11}. \tag{1.7}$$

The upper limit to the $K^+ \to \pi^+ \nu\bar{\nu}$ decay is 3.2×10^{-10} (90% C. L.) [6], and the upper limit to the $K_L \to \pi^0 \nu\bar{\nu}$ decay is

$$\mathrm{Br}(K_L \to \pi^0 \nu\bar{\nu}) < 1.4 \times 10^{-9} \text{ (90\% C. L.)}. \tag{1.8}$$

1.2.3 $K_L \to \pi^0 \nu\bar{\nu}$ beyond the SM

Several new physics beyond the SM (BSM) predict a bigger branching ratio than that in the SM. Figure 1.2.2 shows the predicted correlation between $\mathrm{Br}(K_L \to \pi^0 \nu\bar{\nu})$ and $\mathrm{Br}(K^+ \to \pi^+ \nu\bar{\nu})$ in the BSM [15]. We introduce a brief summary of the BSM.

Littlest Higgs Model with T-Parity (LHT) [16][17] New charged heavy vector bosons ($W_H^{\pm}$), a neutral heavy vector boson (Z_H^0), a heavy photon (A_H), a heavy top quark (T^+), and a triplet of scalar heavy particles (ϕ) are present. This model also requires the introduction of three doublets of "mirror quarks" and three doublets of "mirror leptons". The new particles contribute to the branching ratio of $K_L \to \pi^0 \nu\bar{\nu}$.

Randall-Sundrum model with custodial protection (RSc) [18] This model introduces the heavy neutral gauge bosons Z_H and Z' which contain new flavor violating interactions. The new particles contribute to the branching ratio of $K_L \to \pi^0 \nu\bar{\nu}$.

Sequential fourth generation (SM4) [19] A sequential fourth generation of quarks and leptons are introduced. This new generation of quarks has mixing with other quarks, and new CP phases are generated.

Minimal Flavor Violation (MFV) [20] This model does not introduce any new CP violation beyond the CKM phase, and a flavor of quarks and CP-violating interactions are linked to the known structure of Yukawa couplings. The contribution to the branching ratio in $K_L \to \pi^0 \nu\bar{\nu}$ is simply given by a real part of a function within the parenthesis in Eq. 1.3.

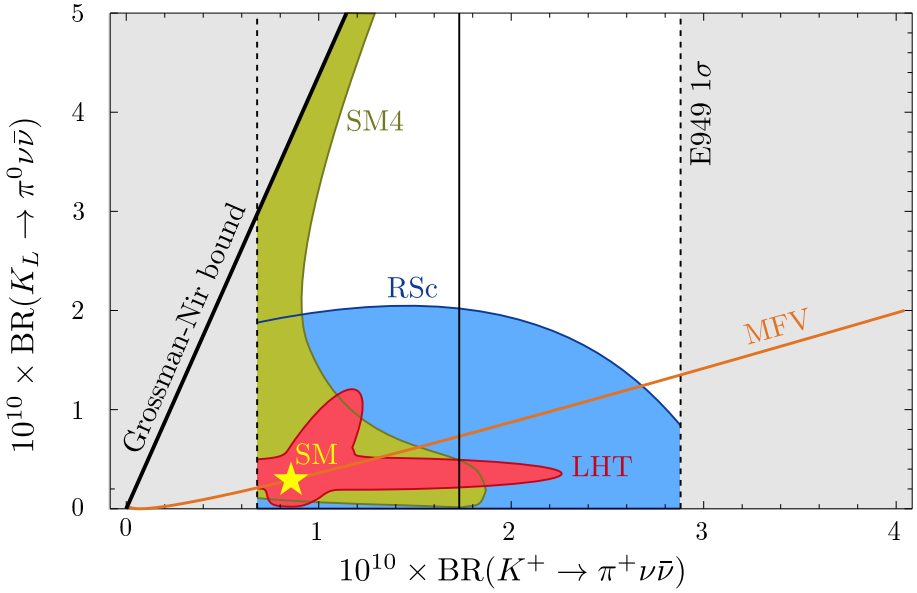

Figure 1.2.2: The predicted correlation between $\mathrm{Br}(K_L \to \pi^0 \nu\bar{\nu})$ and $\mathrm{Br}(K^+ \to \pi^+ \nu\bar{\nu})$ in the BSM [15].

Next, we discuss an advantage of $K_L \to \pi^0 \nu\bar{\nu}$ over other rare decays. In the FCNC process including

$K_L \to \pi^0\nu\bar{\nu}$, the matrix elements related to the top quark in the CKM matrix are dominant source of CP violation [21], and have the hierarchy described as the following,

$$|V_{ts}^* V_{td}| \sim 5 \times 10^{-4} \ll |V_{tb}^* V_{td}| \sim 10^{-2} < |V_{tb}^* V_{ts}| \sim 4 \times 10^{-2}. \tag{1.9}$$

A transition from the s quark to the d quark is much suppressed than other transitions in the SM. $K_L \to \pi^0\nu\bar{\nu}$ can still have large anomaly in the branching ratio if the amplitude of the CP violation in new physics is small and any anomaly is not observed in other rear decays.

1.2.4 History of the search for the $K_L \to \pi^0\nu\bar{\nu}$

The history of the search for the $K_L \to \pi^0\nu\bar{\nu}$ decay is shown in Fig. 1.2.3. The vertical axis shows the upper limit of the $K_L \to \pi^0\nu\bar{\nu}$ decay at 90% C.L. The green point shows the indirect limit by using the $K_L \to 2\pi^0$ study [22]. The red points shows the direct limit by using the $\pi^0 \to \gamma\gamma$ decay for the identification of this decay. The blue points shows the direct limit by using the $\pi^0 \to e^+e^-\gamma$ decay. The $K_L \to \pi^0\nu\bar{\nu}$ is not observed yet since the Br($K_L \to \pi^0\nu\bar{\nu}$) is very small. The current upper limit is set by E391a to be [4]

$$\mathrm{Br}(K_L \to \pi^0\nu\bar{\nu}) < 2.6 \times 10^{-8} \text{ (90\% C. L.)}. \tag{1.10}$$

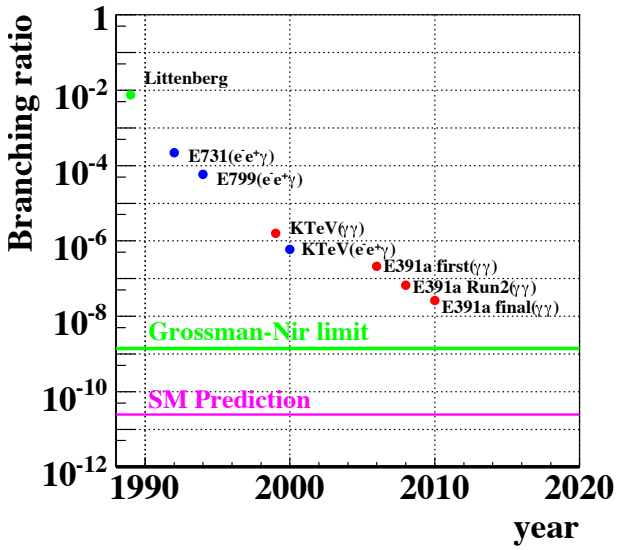

Figure 1.2.3: History of the search for the $K_L \to \pi^0\nu\bar{\nu}$ decay.

1.3 Goal of the KOTO experiment

The KOTO experiment [23] is an experiment dedicated to observing the $K_L \to \pi^0\nu\bar{\nu}$ decay for the first time by using an intense kaon beam at the Japan Proton Accelerator Research Complex (J-PARC) [9]. We construct the KOTO detector, and it is the upgraded detector of KEK-PS E391a which is the pilot experiment for KOTO. The KOTO experiment is designed to achieve the single event sensitivity of 8×10^{-12} [24], and the number of expected signal is $\sim$4 assuming the branching ratio in the SM. We examine the amplitude of the CP violation in the SM by measuring the branching ratio. We also examine new physics introduced in Sec. 1.2.3. When we observe $K_L \to \pi^0\nu\bar{\nu}$ with greater branching ratio than the predicted one in the SM, we confirm that the BSM exists. It is a key to access to resolve the imbalance between matter and antimatter in our universe.

1.4 Outline of this thesis

To achieve the sensitivity of $K_L \to \pi^0\nu\bar{\nu}$ predicted in the SM, the K_L decays including charged particles should be rejected. Since the K_L decay with charged particles occurs approximately 3×10^{10} times more frequently than the signal, we develop the Charged Veto detector (CV) to achieve high detection efficiency for the charged particles. We perform a test experiment to measure the detection efficiency of the CV for charged particles before its installation in the KOTO experiment. In this thesis, we report the test result and the expected performance of the CV in the KOTO experiment in the following structure.

In Chapt. 1, we have explained the motivation of the KOTO experiment to search for $K_L \to \pi^0\nu\bar{\nu}$.

In Chapt. 2, the experimental principle of the KOTO experiment and the special setup for the CV test are introduced. The identification of $K_L \to \pi^0\nu\bar{\nu}$ and the rejection method of backgrounds are presented. In the CV test, the K_L beam is used since high statistics is needed to measure the inefficiency of the CV at the level of $O(10^{-5})$. The K_L beam is also useful to avoid mis-reconstruction of charged tracks since the number of charged particles from K_L decays is limited as two and reconstruction of two tracks is further constrained than that of single track. The charged tracks are carefully chosen by using drift-chambers and a fine-segmented CsI electromagnetic calorimeter. Experimental components and a data acquisition system are introduced.

In Chapt. 3, the design principle of the CV and the requirements for the performance evaluated in the CV test are described. The K_L beam contains a large number of neutrons, and neutrons in the beam halo produce a serious background by interacting with the CV. The CV is designed to remove the K_L decays with charged particles and to reduce the neutron interactions. The CV has two separated layers of plastic scintillators with wavelength shifting fibers embedded and Multi Pixel Photon Counters for readout. The thickness of the scintillator is 3 mm, where amount of the materials is minimized in order

to reduce neutron interaction. To reject the background from the K_L decays including charged particles with thin scintillators, small inefficiency, high light yield, and good timing resolution are essential, and we estimate requirements.

In Chapt. 4 and 5, the design of the CV, and development of each component of the CV to satisfy the requirements are presented. In Chapt. 4, the actual structure of the CV is described. In Chapt. 5, the readout system for the CV is described.

In Chapt. 6, the basic performance of the CV, light yield and timing resolution are studied by using the special setup described in Chapt. 2. The high statistics obtained from the K_L beam enable us to measure the position dependence of the light yield and the timing resolution. By using a simulation developed with the measured detector response, we correct the measured inefficiency of the CV. We confirm that the CV achieves very high efficiency, high light yield, and good timing resolution for the charged particles with thin scintillators, and satisfies the requirements for the KOTO experiment.

In Chapt. 7, we discuss the sensitivity of $K_L \to \pi^0 \nu\bar{\nu}$ search with background study in a simulation. We compare the numbers of the neutron backgrounds between the first physics run of KOTO and the final result of KEK-PS E391a that is the pilot experiment of KOTO. For the K_L decay with charged particles, the number of the background events is estimated with a Monte Carlo simulation where realistic detector response is implemented. We confirm that the CV is built as designed and the number of backgrounds from the K_L decay with charged particles is suppressed enough to achieve the sensitivity of $K_L \to \pi^0 \nu\bar{\nu}$ predicted in the SM.

Chapter 2

The KOTO experiment

The signal detection in the KOTO experiment is first introduced. Then, experimental apparatus related to the test of the Charged Veto is described.

2.1 Signal detection

The principle of the KOTO experiment and the KOTO detector are first introduced. Second, the signal reconstruction and indentification are explained. Third, the numbers of signals and backgrounds in KOTO are described.

2.1.1 Experimental Principle and the KOTO detector

The signature of the $K_L \to \pi^0\nu\bar{\nu}$ decay is two photons from a π^0 decay with no other particles detected [1)]. To identify this state, we prepare the KOTO detector as shown in Fig. 2.1.1. Black lines surrounding detectors from z = -200 mm to z = 8500 mm indicate a cylindrical vacuum chamber. We search for the $K_L \to \pi^0\nu\bar{\nu}$ decay in flight that occurs in the central region of the vacuum chamber. The "CsI" in Fig. 2.1.1 indicates a CsI calorimeter, and it is used to measure the position and energy of two photons from the π^0. The position and energy are used to reconstruct and identify the π^0 from $K_L \to \pi^0\nu\bar{\nu}$ as explained in Sec. 2.1.2. Other detectors in Fig. 2.1.1 are the hermetic neutral and charged particle detectors (veto detectors) surrounding the decay region in order to ensure that no other particles exist. Energy deposit of veto detectors are checked in a time span of several tens of ns (veto window) when the π^0 is reconstructed in the calorimeter. Table 2.1.1 shows the function and components of veto detectors. The "CV" in Fig. 2.1.1 and Table 2.1.1 is the charged particle counter that we develop in this thesis.

[1)] A neutrino cannot be detected because of its small cross section.

In Fig. 2.1.1, the vertical axis shows y axis, the horizontal axis shows z axis. The origin of the xy plane is center of the cylindrical vacuum chamber. The origin of z is the upstream surface of Front Barrel Photon Detector (FB) as shown in Fig. 2.1.1. The definition of the coordinate is used in this thesis.

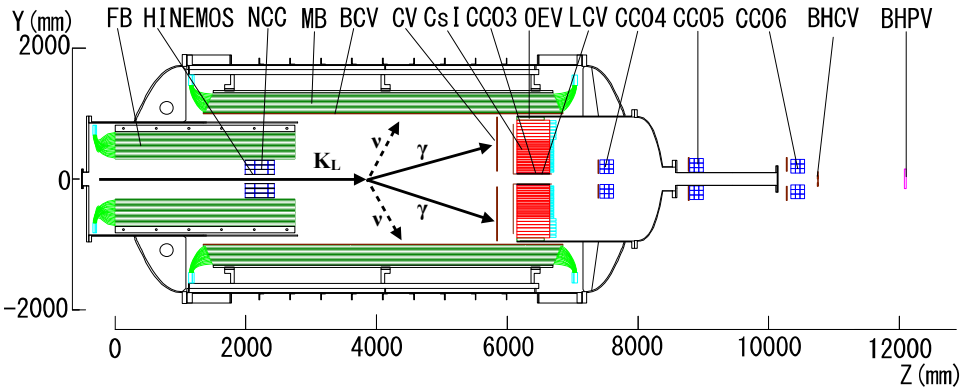

Figure 2.1.1: Cross sectional view of the KOTO detector. The name of each detector is explained in Table. 2.1.1. Most of detectors, including the CV, are installed in a cylindrical vacuum chamber.

Table 2.1.1: Components of the KOTO detector with the functions.

Detector Name	Function	detector components
Front Barrel (FB)	gamma veto	sandwich (lead and plastic scintillator)
HINEMOS	charged veto	plastic scintillator
Neutron Color Counter (NCC)	gamma veto	CsI crystal
Main Barrel (MB)	gamma veto	sandwich (lead and plastic scintillator)
Barrel Charged Veto (BCV)	charged veto	plastic scintillator
Charged Veto (CV)	charged veto	plastic scintillator
Color Counter 03 (CC03)	gamma veto	CsI crystal
Outer Edge Veto (OEV)	gamma veto	sandwich (lead and plastic scintillator)
Liner Charged Veto (LCV)	charged veto	plastic scintillator
Color Counter 04 (CC04)	gamma veto	plastic scintillator + CsI crystal
Color Counter 05 (CC05)	gamma veto	plastic scintillator + CsI crystal
Color Counter 06 (CC06)	gamma veto	plastic scintillator + CsI crystal
Beam Hole Charged Veto (BHCV)	charged veto	plastic scintillator
Beam Hole Photon Veto (BHPV)	gamma veto	lead converter + aerogel

2.1.2 Reconstruction and identification of the signal

We reconstruct a π^0 by assuming $\pi^0 \to 2\gamma$ to identify the π^0 from $K_L \to \pi^0\nu\bar{\nu}$. Since it is difficult to reconstruct a π^0 only from the positions and the energy of two photons, we assume that the vertex position of a π^0 is on the z axis. To satisfy the assumption of the vertex position, the K_L beam is shaped to be narrow with a beamline as mentioned in Sec. 2.2, and the kinematics of the π^0 is shown as Fig. 2.1.2. In this figure, the square shows xy plane on the surface of the calorimeter whose z position is Z_{CsI}. E_1 and E_2 are the energy of two photons measured by the calorimeter. R_1 and R_2 are the distance from the beam center to the hit position of each photon measured by the calorimeter. R_{12} is the distance between the hit positions of the two photons. θ is an opening angle between two photons from the decay-vertex position of the π^0 whose z position is Z_{vtx}. θ and Z_{vtx} are calculated by using the mass of π^0 (M_π), conservation of the four-momentum, and geometric relations as described in the following equations.

$$M_\pi^2 = 2E_1E_2(1-\cos\theta) \tag{2.1}$$

$$R_{12}^2 = d_1^2 + d_2^2 - 2d_1d_2\cos\theta \tag{2.2}$$

$$d_1 = \sqrt{R_1^2 + (Z_{CsI} - Z_{vtx})^2} \tag{2.3}$$

$$d_2 = \sqrt{R_2^2 + (Z_{CsI} - Z_{vtx})^2} \tag{2.4}$$

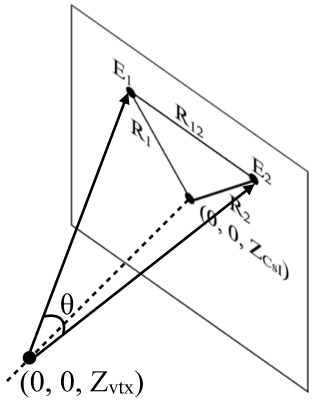

Figure 2.1.2: Kinematics of the π^0.

Z_{vtx} is used to ensure that the $K_L \to \pi^0\nu\bar{\nu}$ decay occurs in the central region of the vacuum chamber, and to reduce backgrounds by the interaction between neutrons and veto detectors. The events become background when the neutrons surrounding the K_L beam (halo neutron) hit veto detectors and generate π^0 or η. To reduce the background, we reject events in which Z_{vtx} is reconstructed near veto detectors.

In this thesis, the allowed region is set from 3000 mm to 5000 mm.

The transverse momentum of π^0 (P_t) is calculated from θ, E_i, R_i and Z_{vtx}. P_t is used to reject the reconstructed π^0 from $K_L \to 2\gamma$ and $K_L \to \pi^+\pi^-\pi^0$ whose kinematic limit of P_t is different from that of $K_L \to \pi^0\nu\bar{\nu}$. P_t of the reconstructed π^0 from $K_L \to 2\gamma$ is ≈ 0 since it occurs back-to-back. P_t of the π^0 from $K_L \to \pi^+\pi^-\pi^0$ is kinematically limited to be less than 133 MeV/c. On the other hand, P_t of the π^0 from $K_L \to \pi^0\nu\bar{\nu}$ tends to be larger than that from other decay modes because of the missing momentum of 2 neutrinos, and is kinematically limited to be less than 231 MeV/c. In this thesis, the allowed region of P_t is set from 140 to 250 MeV/c.

2.1.3 Signals and Backgrounds

The expected numbers of signals and backgrounds with the sensitivity of 1.0×10^{-11} [25] are shown in Table 2.1.2[2)]. The branching ratio of each decay mode is also shown. The $K_L \to 2\pi^0$ decay becomes background when only two of four photons are detected by the calorimeter and other photons are not detected by any veto detectors. The number of background by $K_L \to 2\pi^0$ is expected to be less than 0.3 [26] after the installation of a new detector which is located in the inner region of Main Barrel (MB) as shown in Fig. 2.1.1[3)]. Other backgrounds are described in Chap. 3 since they are related to the design and requirements of the CV. The number of all the backgrounds will be suppressed, and KOTO achieves the sensitivity of $K_L \to \pi^0\nu\bar{\nu}$ predicted in the Standard Model of particle physics (SM).

Table 2.1.2: Expected signals and backgrounds [25].

Decay Mode	branching ratio	value
$K_L \to 2\pi^0$	9×10^{-4}	1.32±0.04
$K_L \to \pi^\pm\pi^\mp\pi^0$	13 %	0.11±0.11
$K_L \to \pi^\pm e^\mp \nu_e$	41 %	0.07±0.04
Halo neutron	–	0.10±0.05
$K_L \to \pi^0\nu\bar{\nu}$	2.4×10^{-11}	2.39 ±0.03

2.2 J-PARC accelerator and KL beamline

The K_L beam is generated by using 30-GeV protons from J-PARC and KL beamline.

[2)] In this analysis, a previous value, 2.4×10^{-11} is used as the branching ratio of $K_L \to \pi^0\nu\bar{\nu}$, while the current ratio is 3×10^{-11} as described in Sec. 1.2.1.

[3)] The new detector will be installed in April 2016.

J-PARC accelerator

The accelerator complex of J-PARC is shown in Fig.2.2.1. The J-PARC accelerator consists of three components: a linear accelerator (LINAC), a rapid-cycling synchrotron (RCS), and a main ring synchrotron (MR). Protons are accelerated up to 30 GeV in the MR. The protons are then extracted from the MR to the Hadron Experimental Facility (HEF).

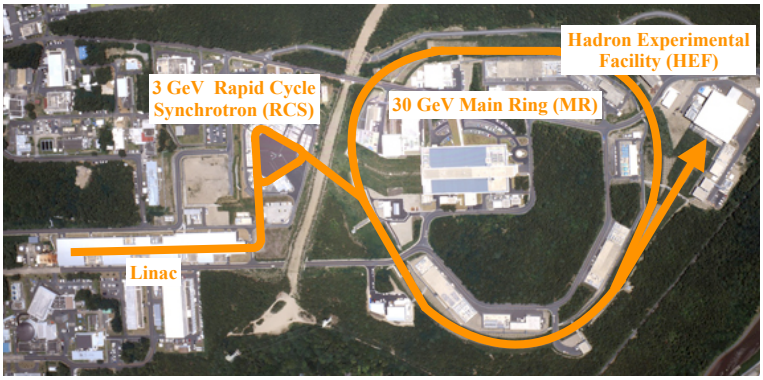

Figure 2.2.1: Photo of J-PARC. This photo is obtained from [9].

KL beamline

The primary T1 target and the KL beamline are installed in the HEF as shown in Fig. 2.2.2 [27]. In this figure, the extracted protons hit the T1 target, and secondary particles are generated. Table 2.2.1 shows the material of the target and the period in which each target is used. In the downstream of the target, the KL beamline is located at 16° with respect to the primary proton beam. From the exit of the beamline, the KOTO experimental area is prepared with the KOTO detector. In Fig. 2.2.2, the KL beamline is shown, where the photon absorber, the sweeping magnet, and the two long collimators are illustrated. The photon absorber reduces the number of gammas. The sweeping magnet eliminates charged particles. Short-lived particles (e.g. K_S, hyperons) are eliminated by the decay in flight through the long beam line. The shape of the collimators is designed to make a small diameter beam and to minimize the halo neutron flux.

- To satisfy the assumption of the vertex position, the K_L beam should be shaped into a small diameter beam.
- As mentioned in Sec 2.1.2, the halo neutron makes a background event. The halo neutron flux should be minimized.

At the exit of the collimator, the solid angle of the $K_{\rm L}$ beam is 7.6 μsr, and the size of the $K_{\rm L}$ beam is 8.5 cm $\times$ 8.5 cm. The flux of the K_L is measured to be 4.2×10^7 per 2.0×10^{14} protons on target (POT) [28], and the K_L momentum is measured as shown in Fig. 2.2.3 [29]. The result obtained from the reconstruction of $K_L \to \pi^+\pi^-$ (red points) and from the reconstruction of $K_L \to \pi^+\pi^-\pi^0$ (green points), and the combined result of the two spectra (black points) are shown. We use the combined result as the momentum distribution of the K_L. The number of halo neutron is expected to be 1×10^4 per 2.0×10^{14} POT from a simulation [27]. The shape of the K_L beam and the neutron flux are input to a simulation, and we obtain the results as shown in Table 2.1.2. With the design of the KL beamline, the number of expected signal is enough large and that of backgrounds are low to achieve the sensitivity of $K_L \to \pi^0\nu\bar{\nu}$ predicted in the SM.

Table 2.2.1: Summary of the T1 target.

Period	Target Material
Jan. 2012-Jul. 2012	Pt square-bar
Apr. 2015-	Au square-bar
Design	Ni disks

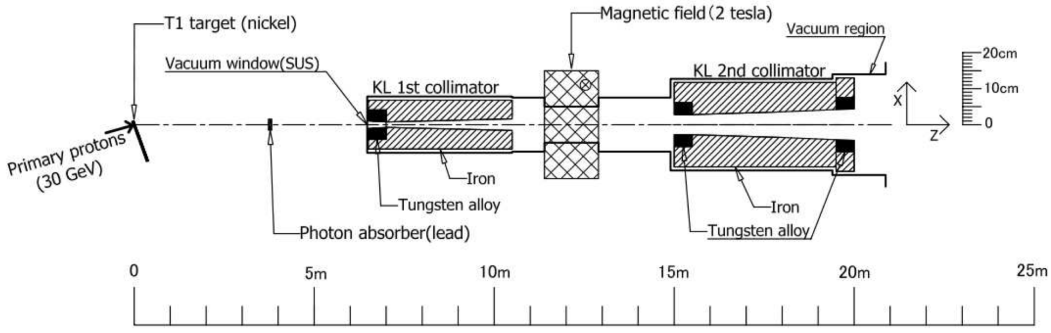

Figure 2.2.2: Cross sectional view of the primary T1 target and the KL beamline [27].

2.3 Experimental setup for the test of the Charged Veto

The test of the CV is the special experiment carried out in the KOTO experimental area before the installation of the KOTO detector, and is shown in Fig. 2.3.1. We use the KL beamline that is the same as used in the KOTO experiment[4)]. From upstream to downstream of the KOTO experimental area,

[4)]The test experiment of the CV is performed with Pt target as described in Table 2.2.1.

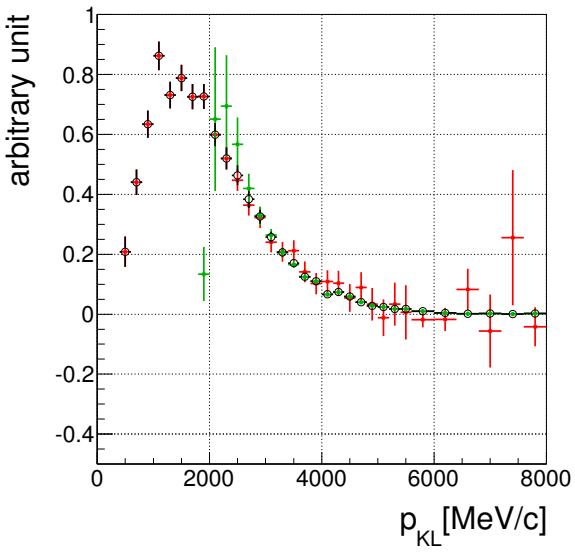

Figure 2.2.3: The observed K_L momentum at the exit of the KL beamline [29]. Red points show the result obtained from $K_L \to \pi^+\pi^-$. Green points show the result obtained from $K_L \to \pi^+\pi^-\pi^0$. Black points show the combined result of the two spectra.

three drift chambers (DC1, DC2, DC3), the CV, a hodoscope and the calorimeter are placed[5)]. All the detectors are located under the atmospheric pressure[6)]. The K_L beam is produced by the KL beamline, and we reconstruct straight tracks of charged particles from K_L decays by the drift chambers and the hodoscope. The CV and the calorimeter in Fig. 2.3.1 are the same as used in the KOTO experiment. The CV is described in Chap. 4 and Chap. 5, and the calorimeter is described in the following paragraph. The drift chambers and the hodoscope are prepared for the test of the CV, and described in the following paragraphs.[7)]. The trigger and DAQ system are also described.

CsI calorimeter The calorimeter consists of two kinds of un-doped CsI crystal as shown in Fig. 2.3.2: one is 2240 small CsI crystals, and the other is 476 large CsI crystals. The cross section of the small crystal is 2.5×2.5 cm^2, and that of the large crystal is 5×5 cm^2. The length of each crystal in the z direction is 50 cm (27 X_0). The Moriere radius of CsI with the electromagnetic shower is 35.7 mm [30], and it is large enough to make multiple hits in the calorimeter. These multiple hits are clustered. Its energy deposit, hit position, and hit timing are reconstructed. A detail of the forming cluster and the reconstruction are described in the reference [28]. To identify the electromagnetic shower, the hit pattern

[5)]Distance between the calorimeter and the front or rear CV is not same as it in the normal KOTO experiment to put in the hodoscope.

[6)]In KOTO, most of the detectors, including the CV and the calorimeter, are locate in vacuum.

[7)]There are another four components, beam plug, spectrometer magnet, dry room, and CsI cover. They are described in the reference [29].

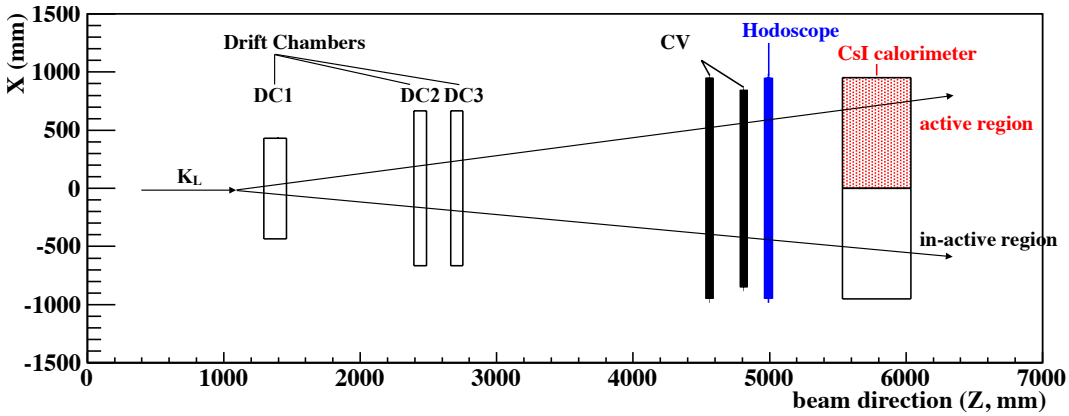

Figure 2.3.1: Setup of the special experiment at the KL beamline.

of each cluster is used as shown in App.A. Waveform of the calorimeter is recorded by the 125 MHz ADC dsecribed in Sec. 5.2.

In the test of the CV, the multiple hits are clustered with another method as described in Sec. 6.1.1. A part of the calorimeter is active as shown with red in Fig. 2.3.2[8)].

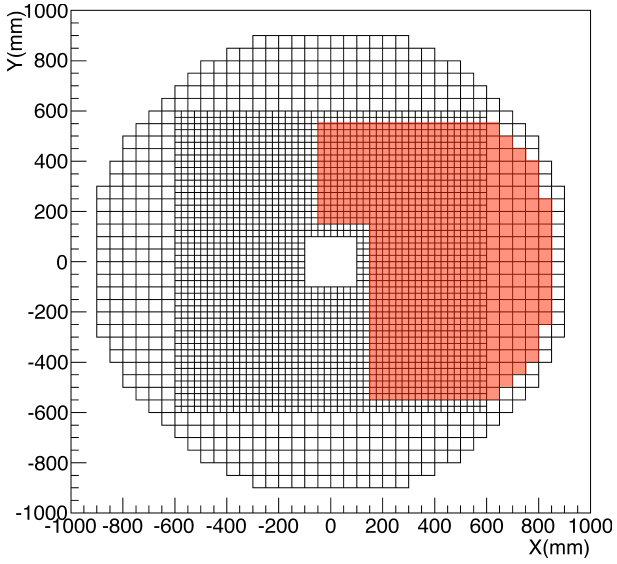

Figure 2.3.2: Rear view of the calorimeter. The two sizes of squares in the array show the small and large CsI crystals in the calorimeter. Red region shows active area of the calorimeter in the test of the CV.

[8)]The installation of PMTs is not completed in other area

Drift chambers Three drift chambers are used for tracking. Table 2.3.1 shows characteristics of the chambers. All the chambers have four sense-wire planes, y, y', x, and x'[9]. The y and y' (or x and x') wires are parallel, and staggered by a half wire spacing. A signal from each sense wire of the drift chambers is readout by a Time-to-Digital converter module (TDC).

Table 2.3.1: Characteristics of chambers.

	DC1	DC2	DC3
plane	X,X',Y,Y'	X,X',Y	X,X',Y,Y'
effective area	715×430	1186×898	1186×898
wire space	5 mm	4.5 mm	4.5 mm
cell type	hexagon	hexagon	hexagon
gas (1:1)	A_r+C_2H_6	A_r+C_2H_6	A_r+C_2H_6

Hodoscope The hodoscope is placed between the CV and the calorimeter to identify the charged particles. The hodoscope consists of twelve modules as shown in Fig. 2.3.3. One module consists of 4 or 5 plastic scintillator bars, and the dimension is 1-cm thick, 5-cm wide, and 112-cm long. The scintillating lights are collected with wavelength shifting (WLS) fibers[10], and all the fibers are bundled and readout with a PMT. Waveform of the hodoscope is recorded with the 125 MHz ADC.

Scintillator tracker To perform energy calibration of the calorimeter, five scintillators are put above and below the calorimeter to track cosmic-ray muons as shown in Fig. 2.3.4.

Trigger and data acquisition The trigger is designed to collect two charged particles from K_L decays and the major decay processes are $K_L \to \pi^{\pm}e^{\mp}\nu$, $K_L \to \pi^{\pm}\mu^{\mp}\nu$, and $K_L \to \pi^{+}\pi^{-}\pi^{0}$. The trigger requests at least one hit in each quadrant of the two diagonal quadrants of the hodoscope as shown with blue and red in Fig. 2.3.5. When the hodoscope is triggered, the data taking for the chambers with the TDC is started. The data taking for other detectors is started when the hit multiplicity of the DC1 is more than two[11]. The trigger rate of the data acquisition system is $\sim$ 250 Hz. The data is taken for $\sim$ 3 weeks from June to July in 2012. The beam power of the J-PARC MR for delivery to HEF is 6 kW. The number of obtained events is $\sim 1\times 10^8$.

We check the momentum of the collected charged particles by the data acquisition system with a simulation since we can not reconstruct the momentum of charged particles in the test of the CV.

[9] The y' wires of the DC2 are not active since the readout electronics are not functioning.
[10] The bar has a 2 mm × 4 mm × 1120 mm hole to insert two WLS fibers (Y11, 1 mm diameter).
[11] The detail of the data acquisition system is described in the reference [29]

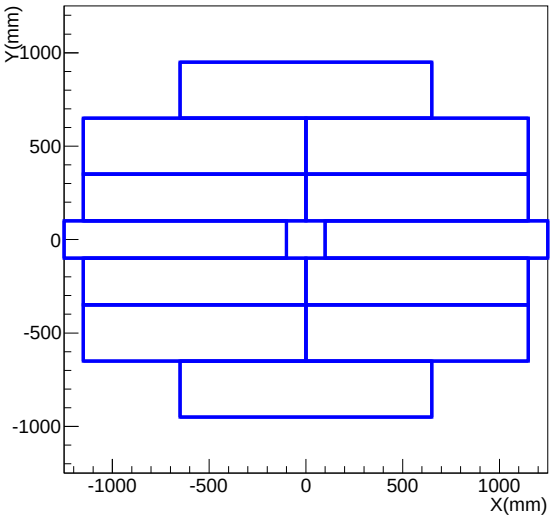

Figure 2.3.3: Rear view of the hodoscope.

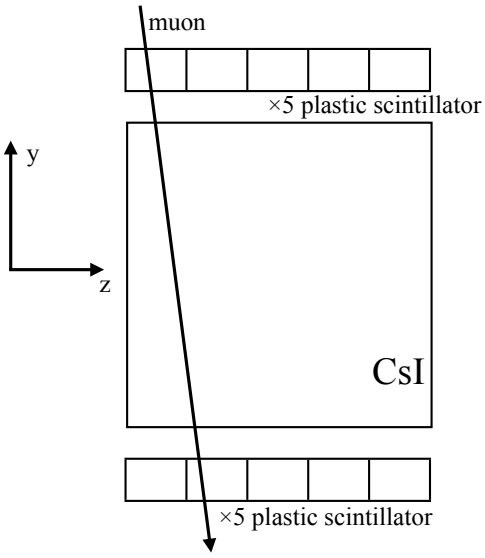

Figure 2.3.4: Plastic scintillators used in the energy calibration of the calorimeter.

The distributions of the true momenta of the charged particles at the CV in the simulation are shown in Fig. 2.3.6. The momentum distribution of pions (black), muons (red), and electrons (green) are overlaid. From Fig. 2.3.6, the charged pions are dominant in the charged particles hitting the CV since the three major decay processes have charged pion. The mean momentum is around 1 GeV/c, and the energy deposit in the CV is almost equivalent to Minimum Ionizing Particle (MIP) for the momentum range in

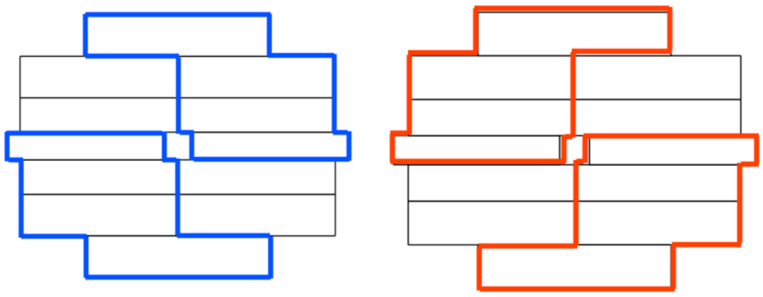

Figure 2.3.5: The configuration of the hit module of the hodoscope in the trigger decision. Blue and red boxes show the hit module.

Fig. 2.3.6. It is unnecessary to reconstruct the momentum of charged particles for the test of the CV.

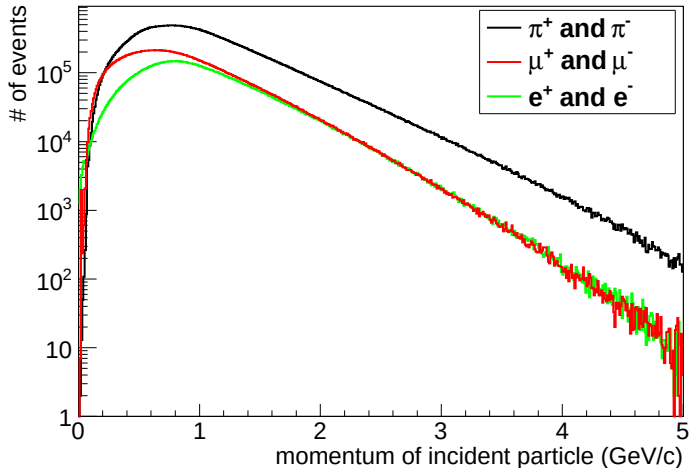

Figure 2.3.6: The distributions of the true momentum of the charged particles at the CV in the simulation.

Chapter 3

Requirements for the charged veto

To achieve the sensitivity of $K_L \to \pi^0\nu\bar{\nu}$ predicted in the Standard Model of particle physics (SM), the K_L decays including charged particles shown in Table 2.1.2 should be rejected. When two charged particles from these decays enter the calorimeter and both of them are missed by the charged veto (CV) placed in front of the calorimeter, these events become background. Since the branching ratio of these decay modes is approximately 3×10^{10} times larger than the signal, high detection efficiency for charged particles is required. In the pilot experiment of KOTO, the E391a experiment, the same concept of the $K_L \to \pi^0\nu\bar{\nu}$ search is adopted and a charged veto detector in front of its calorimeter is also used. In E391a, background events are generated at the CV due to interactions with neutrons in the beam halo, and limit the sensitivity of the $K_L \to \pi^0\nu\bar{\nu}$ search. In this chapter, the CV in E391a and the problem are first reviewed, and then the design of the CV in KOTO is described with requirements.

3.1 CV in the E391a experiment

3.1.1 Design of the E391a CV

A schematic of the CV in E391a is shown in Fig. 3.1.1. The calorimeter with CsI crystal array located down stream of the CV is also shown. The CV consists of inner and outer modules made of 6-mm-thick plastic scintillator. Figure 3.1.2 shows a schematic of the outer and inner modules. Thirty two modules are placed in front of the calorimeter, and four inner modules surround a square beam hole.

3.1.2 Backgrounds related to the CV

The CV modules generate background events due to interactions with neutrons. There are three kinds of backgrounds to be rejected by the CV in the two decay modes: $K_L \to \pi^\pm e^\mp \nu$ and $K_L \to \pi^+\pi^-\pi^0$.

We introduce mechanisms of four backgrounds in the following paragraphs.

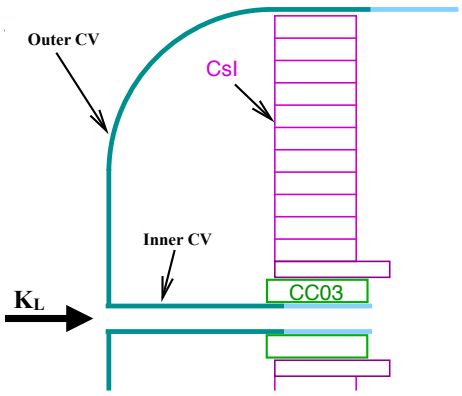

Figure 3.1.1: A cross sectional view of the E391a CV in YZ plane. Definition of other detectors are the same as shown in Fig. 2.1.1 and Table. 2.1.1.

Background from neutrons in beam halo A background process, producing a η or π^0 by the interaction between the neutrons and the CV, is shown in Fig. 3.1.3. These backgrounds are caused by neutrons in the beam halo. In this figure, continuous lines show true trajectories of photons from a η or π^0, and dashed lines show trajectories of two photons from the reconstructed π^0 as described in Sec. 2.1.2. In the left figure, the reconstructed vertex position is shifted to upstream defined as the signal region since the mass of π^0 is assumed in the reconstruction of π^0 for η which has four times larger mass. This background is called CV-η BG. In the right figure, the vertex position is also shifted to the signal region by a cluster of an additional particle from the π^0 production overlapping with the one of two photon clusters in the calorimeter. This background is called CV-π^0 BG.

Background from the $K_L \to \pi^\pm e^\mp \nu$ decay Neither of two charged particles are detected by the CV, the decay process is mis-identified as the signal as shown in Fig. 3.1.4. In this thesis, this background is labeled as "penetrating BG".

In addition to the $K_L \to \pi^\pm e^\mp \nu$ decay, the $K_L \to \pi^\pm \mu^\mp \nu$ decay is another source of the penetrating BG. Since muon does not generate electromagnetic shower, the $K_L \to \pi^\pm \mu^\mp \nu$ decay is easily rejected by the hit patterns of crystals on the calorimeter[1)]. The $K_L \to \pi^\pm \mu^\mp \nu$ decay is not considered in this thesis.

[1)] In KOTO, the number of events which satisfy all cuts in a simulation for the $K_L \to \pi^\pm \mu^\mp \nu$ decay is ~70 times smaller than that of the $K_L \to \pi^\pm e^\mp \nu$ decay.

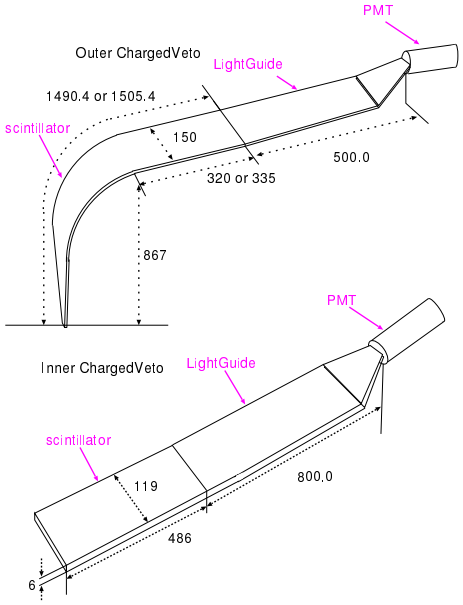

Figure 3.1.2: Schematic of each module of the E391a CV. The top figure shows the outer module. The bottom figure shows the inner module.

Background from the $K_L \to \pi^- e^+ \nu$ decay $K_L \to \pi^- e^+ \nu$ is not only the source of the penetrating BG, but also causes another type of the background as shown in Fig. 3.1.5. Two photons are generated from a π^0 in a charge exchange interaction ($\pi^- + p \to \pi^0 + n$), and other two photons are generated from an annihilation ($e^+ + e^- \to 2\gamma$). This decay is mis-identified as the signal when each pair of two photons makes single hit in the calorimeter, while this decay is rejected when the distance of the two photons on the calorimeter is enough large to be identified as separate objects on the calorimeter. The distance between the two photons becomes larger by extending the distance between the CV and the calorimeter. To reduce this background, the E391a CV is placed at 50 cm upstream from the calorimeter surface. In

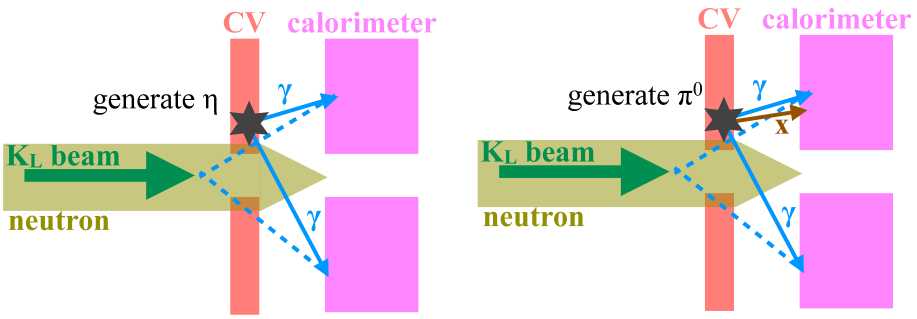

Figure 3.1.3: Mechanism of the backgrounds by a η (right) or π^0 (left) produced from the interaction between the neutrons and the CV.

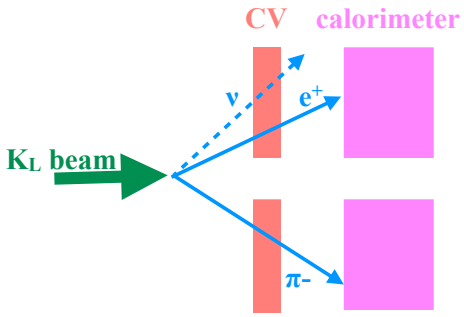

Figure 3.1.4: Mechanism of a background caused by the $K_L \to \pi^{\pm} e^{\mp} \nu$ decay (penetrating BG).

this thesis, this background is labeled as "Ke3 BG".

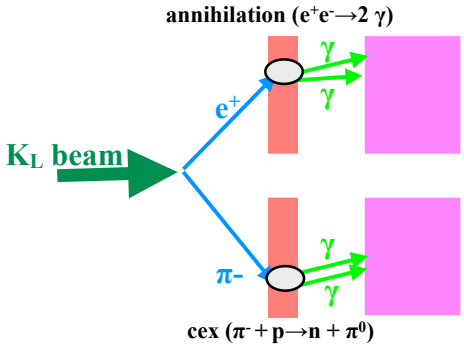

Figure 3.1.5: An example of the background caused by the $K_L \to \pi^- e^+ \nu$ decay (Ke3 BG). Red boxes are the CV, and purple boxes are the calorimeter.

Background from the $K_L \to \pi^+\pi^-\pi^0$ decay Figure 3.1.6 shows an example how the decay mode is mis-identified as the signal. In this figure, two photons from a π^0, charge exchange interactions of π^+ ($\pi^- + p \to \pi^0 + n$) and π^- ($\pi^+ + n \to \pi^0 + p$) without large energy deposit in the CV, are shown. In this thesis, this background is labeled as "Kπ3 BG".

3.1.3 Single event sensitivity and number of backgrounds in E391a

The single event sensitivity in E391a is 1×10^{-8} [4], and the number of the expected signal is 3×10^{-3} assuming the branching ratio of $K_L \to \pi^0 \nu\bar{\nu}$ predicted in the SM. The number of the neutron backgrounds is expected to be ~ 0.5 and that of the K_L decay backgrounds is expected to be $O(10^{-4})$ [4]. The number of neutron backgrounds is 100 times larger than the signals, and the neutron backgrounds limit the sensitivity of E391a.

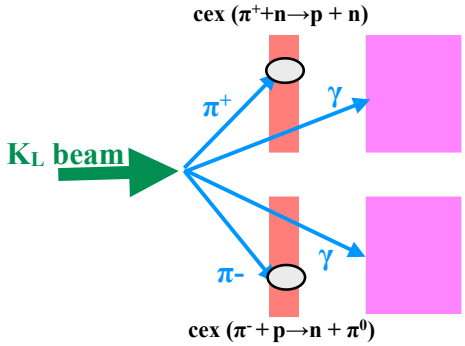

Figure 3.1.6: An example of the background caused by the $K_L \to \pi^+\pi^-\pi^0$ decay (Kπ3 BG). Red boxes are the CV, and purple boxes are the calorimeter.

3.2 CV in the KOTO experiment

As shown in the previous section, the E391a CV suppresses the K_L decay backgrounds to the sufficiently low level, while the number of neutron backgrounds is large. The neutron background should be reduced by more than a factor of 10^3 to be less than 10 % of the expected signals and to achieve the sensitvity of $K_L \to \pi^0\nu\bar{\nu}$ predicted in the SM. The CV in KOTO is designed to suppress the neutron interactions, as well as to keep the sufficient rejection power to the K_L decay backgrounds. Two separated layers are adopted and the readout scheme of the scintillator is changed.

The CV in KOTO is shown in Fig. 3.2.1. The CV consists of two layers of 3-mm-thick plastic scintillators. The first layer of the CV is labeled as "front CV", and the second as "rear CV". Since the CV is exposed in a high rate environment, each plane of the CV consists of ~50 strips to reduce occupancy per one readout channel.

A schematic of the scintillator strip is shown in Fig. 3.2.2. Seven wavelength shifting (WLS) fibers are embedded in the scintillator, and both ends of them are bundled and readout by photosensors. The region under the groove for the WLS fibers is thinner than the other part. Details of components are described in Chapter 4. To achieve sufficient background rejection, we devise five features as the upgrade from the E391a CV: eliminating the inner CV, adding a front CV layer, reducing the mass, embedding the fibers for light collection, and adopting both-end readout of fibers.

The inner CV is eliminated to reduce the neutron backgrounds. In E391a, the inner CV interacts with high momentum neutrons around the beam and generates the CV$-\eta$ BG since the inner CV is placed in parallel to the beam and the neutron path length is long. Instead of the inner CV, the rear CV is placed in front of the calorimeter to detect the charged particles escaping the front CV.

The two-layer configuration of the CV, front and rear, improves the rejection power to the Ke3 BG

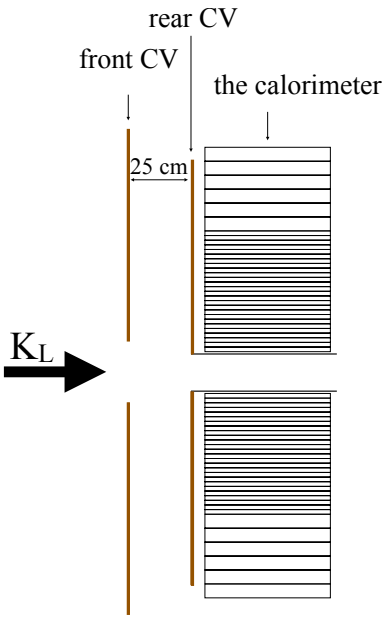

Figure 3.2.1: The cross sectional view of the KOTO CV in YZ plane.

shown in Fig. 3.1.5. The number of the Ke3 BG becomes large when only rear CV is located in front of the calorimeter since the distance between the rear CV and the calorimeter is too short to identify two separate photons in the calorimeter. The front CV is placed to keep the distance between the CV and the calorimeter large enough. When the distance between the front CV and the calorimeter is too large, the number of the Ke3 BG becomes large since the fraction of the $K_L \to \pi^- e^+ \nu$ decays hitting the rear CV increases. The number of the neutron backgrounds also becomes large by the neutrons interacting with the front CV since the production point of π^0 or η from the neutron interaction is shifted to upstream. Therefore, the distance between the front CV and the calorimeter should be minimized. We first developed inefficiency functions for charged particles [24] to evaluate the number of Ke3 BG since it was not practical to simulate this background with enough statistics. In this study, the detection threshold of the CV was assumed as 100 keV[2)]. With this threshold, the CV was able to detect π^- and e^+ penetrating scintillator more than 0.5 mm before a charge exchange interaction or an annihilation occurs. We then optimized the position of the front CV by using this function, and decided the position of the front CV at 25 cm upstream from the rear CV [31]. In this design, the number of the Ke3 BG was estimated to be 0.07 ± 0.04 [25], and the number of the Kπ3 BG was estimated to be 0.11 ± 0.01 [25].

We decide to use 3-mm thick plastic scintillator to minimize the neutron backgrounds. It is determined due to a structural limit for a construction of the CV. The number of the CV-η BG is estimated to be 0.01 ± 0.01 [25], and the number of the CV-π^0 BG is estimated to be 0.04 ± 0.04 [25], which are

[2)] In E391a, the detection threshold was set to 300 keV.

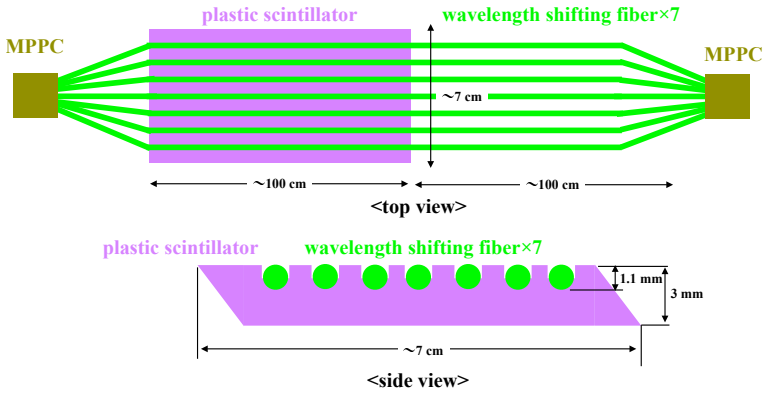

Figure 3.2.2: Schematic of each strip in the KOTO CV. Top figure shows the module viewed from downstream of the CV. Bottom figure shows a cross sectional view of each module.

5000 times smaller than that expected in E391a.

The readout by embedding WLS fibers is introduced to solve the following problem. Since we reduce the thickness of the scintillator from 6 mm to 3mm, the number of reflections increases in the scintillator and causes light attenuation. As a result, it is difficult to achieve high efficiency with a direct readout of the scintillator. We then use the fibers which absorb blue lights from the scintillator and emit green lights, and whose attenuation length is larger than the scintillator.

Both ends of fibers are readout by photosensors and summed in the offline analysis to achieve the high light yield. Good timing resolution also can be achieved by the both-end readout, and the mean of hit timing at both ends is used in the KOTO experiment. The achievement of the good timing resolution is essential since a hit timing of the CV is used for the veto and the CV is exposed in a high rate environment as described in Sec. 3.3.2.

3.3 Requirements for the CV

The CV is required to have the high detection efficiencies for charged particles and the good timing resolution. As described in Sec. 3.2, each plane of the CV consists of ~50 strip. If there are gaps between the strips, a chareged particle entering the gap penetrates the CV without any interaction. The inefficiency of the CV by the gaps is defined as loss of geometrical acceptance, and it should be minimized to reject the penetrating BG. The energy threshold of 100 keV is required to suppress the Ke3 and the Kπ3 BG at the required level as discussed in the previous section. The good timing resolution is a key to minimize the signal loss due to accidental veto. The requirements to the CV are summarized in 3.3.1. Loss of geometrical acceptance and light yield are the requirement in inefficiency and described

in Sec 3.3.1. The requirement in timing resolution is described in Sec. 3.3.2. The requirements are studied with Monte Carlo (MC) simulations, and details are described in App. B.

Table 3.3.1: Summary of three requirements of the KOTO CV.

feature	requirement
loss of geometrical acceptance	$< 10^{-3}$
light yield	> 10 p.e./100keV
timing resolution	< 3 ns

3.3.1 Inefficiency for charged particles from the K_L

Requirement on the loss of geometrical acceptance

We first estimate the number of the penetrating BG without the CV, and then evaluate the requirement of the loss of geometrical acceptance.

The distribution of remaining events after applying the hit pattern cut in the calorimeter described in App. A is shown in Fig. 3.3.1[3)]. The horizontal axis shows the reconstructed vertex of the π^0, and the vertical axis shows the reconstructed transverse momentum of the π^0, which are described in Sec. 2.1.2. The black box shows the allowed region of the signal. The number of remaining events in the signal box is $\sim 10^9$ with $\sim 5 \times 10^{12}$ K_L decays that we expect to collect in the KOTO experiment. The CV is required to reduce the backgrounds by more than a factor of 10^{10} [4)].

The $K_L \to \pi^\pm e^\mp \nu$ decay mainly makes four hits, two on each layer of the CV, and the total reduction is expected to be the fourth power of the single-layer inefficiency. We set the requirement of the inefficiency for the single layer as 10^{-3} and the total inefficiency is expected to be 10^{-12}. The number of background events is estimated to be 0.001. The loss of geometrical acceptance should be smaller than 10^{-3} when no other source of inefficiency exists.

Requirement for the light yield

The inefficiency of the CV is affected by the number of photoelectrons per unit energy deposit (light yield) since the width of the energy spectrum in the CV is determined by the energy resolution stemming from photon-statistics of the light yield. To set the requirement on the light yield, the energy deposit of charged particles for the penetrating BG, the Ke3 BG and the Kπ3 BG are estimated without

[3)] Each point is weighted by the factor 10^{-12}.

[4)] The number of expected signals is 2.4 (Sec. 2.1.3), and the number of the penetrating BG should be less than 10 % of the expected signals to achieve the sensitvity of $K_L \to \pi^0 \nu\bar{\nu}$ predicted in the SM.

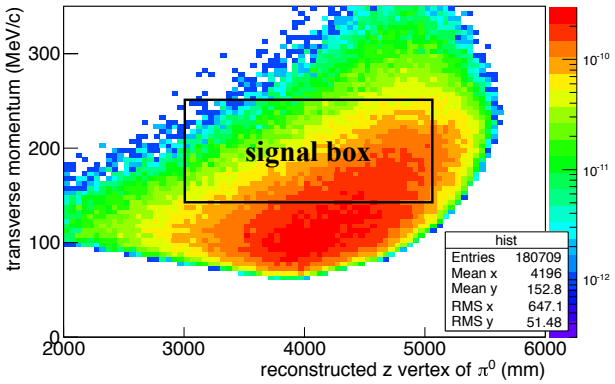

Figure 3.3.1: Distribution of remaining events after applying the hit pattern cut on the calorimeter for the $K_L \to \pi^{\pm} e^{\mp} \nu$ decay.

any smearing from photon statistics. The energy spectrum is then smeared according to the photon-statistics of the light yield. We set the requirement of the light yield so that variation of the inefficiency from the inefficiency without smearing is less than 10%.

The distributions of energy deposit by the π^- of the background candidate without any smearing from photon statistics are shown in Fig. 3.3.2. That of the penetrating BG candidate (black), the Ke3 BG candidate (green), and the Kπ3 BG candidate(red) are shown. In the figure, two minimum-ionizing peaks corresponding to the two different thicknesses of the scintillator, which is explained in Sec 3.2, are seen. In the case of the penetrating BG, there are no events whose energy deposit is less than 100 keV, and the inefficiency is less than 10^{-7} with the energy threshold of 100 keV. The difference between the inefficiency of 10^{-7} and the required inefficiency of 10^{-3} is large enough, and it is unnecessary to concern the increase of the inefficiency by photon-statistics of low light yield. In the case of Kπ3 and Ke3 BG, the energy deposit of less than 100 keV is dominated by the process of charge exchange or hadronic interaction in a dead material [5)]. We find that the CV is expected to have $\sim 10^{-4}$ of inefficiency for the π^- from the Kπ3 or Ke3 BG. The inefficiency of $\sim 10^{-4}$ is equivaret to the required inefficiency, and the increase of the inefficiency for the π^- by the energy resolution should be minimized. The Kπ3 BG determines the requirement of the light yield since the increase of the inefficiency for the π^- from the Kπ3 BG by photon-statistics of low light yield is larger than the Ke3 BG.

The energy deposit of the π^- from the Kπ3 BG candidate is smeared according to the photon-statistics of the light yield as shown in Fig. 3.3.3. The raw energy spectrum (black line), the spectrum smeared with the energy resolution by the photon yield of 2 p.e./100 keV (green line), and the spectrum

[5)]In this study, there is a 0.2-mm-thick film made of polyethylene in front of the CV as a dead material. In KOTO, this film should be installed in front of the CV to keep the upstream of the CV high vacuum, although it is a dead material. We should minimize the material in front of the CV, and we only add a low material reflector film for the scintillator in front of the CV as described in Sec. 4.1. The mass of this material is negligible to that of the polyethylene film.

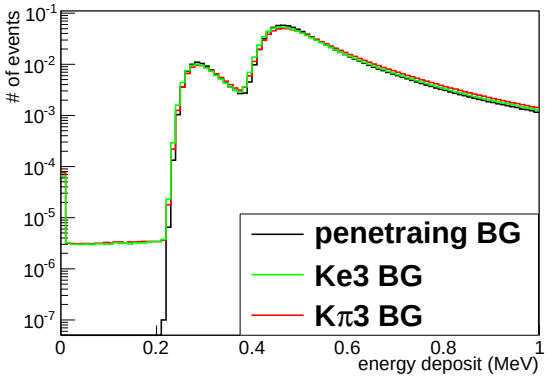

Figure 3.3.2: The distribution of the energy deposit by π^- of each background candidate.

smeared with 10 p.e./100 keV (red line) are shown. The width of the energy spectrum becomes large by the decrease of the light yield. From these plots, we calculate the inefficiency of the CV as a function of the light yield in Fig. 3.3.4. Red line shows the inefficiency without smearing. Shade box shows a region within 10% from the inefficiency without smearing. We find the requirement of the light yield to be more than 10 p.e./100 keV.

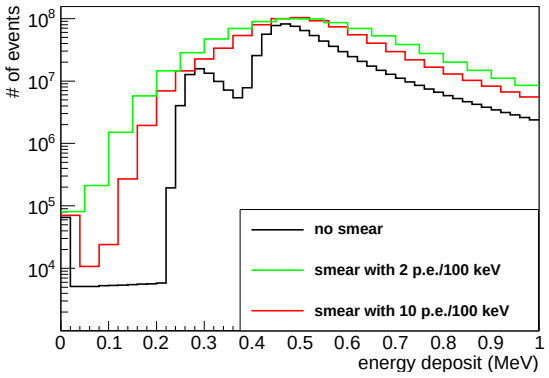

Figure 3.3.3: The energy deposit of the π^- smeared according to the photon-statistics of the light yield. The binning of black line is 20 keV, that of green line is 50 keV, and that of red line is 40 keV.

3.3.2 Requirements for the timing resolution

As described in Sec. 2.1.1, the π^0 signal is selected in the calorimeter when the CV has no energy deposit within the veto window. When the events with the accidental activity in the CV are vetoed, which causes loss of the signal (accidental loss). Ratio of the accidental loss is calculated as the following

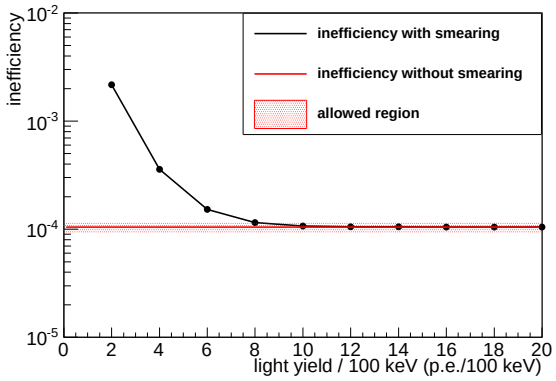

Figure 3.3.4: The inefficiency of the CV as a function of the light yield.

equation by using the width of the veto window (T_{veto}) and the accidental hit rate (R_{acc}):

$$\text{Ratio of accidental loss} = 1 - e^{-T_{veto}R_{acc}}. \tag{3.1}$$

Table 3.3.2 shows the accidental hit rate of the CV with 100 keV threshold at the designed beam power of KOTO. We find that the charged particles from the K_L are the main source of the accidental hits. Figure 3.3.5 shows the accidental loss as a function of the width of the veto window. To keep the accidental loss at the level of 5%, the veto window should be narrower than 30 ns and it requires good timing resolution to the CV. We first study distributions of the hit time difference between the calorimeter and the CV to evaluate the width of the veto window. Second, we estimate the accidental loss taking into account the timing resolution. Finally, we check the accidental loss.

Table 3.3.2: Accidental hit rate of the CV with 100 keV threshold at the designed beam power of KOTO.

source	rate (MHz)
K_L	1.8
γ	0.1
neutron	0.08
other	0.1
All	2.1

We estimate the hit time difference between the calorimeter and the CV for the main K_L decay modes: $K_L \to \pi^{\pm}e^{\mp}\nu$, $K_L \to \pi^{\pm}\mu^{\mp}\nu$, and $K_L \to \pi^{+}\pi^{-}\pi^{0}$. Figure 3.3.6 shows the distribution of the time difference. We do not apply hit pattern cuts in the calorimeter to keep enough statistics. The hit time difference of the $K_L \to \pi^{\pm}e^{\mp}\nu$ decay (black), the $K_L \to \pi^{\pm}\mu^{\mp}\nu$ decay (red), and the $K_L \to \pi^{+}\pi^{-}\pi^{0}$ decay (green) are shown[6)]. In the $K_L \to \pi^{\pm}e^{\mp}\nu$ decay or the $K_L \to \pi^{\pm}\mu^{\mp}\nu$ decay, the distribution is narrow

[6)] When single charged pion hits both the CV and the calorimeter and makes two clusters by hadronic interactions, the hit

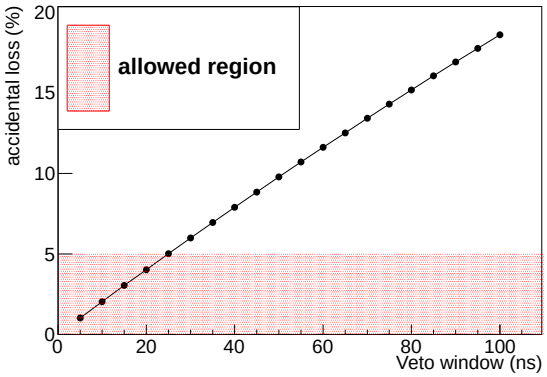

Figure 3.3.5: The accidental loss as a function of the width of the veto window.

since the charged pion and the lepton hit both the calorimeter and the CV. On the other hand, the time difference in the $K_L \to \pi^+\pi^-\pi^0$ decay becomes larger when the charged pion hits only the CV and the two photons from the π^0 hit the calorimeter. This is the reason that the distribution of $K_L \to \pi^+\pi^-\pi^0$ is larger than other decay mode. Each distribution is enough narrower than 30 ns, and the width of the veto window is determined by the effect of timing resolution as described in the next paragraph. As mentioned in the previous section, the CV has 10^{-4} of inefficiency for the π^- from the Kπ3 BG, and the veto window is set to have no effect for this inefficiency.

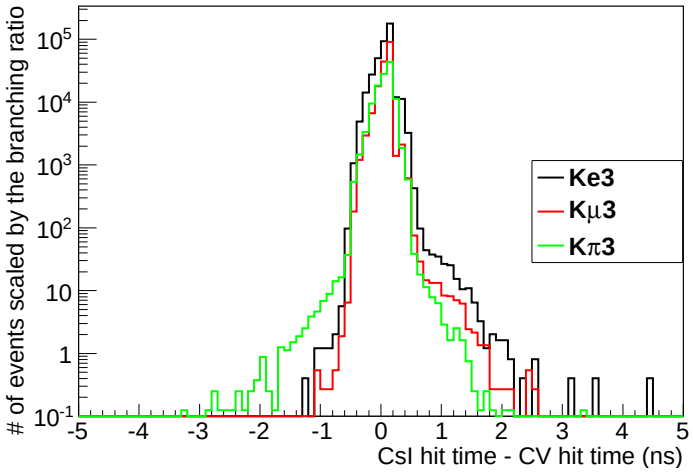

Figure 3.3.6: The distribution of the time difference between the calorimeter and the CV.

time of the calorimeter becomes later than the nominal hit time. These events dominate each distribution in the more than 1 ns region.

In the $K_L \to \pi^+\pi^-\pi^0$ decay, the hit time of the CV and the calorimeter are smeared with a timing resolution according to a Gaussian distribution. Figure 3.3.7 shows the distribution of the time difference with the smearing. The hit time of the calorimeter is smeared with 1 ns. The hit time of the CV is smeared with 0 ns (black line), 1 ns (red) and 3 ns (green). From these plots, we calculate the width of the veto winodw. Figure 3.3.8 shows the veto window and the accidental loss. The horizontal axis shows the timing resolution, and the vertical axis in the left shows the width of the veto window. The vertical axis in the right shows the accidental loss. To keep the accidental loss at the level of 5%, the timing resolution of the CV should be better than 3 ns.

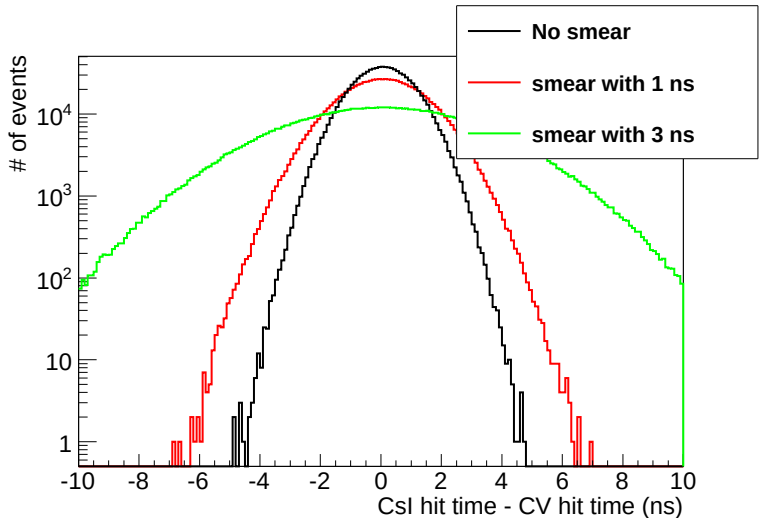

Figure 3.3.7: The effect of the timing resolution to the hit time distribution.

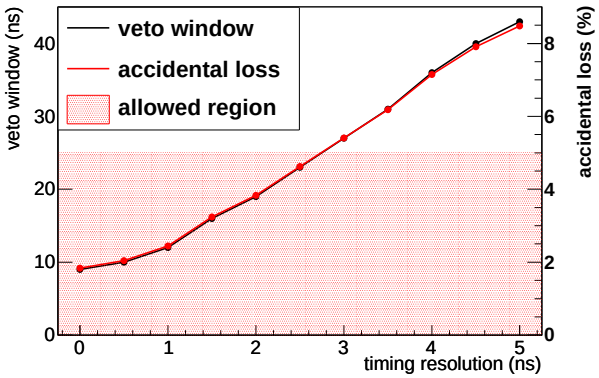

Figure 3.3.8: The accidental loss and the required veto window as a function of the timing resolution.

Chapter 4

Design and production of the CV

We describe the design of the CV. We explain the developments of components of the CV. Finally, we report the production and the construction of the CV.

4.1 Design of the CV

The arrangement of the CV scintillator strips with the assignment of module ID is shown in Fig. 4.1.1. The left figure shows the front layer of the CV, and the right figure shows the rear layer of the CV. Both layers of the CV have a quadrant structure with a 90-degree symmetrical arrangement, with a beam hole in the center. One quadrant consists of twelve (eleven) scintillator strips in the front (rear) layer. The shape of the plane is designed to cover the whole region of the calorimeter[1)]. The number of strips per layer is designed to reduce the count per readout channel. Figure 4.1.2 shows the accidental hit rate of the CV with the designed beam intensity of KOTO in the simulation as described in App. B.4. The horizontal axis shows the module ID, and the vertical axis shows the accidental rate in one strip with the energy threshold of 100 keV. The maximum count rate is $\sim$ 200 kHz, and it is acceptable from the point of rate tolerance of a readout circuit. The front CV is orthogonally arranged against the rear CV. We minimize an overlap region between the boundary of the strips on the front CV and that on the rear CV to prevent the loss of geometrical acceptance as described in Sec. 3.3.1. Table 4.1.1 shows summary of the CV structure.

A schematic view of one quadrant in the front CV is shown in Fig. 4.1.3. The strips are tied onto a 0.8 mm thick carbon-fiber-reinforced-plastic (CFRP) plate with fluorocarbon wires. There are 0.6 mm $\times$ 0.4 mm holes in boundaries of the strips to path through the wires[2)]. The holes make an insensitive

[1)]The region within the radius of 850 mm, and outside of 150 mm $\times$ 150 mm in xy coordinate. The beam hole size of the front CV is decided to avoid the interaction by the neutrons surrounding the K_L beam with the front CV.

[2)]Only in the boundary where the strip contacts its neighbor strip in the longitudinal direction of the strip. There are three

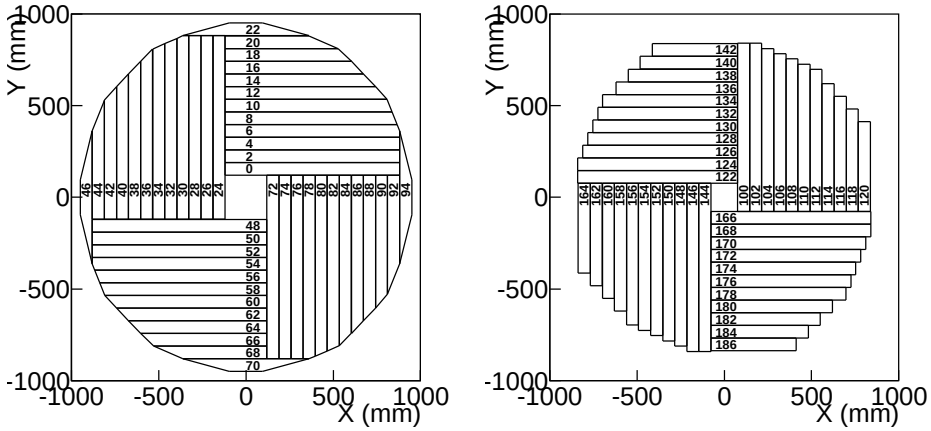

Figure 4.1.1: The arrangement of the strips and the module ID.

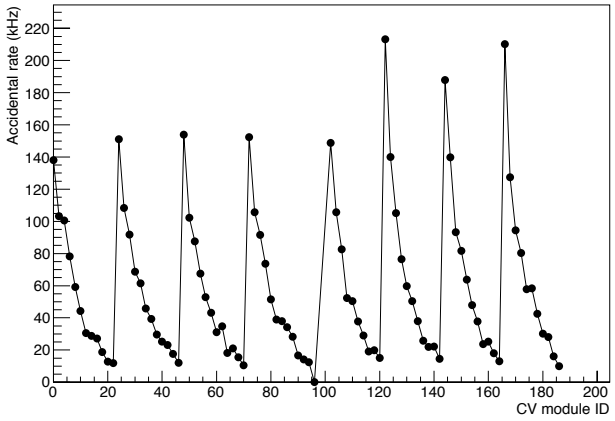

Figure 4.1.2: Accidental hit rate of the CV.

Table 4.1.1: Summary of the CV structure.

	Front layer	Rear layer
Outer radius (mm)	950	850
Beam hole size (mm^2)	242×242	154×154
Number of scintillator strips	48 (12×4)	44 (11×4)
Lengths of the strips (mm)	644–1002	490–917
Number of readout channels	96	88

region, and the ratio of the inefficient area to the whole area is 10^{-5} for all the holes. This is smaller than the required inefficiency of 10^{-3}.

holes in one boundary.

Side view of one strip is shown in Fig. 4.1.3 right. One strips is 70.7 mm wide and 3 mm thick. Seven 1 mm diameter fibers are embedded and glued into grooves on one strip at 10 mm interval. The cross section of a groove [3)] is 1.1 mm $\times$ 1.1 mm. Four sides are cut at an angle of 60°. We make an overlap with neighboring strips without increasing the thickness to prevent the loss of geometrical acceptance caused by a gap.

The side view of one strip is shown in Fig. 4.1.3 bottom. Fibers are not glued in the 20 mm region at the both ends of the strip. Fibers are fed to the opposite side of the CFRP plate through the rectangular holes in this region. Seven fibers are bundled, and both ends of the bundle are readout by Multi Pixel Photon Counters (MPPCs) in the outer region of the CV. We call one end of the strip "long side" and the other "short side" according to the length of fibers hanging out of the strip.

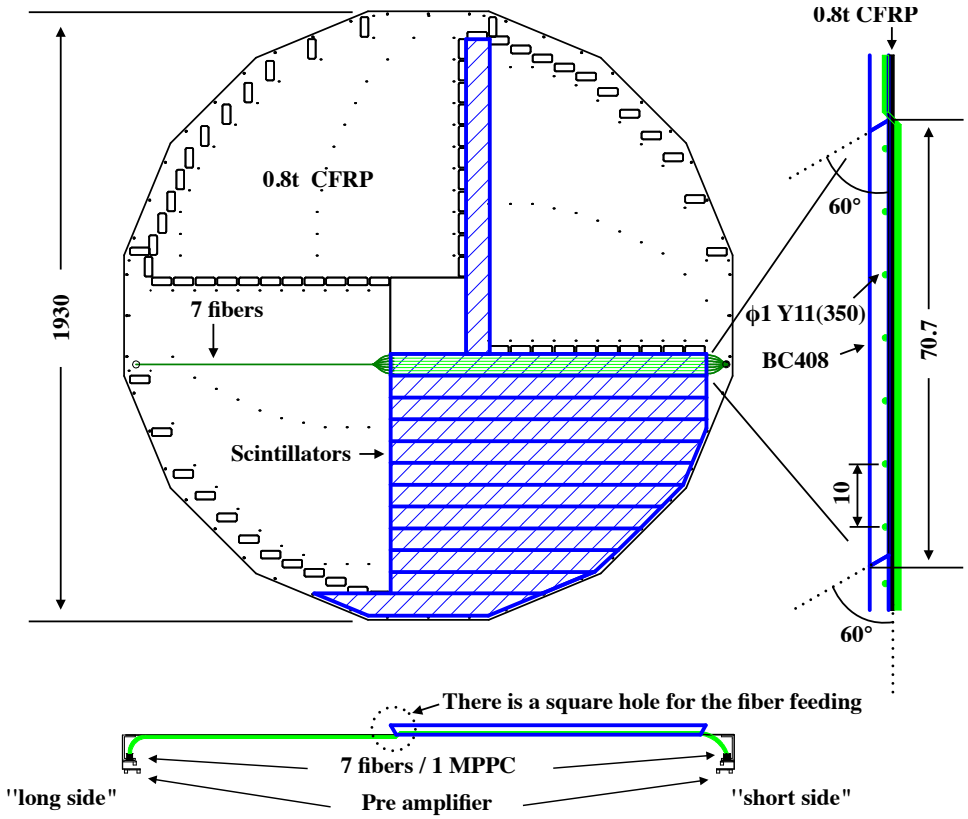

Figure 4.1.3: Schematic view of one quadrant in the front CV. The right figure is viewed from the right of the center figure. The bottom figure is viewed from the bottom of the center figure.

One strip is composed of BC404 plastic scintillator by Saint-Gobain [32], Y11 (350) WLSF by Kuraray [33], and S10943-0928(X) MPPCs by Hamamatsu Photonics [34]. One strip is wrapped with

[3)]The bottom of the groove is a circular shape to make full contact between the surface of the fibers and the scintillator.

a reflector film: an aluminized polyester film (Tetolight) by OIKE & Co., Ltd. [35][4]. Figure. 4.1.4 left shows the emission spectrum of BC404 [32], and Fig. 4.1.4 right shows the absorption and emission spectrum of Y11 [33]. Y11 has an emission peak at ~500 nm, and Y11 is suitable to readout by MPPC. We use MPPC to achieve high light yield since MPPC has an approximately 2.5 times higher detection efficiency for green light (~ 45% at 480 nm[5] [36]) than ordinary photomultipliers. The detail of MPPC is described in Sec. 5.1.

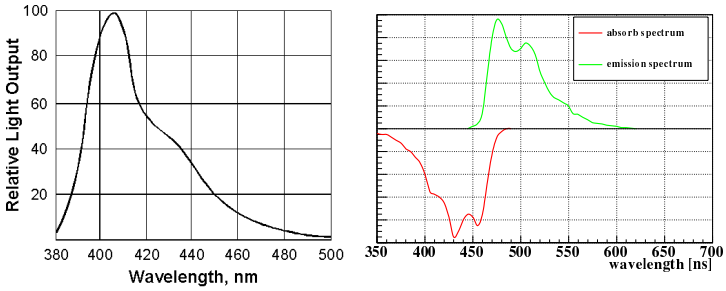

Figure 4.1.4: Spectral response of each component. Left plot shows the emission spectrum of BC404 [32]. Right plot shows the absorption and emission spectrum of Y11 [33].

4.2 Development of the CV components

We develop three components to maximize the light yield: the material of the scintillator, concentration of wavelength shifter in Y11, the connection method between the fibers and the MPPC.

4.2.1 Material of the scintillator

We measure the light yield of three kinds of plastic scintillators with Y11 and MPPC. First, we compare the light yield of EJ212 [37] and that of EJ204 [37] by using a prototype of the CV and a ^{90}Sr β source. The light yield with the sum of both-end readouts is 10.6±0.06 p.e./100 keV for EJ212, and 13.2±0.3 p.e./100 keV for EJ204. Second, we compare the light yield of EJ204 and that of BC404 by using another kind of the prototype CV. The fiber length of this prototype is longer than that used in the comparison of EJ202 and EJ204, and the light yield of EJ204 is decreased by the increase of the light attenuation. The light yield is 10.6±0.04 p.e./100 keV for EJ204 and 12.3±0.4 p.e./100 keV for BC404. Table 4.2.1 shows the summary of the light yield measurement. BC404 has the maximum light yield, and we choose BC404 for the CV.

[4] The thicknesses of the base film and the deposited aluminum are 12 μm and 40–50 nm, respectively.
[5] This value includes after pulse and crosstalk of MPPC.

Table 4.2.1: Summary of the light yield measurement.

material	light yield in the first measurement	light yield in the second measurement
EJ212	10.6±0.06 p.e./100 keV	
EJ204	13.2±0.3 p.e./100 keV	10.6±0.04 p.e./100 keV
BC404		12.3±0.4 p.e./100 keV

4.2.2 Concentration of wavelength shifter

Light absorption of the WLS fiber from a scintillator increases with more concentration of the wavelength shifter. With more concentration, self light absorption in the fiber increases, and the attenuation length of the fiber becomes shorter. To optimize the concentration, we produce two kinds of the Y11 whose concentration are 200 ppm (Y11 (200)) and 350 ppm (Y11 (350)). The fibers are embedded in the prototype CV whose fiber length is the same as that in the CV strip, and the light yields are measured. The light yield is 11.1 ± 0.04 p.e./100 keV for Y11 (200), and 14.6 ± 0.09 p.e./ 100 keV for Y11 (350), and we select Y11 (350).

4.2.3 Connection between the fibers and the MPPC

A schematic view of the connection method between the fibers and the MPPC is shown in Fig. 4.2.1. The left figure shows the top view of the MPPC and fibers, and the right figure shows the side view. Fibers (green), connector (gray), and socket (cobalt blue) are shown. The seven fibers are glued in a hole of the connector. The package of the MPPC is soldered on a PCB board. The socket is fixed on the PCB board. There is air gap between the fibers and the MPPC. We minimize the distance between the surface of the fibers and that of the MPPC (fiber-MPPC distance) to maximize the acceptance of lights from the fibers. We also minimize the misalignment between the center of the fibers and that of the MPPC in the left figure (fiber-MPPC misalignment).

We carry out a simulation to minimize the distance and to estimate the loss of lights. In this simulation, machining error of components are implemented with ±0.2 mm for the MPPC, and ±0.05 mm for other components. The uncertainty of the fiber-MPPC distance is shown in Fig. 4.2.2 left[6)]. The uncertainty of the fiber-MPPC misalignment is shown in Fig. 4.2.2 right. The uncertainties obtained from the convolution of all the machining errors is shown in these plots. We find that the fiber-MPPC distance becomes 0.3-mm shorter at most, and decide the fiber-MPPC distance to be 0.6 mm from Fig. 4.2.2 left since there is the epoxy resin[7)] (0.3 mm in thickness) upon the surface of the MPPC. We also find that the uncertainty of the fiber-MPPC distance is ±0.3 mm and that of the fiber-MPPC misalignment

[6)]The center of the distribution shift to + x region since a part of machining uncertainty for the distance is more than 0 mm.
[7)]It is the protection for the photosensitive surface of the MPPC.

is ±0.4 mm.

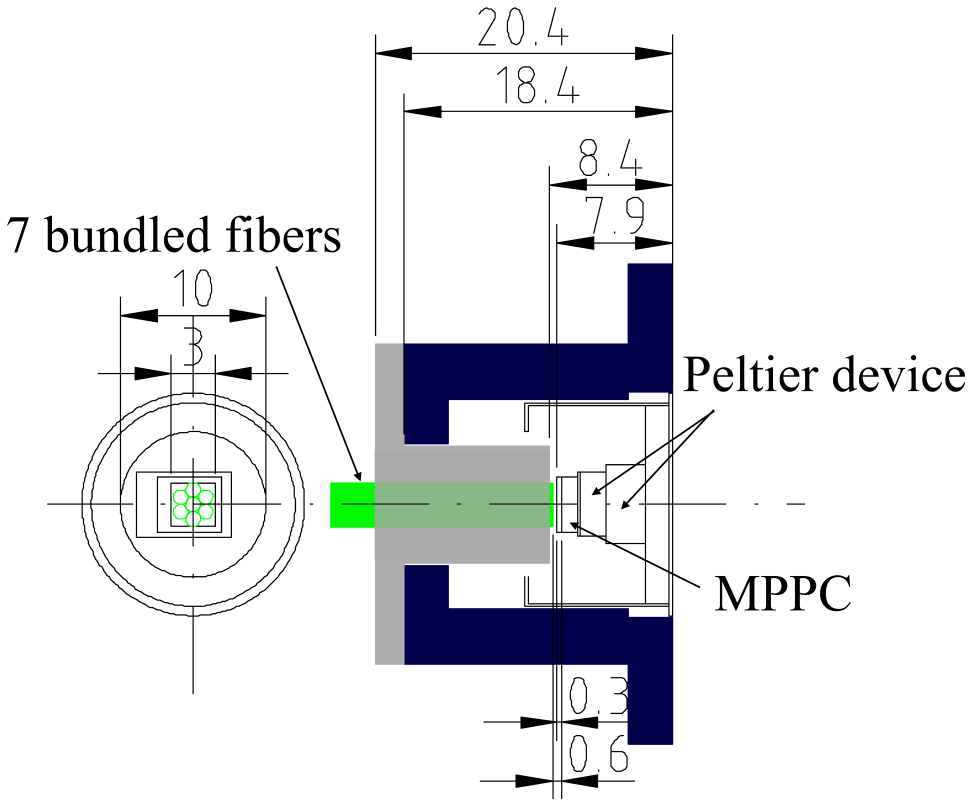

Figure 4.2.1: Schematic view of the connection method between the fibers and the MPPC. Left figure shows the top view of MPPC and fibers. Right figure shows the side view. Fibers (green), connector (gray), and socket (cobalt blue) are shown.

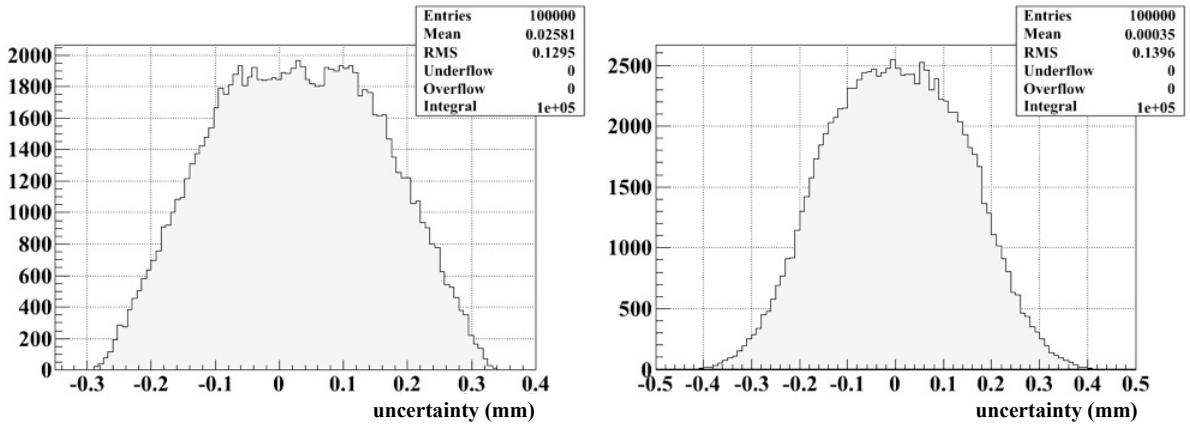

Figure 4.2.2: The uncertainty of the distance between the surface of the fibers and that of the MPPC (left). The uncertainty of the misalignment between the center of the fibers and that of the MPPC (right).

We estimate the fraction of the lights from the fiber not hitting the MPPC by using the estimated uncertainties. The light from the fibers is emitted uniformly in the solid angle defined by the numerical aperture of Y11. The path of light is calculated in consideration of the transmittance of air and the epoxy resin. The light loss is 9.5% in the nominal case and 14.5% in the worst case. We conclude that the loss is acceptable in this design. By this development, the light yield of the CV becomes 20% larger than that of the prototype as shown in Fig. 4.3.2.

4.3 Production and light yield measurement of the scintillator strips

4.3.1 Production of the scintillator strips

The production of the scintillator strip has mainly four steps: cutting a scintillator plate and grooves, embedding fibers, bundling fibers into a connector, and wrapping the strip with a reflector film.

We prepare sixteen scintillator plates whose size is 1010 mm $\times$ 570 mm $\times$ 3 mm. We measure the thickness of these plates by a laser displacement meter[8)]. The mean thickness of the scintillators is 3.10 mm and its RMS is 0.19 mm. The region thicker than 2.75 mm is used for the strips to ensure enough light yield. In each strip, seven grooves for fibers are made with a milling machine.

We embed fibers into the grooves and glue them by using an optical cement (ELJEN EJ-500 [37]). We develop an automatic applicator system for the glueing as shown in Fig. 4.3.1. In the applicator system, scintillators are fixed on the "scintillator fix plate". Fibers are embedded into the grooves of the scintillators, and the both ends of fibers are fixed with the "fiber fixer". The "dispenser" is filled with the optical cement, and the cement is applied onto the fibers automatically. The dispenser is moved by linear stages automatically.

We glue the fibers to the connector as shown in Fig. 4.2.1. The fibers are cut to the designed length[9)]. The fibers are bundled into the connector at their both ends, and glued. The end surface of the fibers are polished by a diamond polisher. We measure the distance between the bottom of the connector and the surface of the fibers. The distance of all the strips is within $+0.00/-0.05$ mm from the nominal distance, that is well satisfied with our requirement.

Finally, we wrap the strips with the reflector film, described in Sec.4.1.

[8)] The measurement accuracy is ± 0.03 mm.

[9)] The fiber length for one strip is determined by considering a route to the corresponding MPPC location as well as the strip length itself.

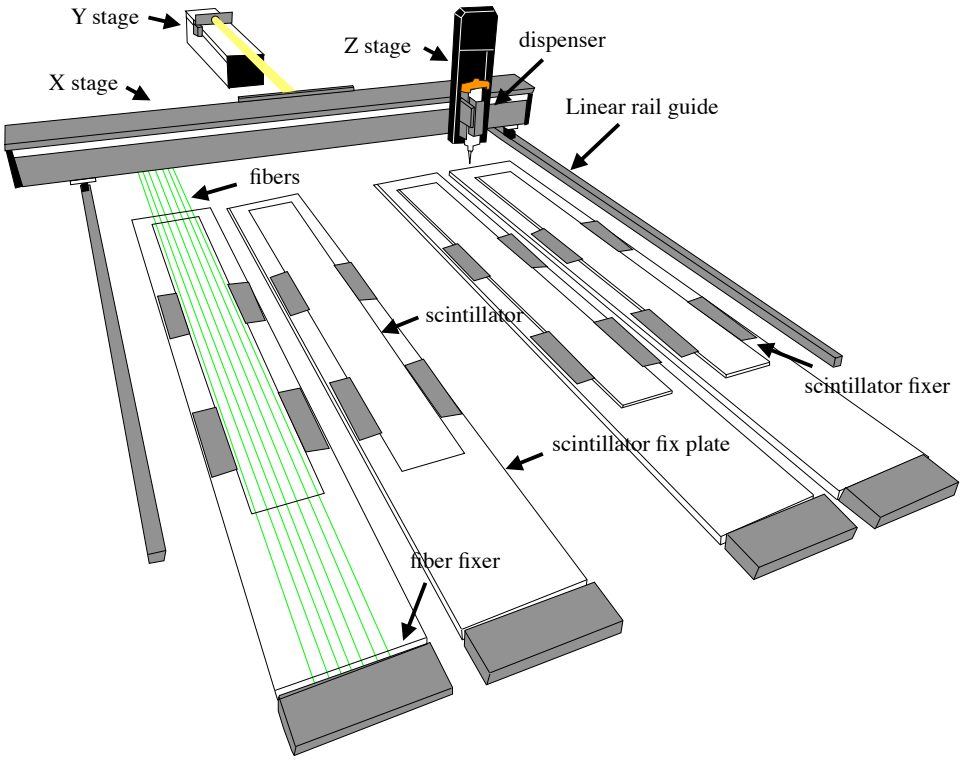

Figure 4.3.1: Schematic picture of the automatic applicator.

4.3.2 Light yield measurement of the strips

We check the light yield of all the strips and the variation of the light yield before installation. We measure the position dependance of the light yield along the fibers by using a ^{90}Sr β source[10]. Figure 4.3.2 shows the light yield of the inner most strip in the front CV as a function of the β source position. The horizontal axis indicates the distance of the source from the "long side" end of the strip. Here the light yield at both ends, and the sum of the two are presented in units of the number of photoelectrons per 100 keV energy deposit [11]. The measured light yield is attenuated along the distance from the MPPC. The light yield is low in the edge regions where the fibers are not embedded in the scintillator. All the points satisfy the light yield requirement of 10 p.e./100 keV. Figure 4.3.3 shows the summed light yields of two sides at the center of the strips including all strips[12]. Red line shows the light-yield requirements of 10 p.e./100 keV. The light yields on average is 16.3 p.e./100 keV. We successfully produce the scintillator strips with 60% higher light yield than the requirement.

[10] The position in the vertical direction of the scintillator strip is fixed at its center.
[11] The energy deposit of the β ray is estimated by a simulation.
[12] They are the points included within the radius of 850 mm in Fig. 4.1.1.

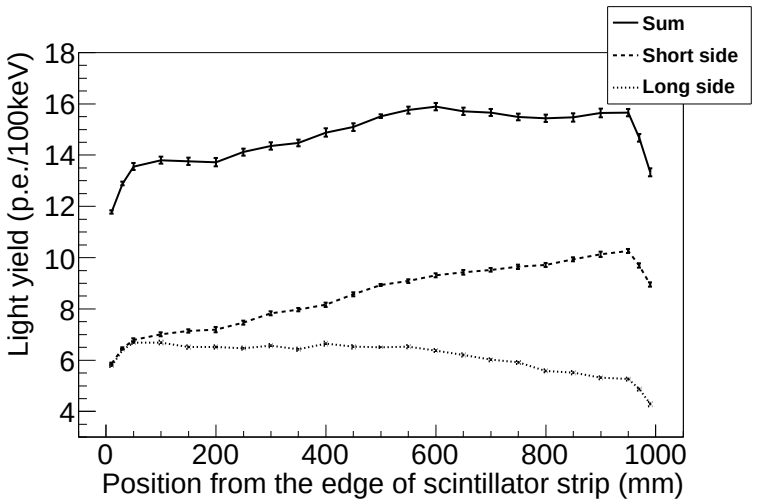

Figure 4.3.2: The light yield of the inner most strip in the front CV as a function of the β source position.

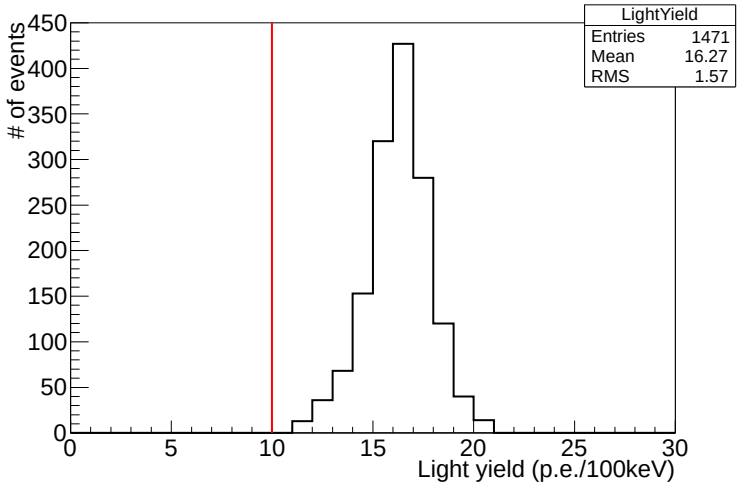

Figure 4.3.3: The summed light yields of all strips.

Finally, we evaluate the validity of the performance of the CV strips to check the quality control of the CV strip in the production. There are 23 kinds of the strip shapes according to their length of the scintillator and fibers. There are four strips with the same shape since the CV has a 90-degree symmetry, and we assign same shape ID to the four strips. Figure 4.3.4 shows variations of the light yields in the four strips. The vertical axis shows a ratio of the RMS of the light yield in one shape ID to its mean[13)]. The horizontal axis shows the shape ID. Black points shows the variation without any correction. Red

[13)]The light yields at the center of strips are used.

points shows the variation with the correction of the thickness variations. The mean of the RMS is 2% after correcting the thickness variations[14]. We succeed in the production of high-light yield scintillator strips with good quality.

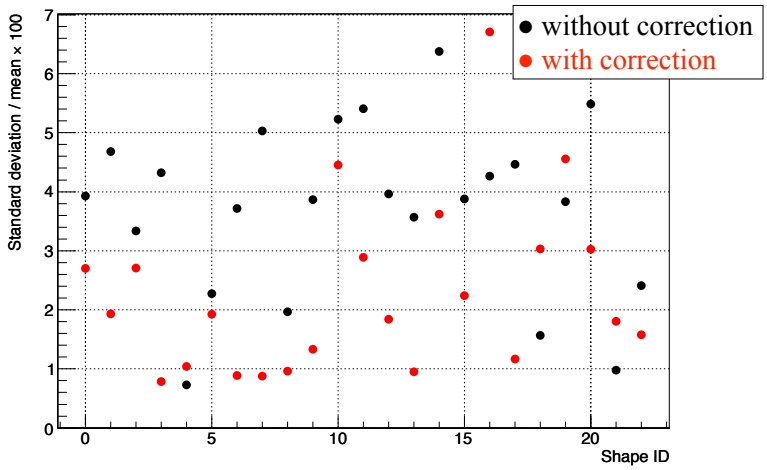

Figure 4.3.4: Variations of the light yields in the four strips to which we assign the same shape ID.

4.4 Construction of the CV

We transport the CV strips to J-PARC after the light yield measurement, and construct the CV. The photo of the rear CV under construction is shown in Fig. 4.4.1. In Fig. 4.4.1, the black plate is the CFRP plate, and the outer ring is the support structure of the CV. We stretch the CFRP plate on the support structure. Four of square poles are attached to the four sides of the support structure to put the CV plane in parallel to the ground. The fibers of the CV strip are fed to the backside of the CFRP plate through the rectangular holes, and the CV strip is fixed on the CFRP plate by using the wires. The fibers are connected to the MPPC at the support structure. The CV strips are fixed in order from the inner strips. After the construction, the CV is fixed in a square frame[15] as shown in Fig.4.4.2. The square frame is installed in the KL beamline, and we carry out the experiment for evaluation of the CV performance.

[14] ID 16 has large variation after the correction since some scintillators are failed to measure the light yield.

[15] The square frame is not used in the nominal KOTO experiment. The CV is fixed to the support structure of the calorimeter in KOTO.

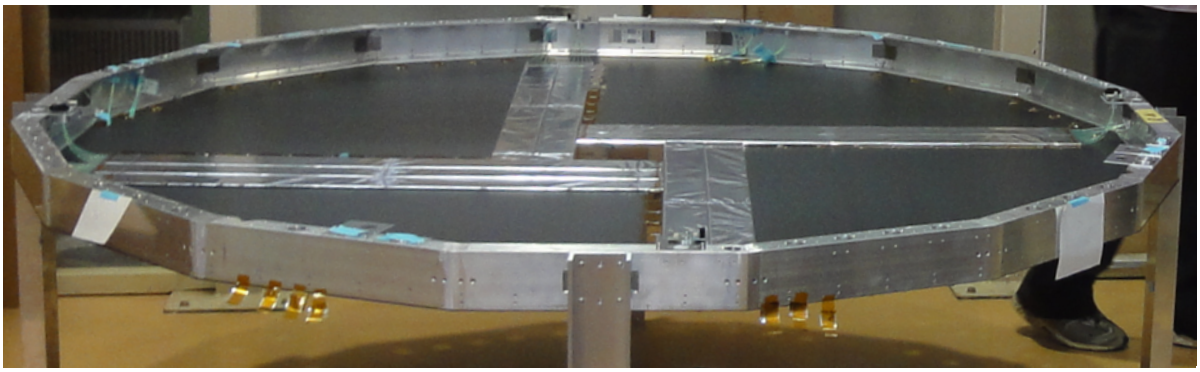

Figure 4.4.1: The photo of the rear CV under construction. The black plate is the CFRP plate, and the outer ring is the support structure of the CV. Four of square poles are attached to the four sides of the support structure. Four of inner most CV strips and four of second inner CV strips are fixed in photo.

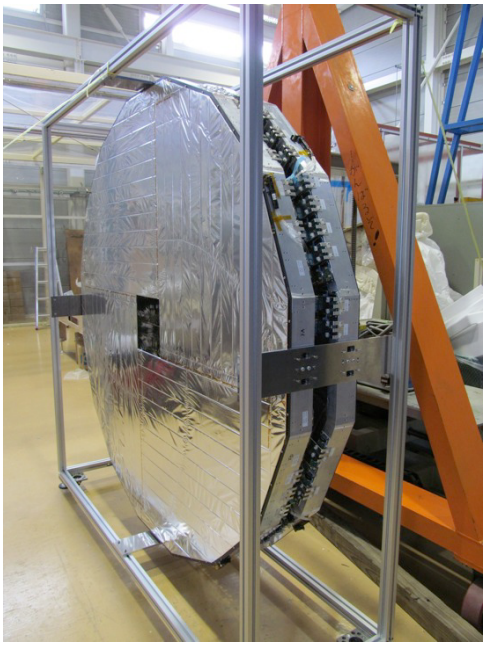

Figure 4.4.2: Photo of the CV and the fixing frame.

Chapter 5

Readout system for the CV

We describe the readout system for the CV. It consists of three components: the MPPC, the preamplifier, and the 125 MHz ADC. We first describe the characteristics of the MPPC. Then, we introduce the readout system for the CV. We describe the control system for the readout system. We evaluate the characteristics of the MPPC and the performance of the preamplifier. Finally, we report the installation and operation of the readout system.

5.1 MPPC

MPPC is a photosensor manufactured by Hamamatsu Photonics. MPPC consists of many avalanche photodiodes (APDs) which are arrayed and electrically connected in parallel. MPPC is operated in Geiger-mode, and the minimum applied voltage of MPPC in Geiger-mode is called "breakdown voltage". In the single APD, a schematic diagram of avalanche multiplication is shown in Fig. 5.1.1 [38]. The avalanche layer, and the depletion layer of N^+ or P^- are shown. Electron-hole pairs are generated[1)] when a photon enters the depletion layer (Internal photoelectric effect). Since the depletion layer is enough long compared to the interaction length of the internal photoelectric effect[2)], MPPC has higher detection efficiency than ordinary photomultipliers. The avalanche multiplication occurs when the electron or hole enters the avalanche layer. For the operation of MPPC in the CV, we concern its four characteristics: the photon detection efficiency, the signal gain, the operation voltage, and noise rate.

- The photon detection efficiency of MPPC increases with the over voltage (V_{OP}) which is the difference between the applied voltage and the breakdown voltage.

[1)] The critical energy is 1-2 eV.

[2)] The thickness of the depletion layer is $\sim$ 10 μm, and the interaction length is 0.5 μm against light whose wavelength is 420 nm.

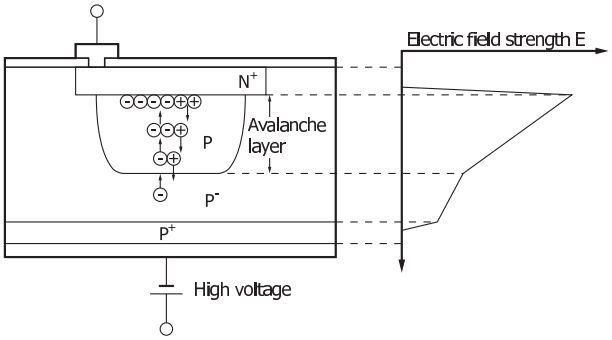

Figure 5.1.1: Schematic diagram of avalanche multiplication in the single APD of MPPC [38].

- The signal gain of MPPC (G_{signal}) is in the following equation by using the number of pixels that detect a photon (N_{pixel}), the electrical capacitance of a single APD (C_{APD}), and the elementary charge (C_e).

$$G_{signal} = (N_{pixel} \times C_{APD} \times V_{OP})/C_e. \tag{5.1}$$

  G_{signal} increases with the over voltage. MPPC is a device to count the number of photons.

- The breakdown voltage of MPPC increases with the temperature.

- A noise signal is caused by thermal generated electron-hole pairs in the depletion layer. We call this noise as dark count noise. Since the probability of the thermal generation increases with the temperature, the rate of the dark count noise increases with the temperature.

From four characteristics, the photon detection efficiency depends on the temperature with $\sim$ 3.5 %/°C [39], and the G_{signal} depends on the temperature with $\sim$ 5 %/°C [40]. The dark count noise affects the energy measurement when the noise overlaps with the signal. To stabilize the photon detection efficiency and G_{signal} and to reduce the dark count noise rate, we use a thermoelectric cooler (Peltier device) thermally connected to MPPC.

We develop a 3 mm square MPPC, which is integrated with a Peltier device, in collaboration with Hamamatsu Photonics. Table 5.1.1 shows specifications of the MPPC used for the CV. Figure. 5.1.2 shows a schematic of the MPPC. The thermistor monitors the temperature of the MPPC on a ceramic board mounted on the Peltier device. All components are put in an aluminum can package.

Table 5.1.1: Specifications of the MPPC

Effective photosensitive area	3×3 mm^2
Pixel pitch	50 μm
Number of pixels	3600
Number of channels	1ch
Package	Metal with TE-cooler
Operation guarantee	$V_{OP} < 2$ V, temperature > 0 °C
Dark count (at 10°C)	200 kHz
Gain ($V_{OP} = 1.5$ V)	8×10^5

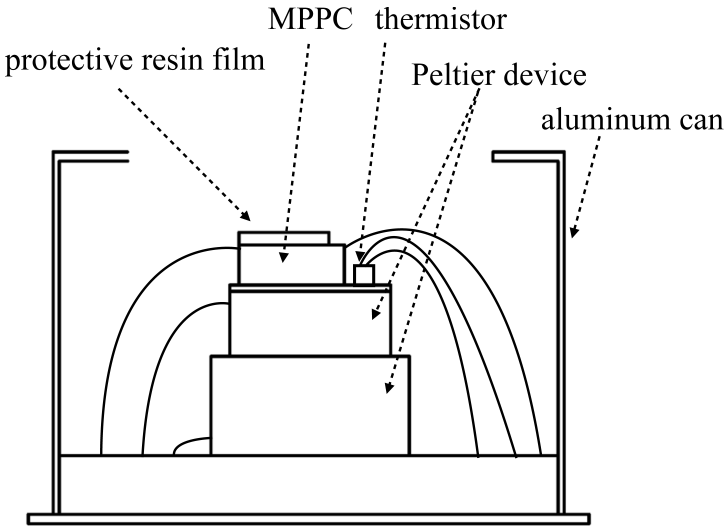

Figure 5.1.2: The schematic of the MPPC.

5.2 Readout system for the MPPC

The readout system for the MPPC consists of three components: the MPPC mounted board, the preamplifier, and the 125 MHz ADC.

The MPPC mounted board is shown in Fig. 5.2.1 [3)]. "DAC" in Fig. 5.2.1 is connected to a digital-to-analog converter in order to adjust the bias voltage of the MPPC, and is connected to the cathode of the MPPC. "Peltier in" is connected to a voltage control circuit as described in Sec. 5.3. "Peltier out" is connected to the current return for the Peltier device. "Base bias" is connected to a common voltage supply for the MPPCs, and connected to the anode of the MPPC. "Signal out" is sent to a 50-fold preamplifier. "Thermistor in" is connected to a voltage supply for the thermistor. "Thermistor out" is connected to the voltage control circuit for the Peltier device.

[3)]The temperature sensor (Tmp37) is mounted on the PCB board to monitor surface temperature of the PCB board.

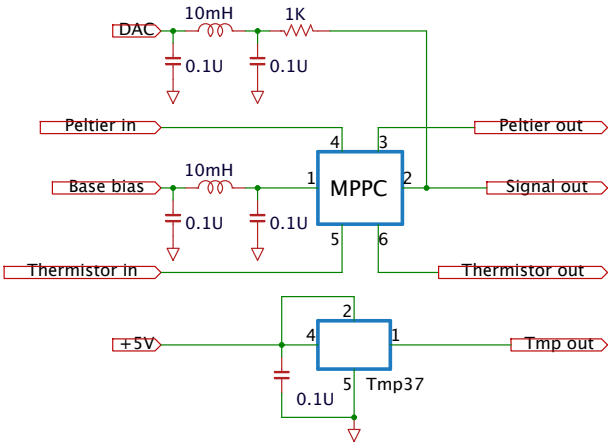

Figure 5.2.1: The circuit of the MPPC mounted board.

We develop the 50-fold preamplifier since the gain of the MPPC is not large enough to record one-photoelectron signal for the data acquisition system for KOTO. The details of the requirements for the preamplifier are described in Sec. 5.5.1. The circuit of the preamplifier is shown in Fig. 5.2.2. The input signal shown as "In" is received via an AC coupling to eliminate the voltage offset caused by "DAC" in Fig. 5.2.1. The signal is then amplified by a 10-fold non-inverting amplifier. Next, the signal is amplified by a 5-fold differential amplifier, and the output of the differential signal is shown as two of "STP" in Fig. 5.2.2. The differential outputs are used to reduce the electrical noise in the transmission[4)].

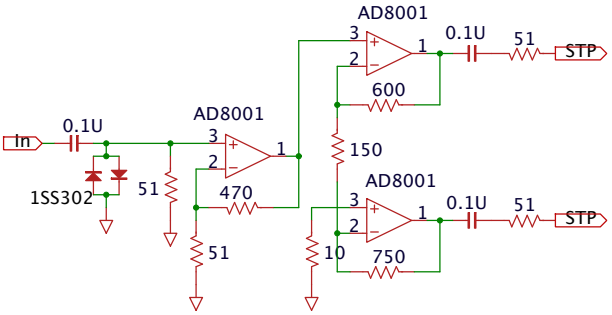

Figure 5.2.2: The circuit of the preamplifier.

The differential signals are sent to the 125 MHz ADC [41] through a shielded twisted pair (STP) cable, and converted to a unipolar signal in the ADC. Figure 5.2.3 shows a waveform of the CV by a charged particle [5)]. The black line shows an output of the preamplifier. The dots indicate the data recorded by the 125 MHz ADC. The ADC shapes the signal waveform with a 10-pole Bessel filter and

[4)]The transmission distance of the signal is 50 m in KOTO.
[5)]Both waveforms are obtained by averaging over 10000 pulses.

records pulse heights at 64 points.

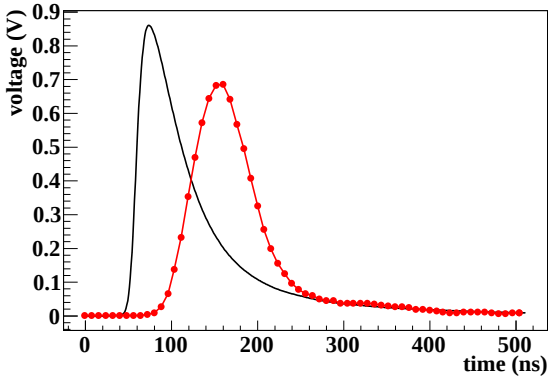

Figure 5.2.3: An example of the CV pulse shape. The black line shows an output of the preamplifier. The dots indicate data recorded by the 125 MHz ADC.

5.3 The control system for the readout system

The MPPCs and the preamplifiers are located in a vacuum chamber, and can't be accessed when the KOTO experiment is running with the K_L beam. We develop a remote control and monitor system for the readout system. The control system is designed to control the applied voltage and the temperature of the MPPCs individually. A diagram of the control system is shown in Fig. 5.3.1. The control system is located out side of the vacuum chamber. The control system consists of six modules, and each module is named the CV controller. The CV controllers are controlled by a PC using an Universal Serial Bus (USB) interface. One CV controller monitors and controls 32 channels of the MPPCs and the preamplifiers. The control signals from the CV controller are transmitted to the MPPCs through 26-pin flat cables, and to the preamplifiers through LAN cables. One CV controller consists of one mother board, four MPPC daughter boards, four MPPC sub cards, and one AMP daughter board.

The mother board has a micro-controller to control the MPPC daughter boards and the MPPC sub cards with Serial Peripheral Interface (SPI) communication.

The MPPC daughter board has a DAC[6)] to control the applied voltage and the temperature of the MPPCs. The DAC outputs are connected to "DAC" shown in Fig. 5.2.1, and control the applied voltage of the MPPCs. The DAC outputs are also connected to the voltage control circuit for the Peltier device. The MPPC daughter board has an ADC[7)] to monitor the various outputs and voltage lines as shown in

[6)] It has 32 outputs, and has 5 V range with 14 bit.
[7)] 8bit, 5 V range.

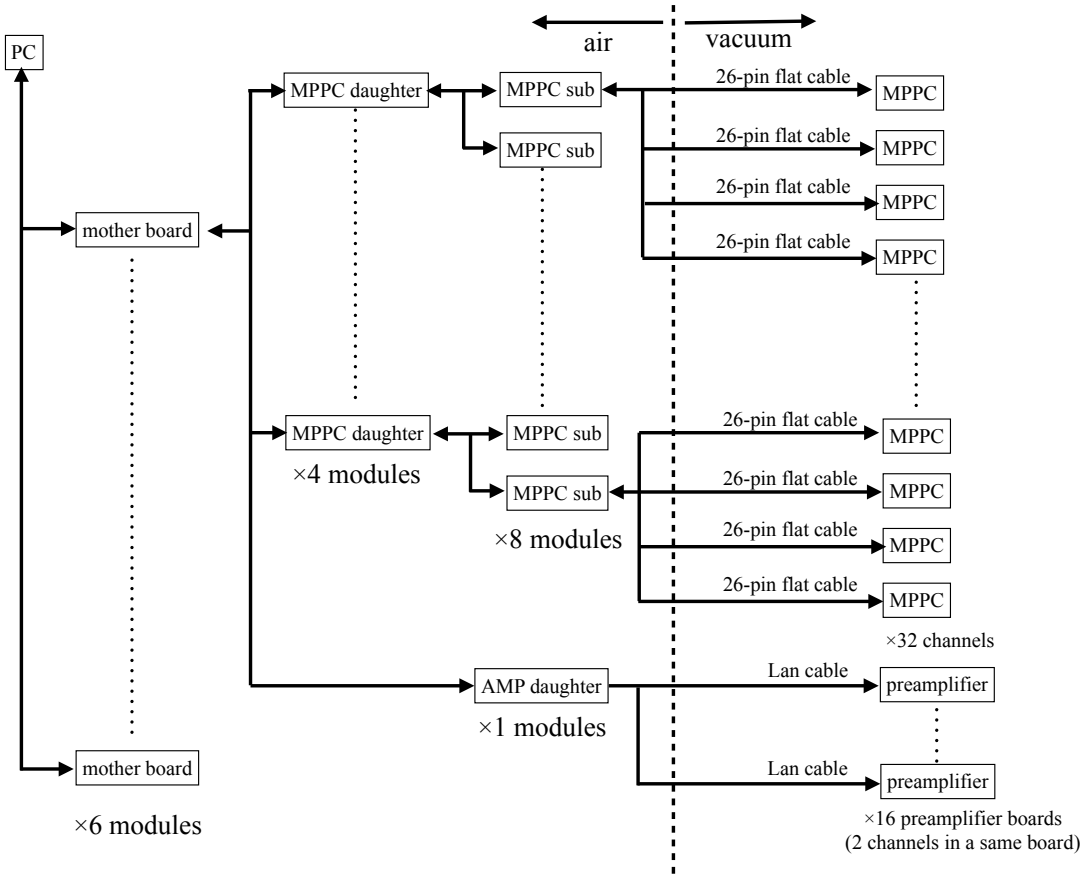

Figure 5.3.1: The diagram of the control system.

Table 5.3.1.

The MPPC sub card has the voltage control circuit for the Peltier device as shown in Fig. 5.3.2. We control the temperature of the MPPC through the comparison between the DAC output and the thermistor output.

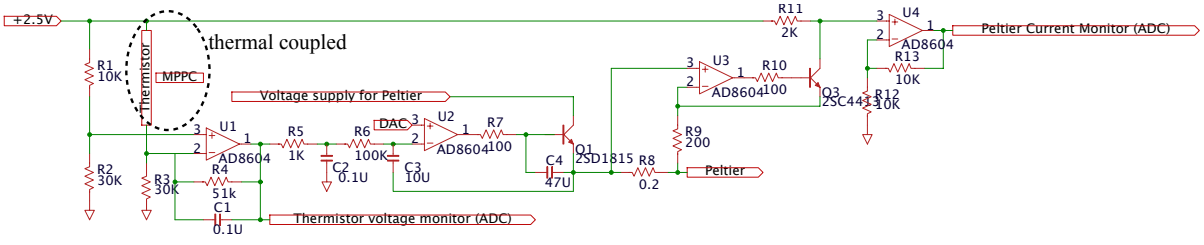

Figure 5.3.2: The voltage control circuit for the Peltier device.

Table 5.3.1: List of the monitor in one CV controller.

value	number of channel / one controller
DAC for the MPPC	32
Base bias voltage of the MPPC	4
DAC for the Peltier device	32
Output of the thermistor	32
Current of the Peltier device	32
Voltage of the Peltier device	32
Output of the thermo censor	32
Supply voltage for the passive element	12

The AMP daughter board distributes the voltage to the preamplifier.

The CV controller is controlled and monitored with a software running on a PC. The user interface window is shown in Fig.5.3.3. In the operation of the CV, the values shown in Table 5.3.1 are monitored, and a warning message is displayed in a terminal window if an unusual value is detected.

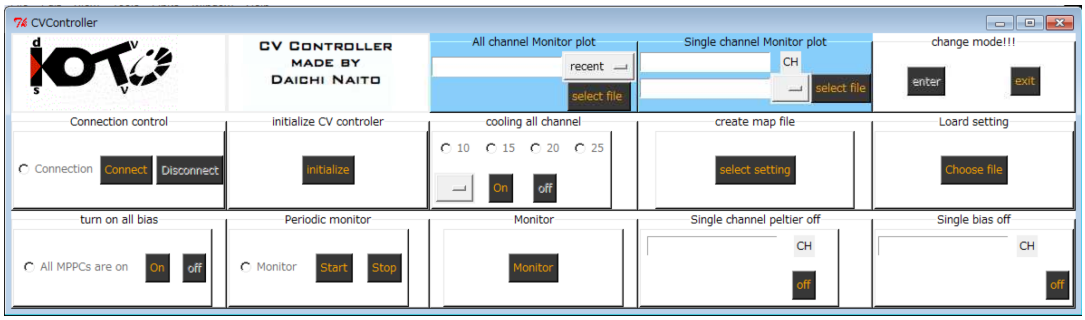

Figure 5.3.3: Screen shot of the window to control and monitor the CV controller.

5.4 Measurement of the MPPC characteristics

We measure the characteristics of the MPPCs before the installation to the CV. We measure the voltage dependence of the gain of the MPPC and the temperature dependence of the breakdown voltage to determine the applied voltage. We measure the temperature dependence of the dark count noise to check the noise rate. We measure the temperature dependence of the thermistor output to set the output voltage of the DAC for the control of the Peltier device. The MPPCs are put in a thermostat bath [8)], and these characteristics are measured at 20 °C, 12 °C, and 5 °C. Signals from the MPPCs are amplified by

[8)] Stability of the temperature in the thermostat bath is approximately ± 0.1 °C.

50 times with a preamplifier (TKY-0351). One hundred eight-four MPPCs are used in the CV, and two hundred including spares are measured.

We measure G_{signal} and the breakdown voltage by using a LED. The signals from the MPPCs are recorded by a charge-integrating ADC synchronized with the LED signal. Figure 5.4.1 shows the ADC spectrum of one MPPC [9]. The first peak is a pedestal (P_{ped}) and the second peak is a one-photoelectron signal (P_{one}). G_{signal} is calculated as the following equation by using electric charge per ADC count (C_{ADC}).

$$G_{signal} = (P_{one} - P_{ped}) \times C_{ADC}/C_e. \tag{5.2}$$

The difference of ADC values between two peaks is 20 counts in Fig. 5.4.1, and C_{ADC} is 5 fC. G_{signal} is calculated to be 6×10^5. Figure 5.4.2 shows the voltage dependence of G_{signal}. G_{signal} varies by ~120%/V. The breakdown voltage is calculated as the intercept of x axis, and is 69.75±0.02 V. We calculate the breakdown voltages of all the MPPCs with this method. Figure 5.4.3 left shows the temperature dependence of the breakdown voltage for the 200 MPPCs. The break down voltages of all MPPCs are located in the region between 69.5 V and 70.4 V at 10 °C, and we calculate the applied voltages of all the MPPCs. Figure 5.4.3 right shows the slope of the temperature dependence of the breakdown voltage for 200 MPPCs. The breakdown voltage varies ~ 60 mV/°C. With the measured break down voltage and G_{signal}, the applied voltage of the MPPC is adjusted so that the over voltage of the MPPC is set to a specific value in the actual experiment[10].

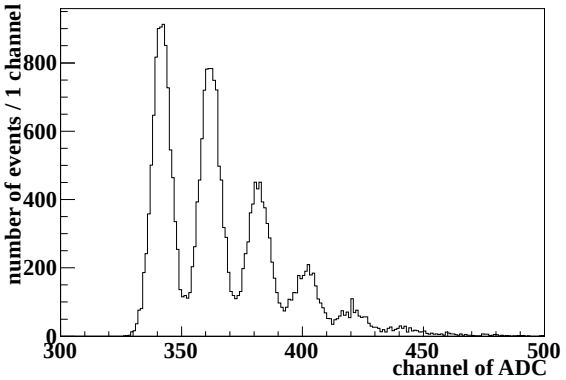

Figure 5.4.1: ADC spectrum of one MPPC.

The dark count noise rate with the 0.5 p.e. threshold is measured by using the charge-integrating

[9] Ambient temperature is 5 °C.

[10] In the evaluation of the CV performance, the over voltages of all the MPPCs are adjust to be 1.5 V. In the physics run, the over voltages are adjust to be the range of the voltage between 1.5 V and 1.8 V so that the signal amplitude of the CV strips by a charged particle are same value.

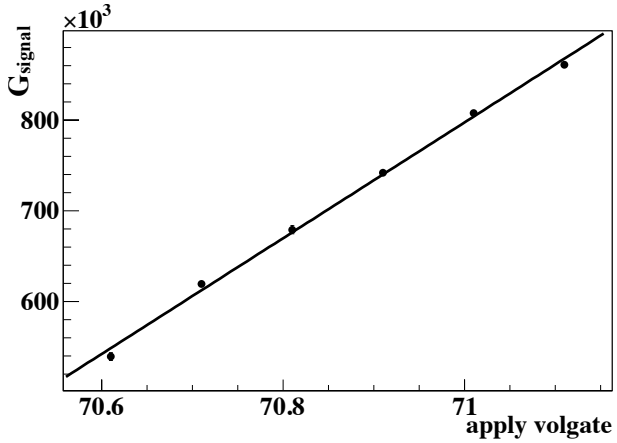

Figure 5.4.2: Voltage dependence of the G_{signal}.

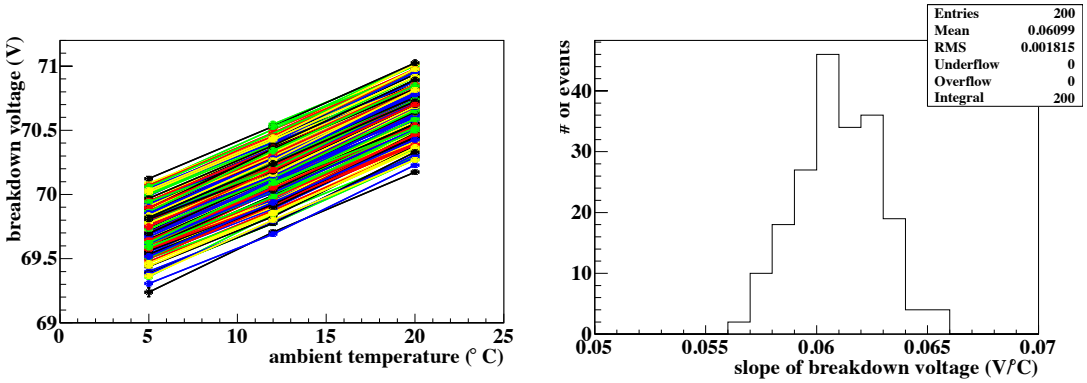

Figure 5.4.3: Temperature dependence of the breakdown voltage for 200 MPPCs (left). The slope of the temperature dependence of the breakdown voltage for 200 MPPCs (right).

ADC with a random trigger. Figure 5.4.4 shows the dark count noise rate as a function of ambient temperature for 200 MPPCs [11]. The dark count noise rate becomes almost half when the MPPC is cooled from 20 °C to 10 °C. Figure 5.4.5 shows the dark count noise rate as a function of the over voltage at 12 °C. With the over voltage below 2V, the noise rates are less than 500 kHz, and the effect of mis-calculation of the energy deposit is estimated to be 1 keV[12]. The effect of 1 keV is negligibly small to the energy threshold of 100 keV for the charged partcle.

We calibrate the thermistors by using the thermostat bath. Output of the thermistor is measured by

[11] over voltage=1.5V. Points in one MPPC are simply connected with a line.

[12] The probability overlapping the dark count noise with the waveform recorded by the 125 MHz ADC is calculated to be 0.22 ($= 1 - exp(-8ns \times 64 \times 500kHz)$). The energy deposit per units in light yield is 6 keV/1p.e. since the light yield of the CV is measured to be 16.3p./100 keV in Sec. 4.3.2. The expected value of the energy deposit by the dark count noise is calculated to be 1.2 keV ($= 0.22 \times 6keV/1p.e.$) since the single photoelectron dominates the dark count noise.

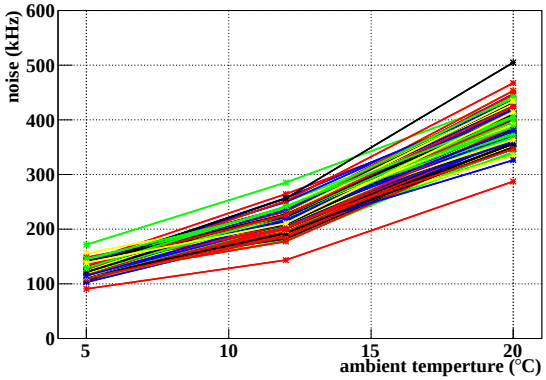

Figure 5.4.4: Dark count noise rate as a function of ambient temperature with the 200 MPPCs.

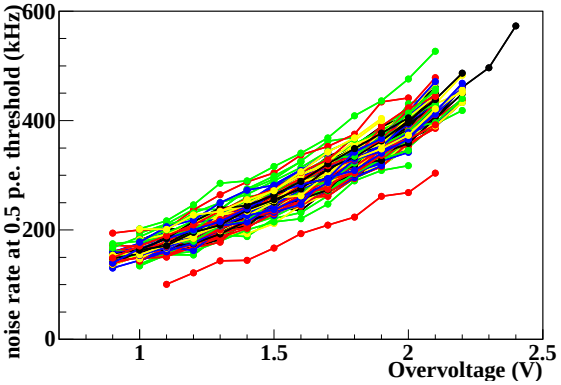

Figure 5.4.5: Distribution of dark count noise rate with 0.5 p.e. threshold.

a slow ADC. Figure 5.4.6 shows the temperature dependence of one thermistor output. The distribution is fit by an exponential function considering the circuit as shown in Fig. 5.3.2. We use the mean of fit parameters of 200 MPPCs to calculate the MPPC temperature. The temperature of the MPPC calculated from the thermistor output and the fitting function are shown in Fig. 5.4.7. The accuracy of the calculated temperature is 0.15 °C, and is acceptable in KOTO[13)].

We check the operation of the Peltier device in air, and the MPPCs in a vacuum. The MPPCs are put in the thermostat bath, and cooled from 20 °C to 5 °C by using the voltage control circuit. We record the varies of temperature of the MPPCs by an oscilloscope, and confirm that all the MPPCs are cooled from 20 °C to 5 °C. Figure 5.4.8 shows one-photoelectron signal in a vacuum. The MPPCs are put in

[13)]The uncertainty of the break down voltage by the temperature calculation is 9 mV (=60 mV/°C×0.15), while the statistical uncertainty of the calculation of the break down voltage is 30 mV. The thermistor has enough accuracy to calculate the break down voltage.

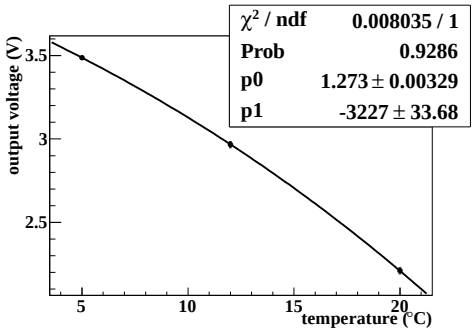

Figure 5.4.6: Temperature dependence of one thermistor output.

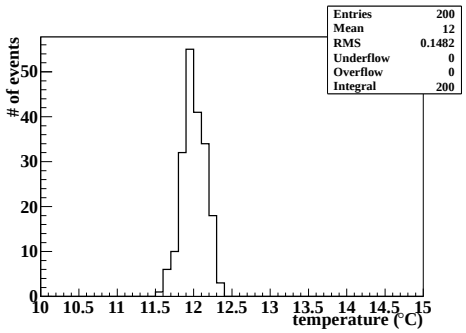

Figure 5.4.7: The temperature of the MPPC calculated from the thermistor output and the fitting function at 12 °C.

a small vacuum chamber and evacuated to 100 Pa, and checked whether one photoelectron is clearly observed[14)]. We test the operation of all the MPPC in a vacuum in this way.

5.5 Evaluation of the performance of the preamplefier

We evaluate the performance of the preamprefier before installation.

5.5.1 Requirements for the preamplifier

There are four requirements: the gain, the bandwidth, the dynamic range, and the power consumption. Table 5.5.1 shows summary of the requirements. To achieve the four requirements, we develop the amplifier as shown in Fig. 5.2.2. The preamplifier consists of only three low power Op Amp of AD8001 to achieve low power consumption. We optimize the parameter of passive components and a layout of a PCB board to achieve high speed and high gain.

[14)]The noise level in the small vacuum chamber is too large to calculate G_{signal}.

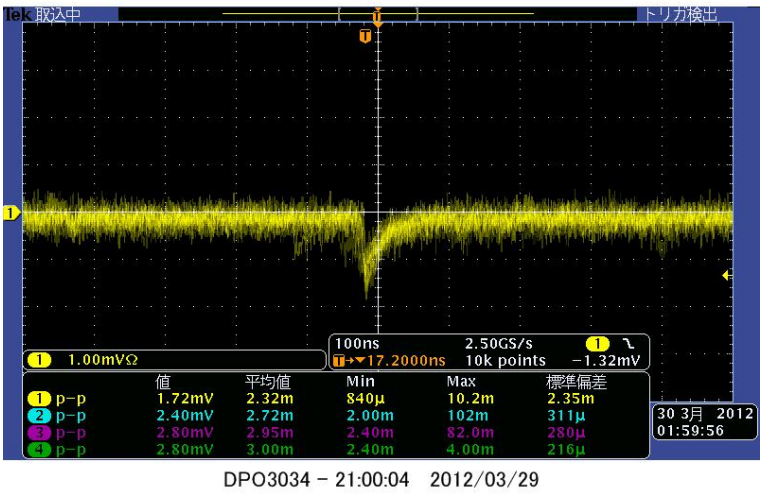

Figure 5.4.8: One photoelectron signal of the MPPC in a vacuum.

Table 5.5.1: Summary of the requirements of the preamplifier.

Gain	> 50
Band Width	> 100 MHz
Output dynamic range	>800 mV
Power consumption	< 200 mW

The preamplifier is designed to have more than 50-fold gain in order to amplify the output of the MPPC so that the one-photoelectron signal is resolved in the waveform recorded by the 125 MHz ADC.

The preamplifier is designed to have better than 100 MHz bandwidth. Figure 5.5.1 left shows an example of the CV waveform without the preamplifier by a 600 MeV/c positron at the Research Center for Electron Photon Science (ELPH) of Tohoku University. In Fig. 5.5.1, the rise time of the waveform is 15.5 ns. Figure 5.5.1 right shows the distribution of the rise time with the waveforms of many events. The rise time is 15.5 ± 0.4 ns with all the pulse. We find the 95 % of the frequency in the leading edge of the signal is less than 75 MHz [15)], and we set the requirement of the bandwidth better than 100 MHz.

The preamplifier is designed to have a dynamic range greater than 800 mV. Figure 5.5.2 shows the distribution of the pulse height without the preamplifier obtained with a 600 MeV/c positron at the ELPH. A typical pulse height of the CV waveform is ~ 5 mV in Fig. 5.5.2, and the typical pulse height becomes 250 mV at the output of the preamplifier with the gain of 50. We set the requirement

[15)] We assume an expornential function whose time costant is 65.5 MHz (=1/15.5ns).

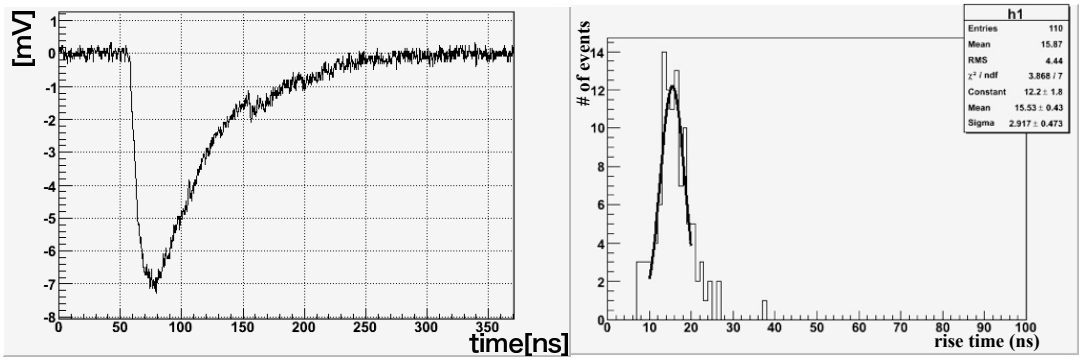

Figure 5.5.1: A CV waveform by a charged particle without the preamplifier (left). The distribution of the rise time with the waveforms of many events (right). The black line shows a Gaussian function.

of the dynamic range equivalent to 3 times of the typical pulse height since we use the energy peak corresponding to the typical pulse height for the energy calibration of the CV.

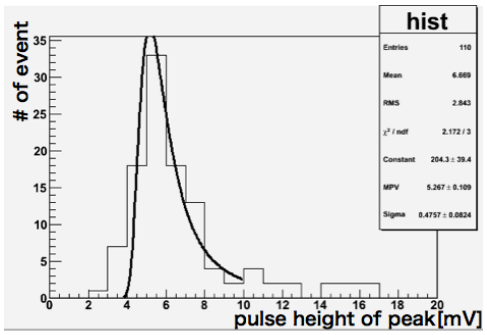

Figure 5.5.2: The distribution of the pulse height without the preamplifier obtained with a 600 MeV/c positron at the ELPH. The black line shows a landau function.

The power consumption of the preamplifier is designed to be less than 200 mW[16)].

5.5.2 Measurement of the preamplifier performance

For the preamplifiers, its gain, response to a test pulse input, dynamic range, power consumption, and noise level are measured before the installation. One hundred eight-four preamplifiers are used in the CV, and one hundred nine-six including spares are measured.

[16)]Since the preamplifiers are put in the vacuum, the power consumption of the preamplifier increases the temperature of the MPPC mounted board through the support structure of the CV. The MPPC mounted board is thermally connected to the heat radiation side of the Peltier device, and the temperature control system does not work when the temperature of the radiation side is more than 30 °C. We estimate the heat transfer from the preamplifier to the MPPC mounted board in a simulation, and we set the requirement of the power consumption so that the temperature of the radiation side is less than 30 °C.

The distribution of the gain of the preamplifiers are shown in Fig. 5.5.3. The mean of the gain is 50.8, and RMS of the gain is ±0.4. One hundred ninety five preamplifiers achieve the gain greater than 50 fold.

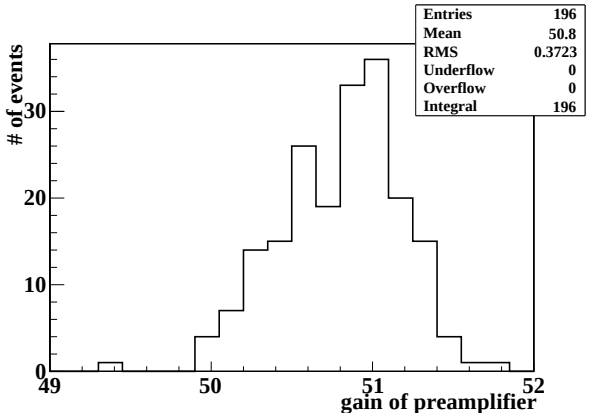

Figure 5.5.3: The distribution of the gain of the preamplifiers.

We measure the rise time of output pulse. We use a test pulse with the rise time of 3 ns and the fall time of 30 ns as it is designed. Figure 5.5.4 left shows an output waveform of the preamplifier. We fit the output waveform by a convolution function of exponential functions. The rise time is 2.5 ns in Fig. 5.5.4 left. Figure 5.5.4 right shows the distribution of the rise time for 196 preamplifiers. The mean rise time is 2.5 ns, and the RMS is ±0.08 ns. The preamplifier achieves good frequency response equivalent to 140 MHz[17]. The variation of the gain as a function of frequency is measured for a preamplifier by a spectrum analyzer as shown in Fig. 5.5.5. The variation of the gain (G_V) is defined as follows by using the nominal gain (G_n) and the gain as a function of the frequency (G_f).

$$G_V = 20log(G_f/G_n) \tag{5.3}$$

The bandwidth of the preamplifier is approximately 200 MHz [18]. We confirm that the preamplifiers have the bandwidth of 100 MHz.

We measure the nonlinearity of the gain to evaluate the dynamic range. The non-linearity is defined as the fractional deviation of the measured gain from the expected one. We input a 10-MHz sine wave with various amplitude. Figure 5.5.6 left shows the nonlinearity as a function of the input amplitude. Figure 5.5.6 right shows the distribution of the maximum nonlinearity for 196 preamplifiers. The mean of the maximum nonlinearity is 0.3±0.1% in the range of the output from -1.25 V to 1.25 V. We find the nonlinearity is acceptable in KOTO[19].

[17] It is the maximum frequency within the 95 % of the frequency in the leading edge.
[18] The zero to -3 db bandwidth.
[19] The nonlinearity is negligibly small to the flucutuation of the energy deposit of the CV as shown in Fig. 5.6.3.

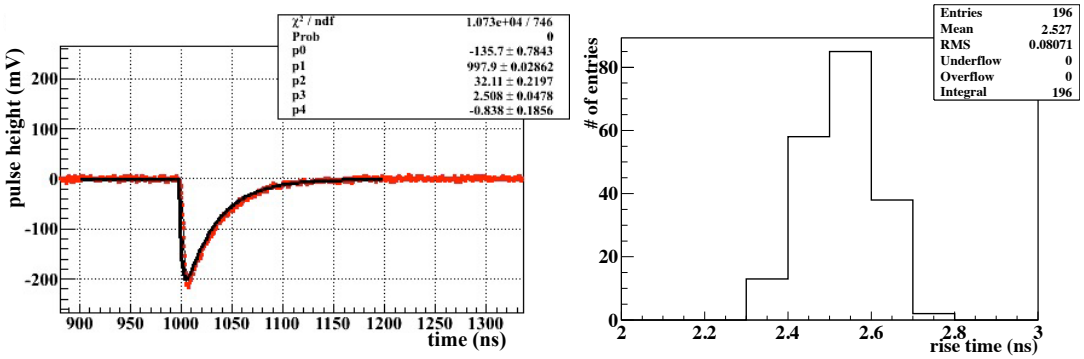

Figure 5.5.4: An output waveform of the preamplifier (left). The distribution of the rise time of 196 preamplifiers (right).

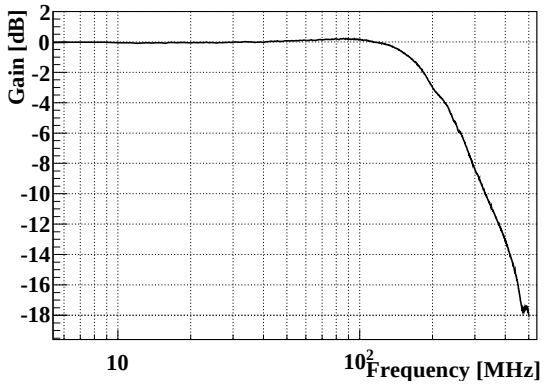

Figure 5.5.5: The variation of the gain of the preamplifier as a function of frequency.

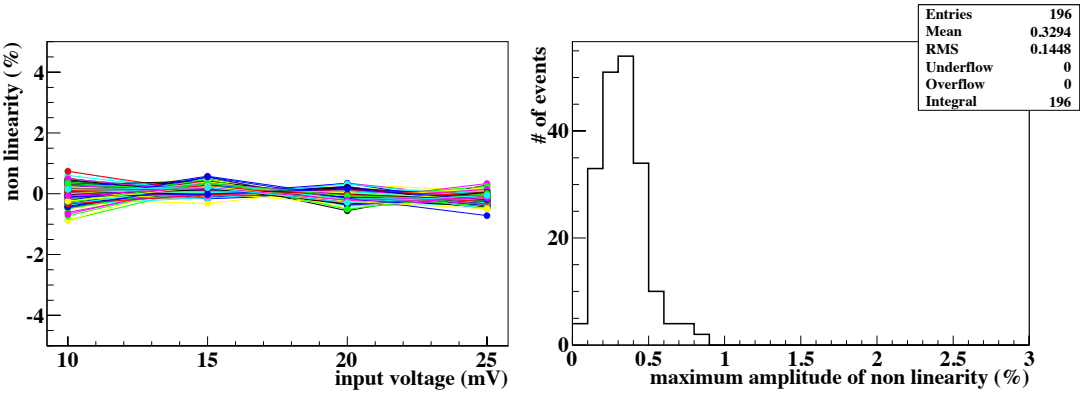

Figure 5.5.6: The nonlinearity as a function of the input amplitude (left). The maximum nonlinearity for 196 preamplifiers (right).

We measure the power consumption. Figure 5.5.7 shows the distribution of the power consumption for 98 samples of boards where two preamplifiers are mounted. The mean power consumption of single amplifier is 156.7 mW, and the RMS is ±0.4 mW. All the preamplifiers satisfy the requirement of the power consumption.

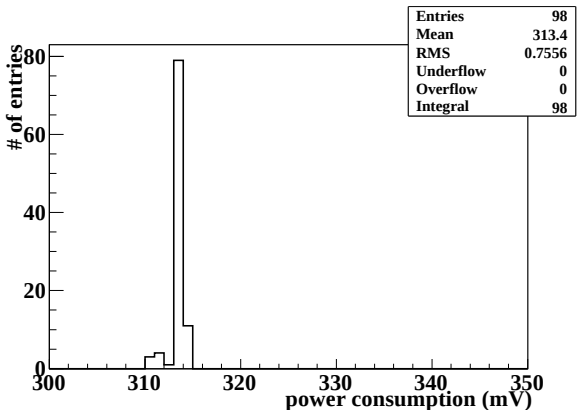

Figure 5.5.7: The distribution of the power consumption for 98 samples of a board where two preamplifiers are mounted.

We evaluate the noise level[20)]. Figure 5.5.8 shows the distribution of the noise level, and the mean of the noise level is 2.4 ± 0.02 mV. Figure 5.5.9 shows the ADC spectrum of the MPPC signal amplified with the preamplifier and recorded by the 125 MHz ADC with a LED signal. The one-photoelectron peak is clearly resolved, and the noise level of the preamplifier is acceptable in KOTO.

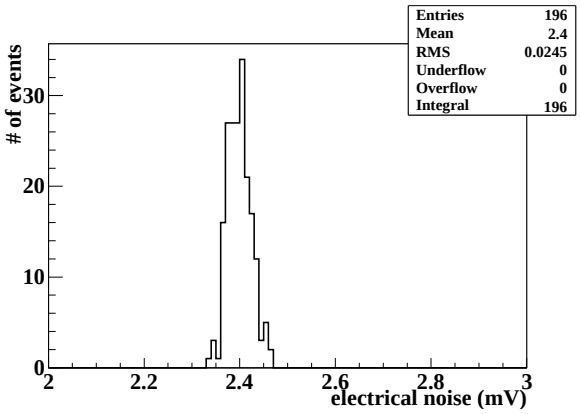

Figure 5.5.8: The distribution of the noise level of the output of the preamplifier.

Summary of the performance test is shown in Table 5.5.2. The preamplifiers satisfy all the require-

[20)] noise level means RMS in 1 μs time range.

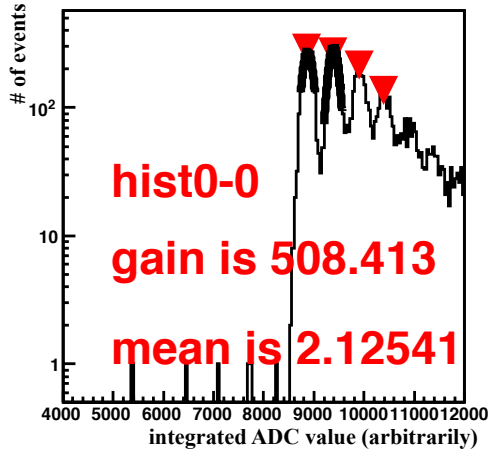

Figure 5.5.9: the ADC spectrum of the MPPC signal amplified by the preamplifier and recorded by the 125 MHz ADC synchronized with the LED signal.

ments in KOTO.

Table 5.5.2: Summary of the performances the performance test.

	achieved value	required value
Gain	51	> 50
Band Width	200 MHz	> 100 MHz
Output dynamic range	2.5 V	> 800 mV
Power consumption	150 mW	< 200 mW
Noise	2.4 mV (RMS)	

5.6 Installation and operation of the readout system

In the construction of the CV, the MPPCs and the preamplifiers are installed and the signals from the preamplifiers are checked. The CV is installed in the KL beamline, and we evaluated the CV performance as reported in Chap. 6. We find that the signals from all MPPCs with preamplifiers are correctly readout, and the one-photoelectron signal is observed. After the evaluation of the CV, the CV is installed in the KOTO detector, and we carry out the engineering run for the KOTO detector and the first physics run. We operate all MPPCs and the preamplifiers in a vacuum with the CV controller. We check the operation of the MPPC and the preamplifier, and the operation of the cooling system.

We estimate the gain of the MPPC in the first physics run of KOTO from the applied voltage of the MPPC and the results of the measurement of the MPPC characteristics. We evaluate the deviation of

the measured gain from the expected gain in the first physics run of KOTO as shown in Fig. 5.6.1[21]. The RMS is 4.7% and is equivalent to 40 mV of accuracy in the calculation of the applied voltage of the MPPC. The gain accuracy is comparable to the statistical uncertainty of ~ 30 mV in the calculation of the applied voltage of the MPPC, and we conclude that the MPPCs are correctly applied the expected voltage and the preamplifiers are correctly operated.

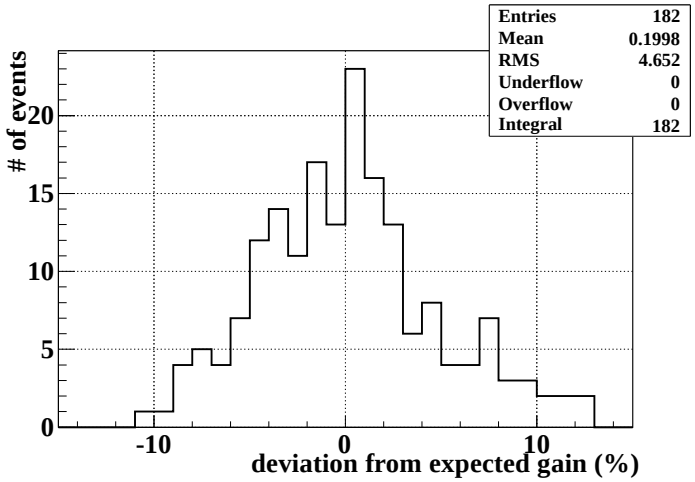

Figure 5.6.1: The deviation of the gain from the expected gain in the first physics run of KOTO.

The temperature variation of the inner most strip of the front CV in the engineering run is shown in Fig. 5.6.2. The temperature variation of the MPPC mounted board (black) and that of the thermistor (red) are shown. The temperature of the MPPC mounted board varies from 16.5 °C to 18 °C, while the temperature of the thermistor is kept to be 10±0.01 °C. The Cooling system works well.

The variation of the signal amplitude of the CV by a charged particle at the inner most strip of the front CV in the engineering run is shown in Fig. 5.6.3. The variation is within 2 % and agree with the statistical uncertainty. We conclude that the temperature dependence of the photon detection efficiency and G_{signal} are negligible in the CV by keeping the temperature of the MPPC.

[21] The signals of the two channels are not readout by mis-cabling.

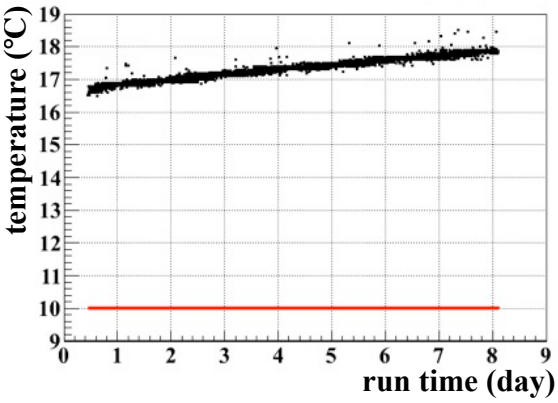

Figure 5.6.2: The temperature variation of the MPPC mounted board (black) and that of the thermistor (red) in the engineering run. The horizontal axis shows the run time, and vertical axis shows the temperature.

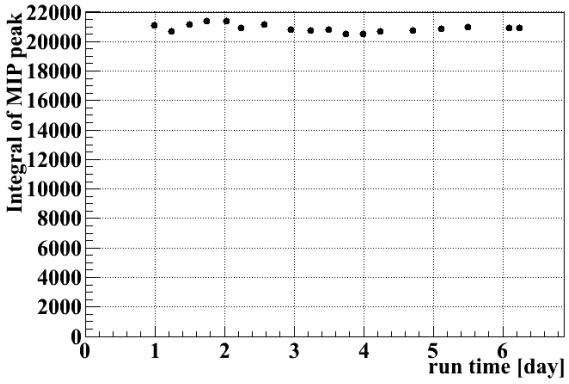

Figure 5.6.3: The variation of the signal amplitude of the CV by a charged particle at the most inner strip of the front CV in the engineering run. The statistical uncertainty is equivalent to the size of points.

Chapter 6

Evaluation of the CV performance

We evaluate the CV performance with the charged particles from K_L decays in the special experimental setup as described in Sec. 2.3. We measure the inefficiency for the charged particles penetrating the CV, and it is defined as the penetrating BG. We check that the light yield of the CV is high enough to identify the major background process from the $K_L \to \pi^- e^+ \nu$ decay (Ke3BG) and the $K_L \to \pi^+\pi^-\pi^0$ decay (Kπ3 BG) as explained in Sec. 3.1.2. We also check the timing resolution of the CV that affects the signal loss by accidental activity. The position reconstructions of charged particles are described in Sec. 6.1. Basic performance of the CV, light yield and timing resolution, are studied in Sec. 6.2. Energy calibrations of detectors are described in Sec. 6.3. We develop simulations for the inefficiency measurement in Sec. 6.4. Inefficiency of the CV is studied in Sec. 6.5. We examine systematic uncertainties for the inefficiency measurement in Sec. 6.6.

6.1 Reconstruction of the hit positions in the CV, the hodoscope, and the calorimeter

Charged particle tracks are reconstructed by the drift chambers and the hodoscope. The track is extrapolated to the CV and to the calorimeter, and the hit position of the track on each detector is called "extrapolated position". The hit position at the calorimeter is also reconstructed with the hit patterns of the crystals in the calorimeter clusters, and it is called "clustered position". We describe the reconstruction of the extrapolated position and the clustered position. We correct the extrapolated position on each detector since it does not correspond to the actual hit position of the track on each detector in the KOTO coordinate described in Sec. 2.1.1[1)].

[1)]The center position of the calorimeter in the xy plane is defined as the center of the xy plane in the KOTO coordinate. The hodoscope and the CV are aligned to the center of the calorimeter, while the chambers are aligned to the center of the KL beamline. The center of the KL beamline was shifted from the designed center by the earthquake in Mar 2011.

6.1.1 Position reconstruction on the CV, the hodoscope and the calorimeter

The experimental setup is described in Sec. 2.3. First, we reconstruct the extrapolated position on the CV, the hodoscope, and the calorimeter. In each chamber, 2 to 4 hit cells in x and x' (or y and y') planes are clustered, and a hit position of a charged particle in X (or Y) plane is calculated from drift-time information. To reconstruct two charged tracks from the K_L decays, each X and Y plane is required to have more than two clusters. Three clusters are selected from three X (Y) planes one by one, and fit with a line function to reconstruct the trajectory of the charged particle in X (Y) axis.We select the trajectories with the χ^2 of the line fitting less than 10. From all the combinations of the trajectories, two-track pairs are reconstructed. We determine a correct two-track pair by requiring hits of the hodoscope at the extrapolated position, and requiring both extrapolated positions to be in diagonal on the hodoscope as shown in Fig. 2.3.5.

The hit position on each layer of the CV is defined as the extrapolated position on the upstream surface of each layer. The hit position on the calorimeter is defined as the extrapolated position at the center of the calorimeter in the z direction[2)]. Next, we reconstruct the clustered position in the calorimeter. We reconstruct the cluster of the CsI crystals with energy greater than 10 MeV. The crystals close to each other are grouped to form a cluster, where the distance from one crystal to the nearest crystal in the cluster is less than 71 mm. The clustered position is calculated as the energy weighted mean of the crystals.

6.1.2 Correction for the extrapolated position on the CV, the hodoscope, and the calorimeter

We calculate the position difference between the extrapolated position and the hit position of the track on each detector. We evaluate the misalignment of each detector by the calculation of the position difference. The extrapolated position is corrected by subtracting the position difference.

CV

The distribution of the extrapolated position on the front CV around the beam hole is shown in Fig. 6.1.1. The black line shows the envelope of the inner most strip. We measure the projection of the extrapolated position in the y axis. We calculate the center position of the strip in the projection. The difference between the extrapolated center and the design value is considered as an offset of the strip. The offset is measured every 50 mm along the strip to evaluate the rotation of the strip.

[2)]The extrapolated position on the calorimeter corresponds to the energy weighted hit position of charged particles penetrating the calorimeter.

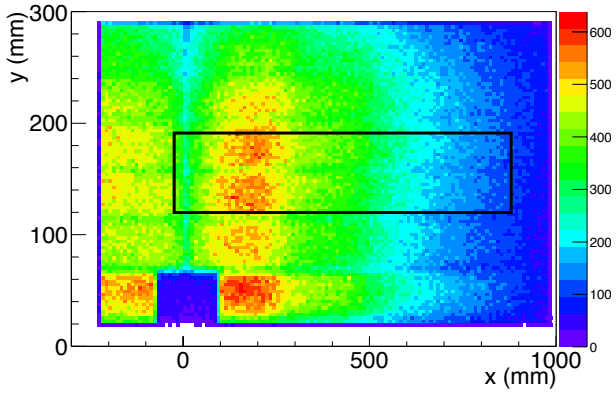

Figure 6.1.1: The distribution of the extrapolated position at the inner most strip of the front CV. The black line shows the envelope of the inner most strip. The contrast in the inner part of the distribution is determined with the geometrical acceptance of the hodoscope and the efficiency of the track reconstruction in the chambers. The difference between inner part and outer part is determined with the position distribution of charged particles from the K_L decay.

The extrapolated center in each 50-mm step is calculated as follows. Figure 6.1.2 shows the distribution of the extrapolated position of the inner most strip in the y axis at x = 0 mm. The black line shows the distribution without any cut. The red line shows the distribution with a cut on the energy loss in the strip. The green line shows the ratio between the black line and the red line. The blue line indicates the designed center. The extrapolated center is calculated as the mean of two edges in the green distribution. The shape of the edge is fit by a convolution of the square wave with a Gaussian. The Gaussian is used to take into account the resolution of the extrapolated position on the CV, and the sigma of the Gaussian is 1.5 mm in Fig. 6.1.2. The strip offset is calculated to be -7±0.06 mm in Fig. 6.1.2 where the error is statistical.

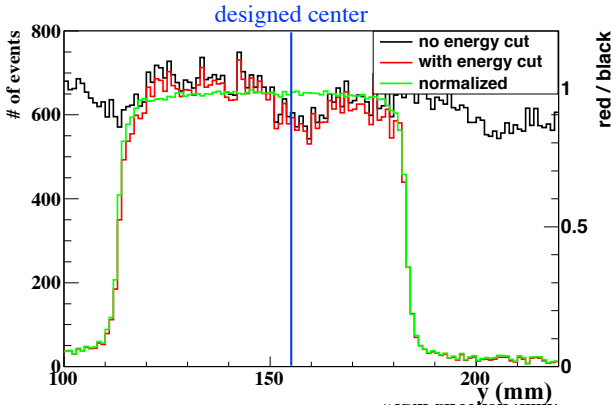

Figure 6.1.2: The distribution of the extrapolated position of the inner most strip in the y axis where the position in the x axis is 0 mm.

We calculate the position dependence of the strip offset as shown in Fig. 6.1.3. The left plot shows the dependence of the x offset in the y axis, and the right plot shows the dependence of the y offset in the x axis. In Fig. 6.1.3, we find that the front CV rotates $\sim 0.1°$, and the rear CV rotates $\sim -0.05°$ in the xy plane. These rotations are evaluated as the systematic source in the inefficiency analysis, and found to be negligible. The x(y) offset of each CV layer is defined at y(x) = 0 mm. The offset of the front CV is (x, y) = ($+9.8^{+1.0}_{-0.8}$, $-6.9^{+0.6}_{-0.9}$), and that of the rear CV is ($+9.1^{+0.6}_{-0.6}$, $-7.9^{+0.3}_{-0.5}$). The error of the x(y) offset is assigned to cover the strip offsets in the range of -850 mm < y(x) < 850 mm.

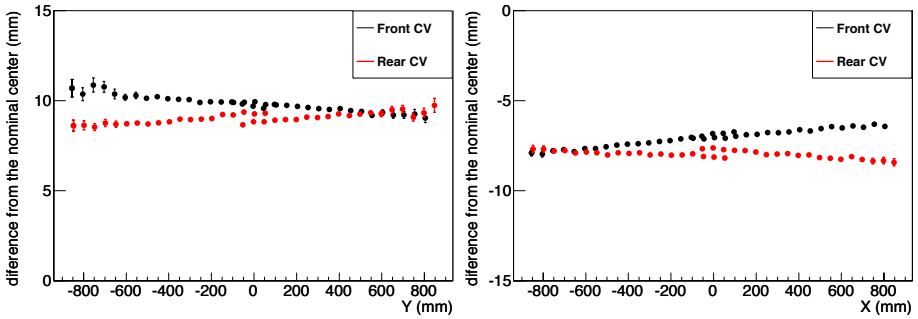

Figure 6.1.3: The position dependence of the x offset in y axis (left). The position dependence of the y offset in the x axis (right).

hodoscope

We evaluate the offset of the hodoscope in the same way as the CV. Figure 6.1.4 left (right) shows the x (y) offsets of eight (ten) hodoscope modules[3)]. The horizontal axis shows the center position of each module in the y axis. The x(y) offset of the hodoscope is assigned with the mean of all x(y) offsets and the errors covering all the strip offsets in the region of -850 mm < y(x) < 850 mm. The hodoscope offset is (x, y) = ($+13.94^{+7}_{-6}$, -23.6^{+7}_{-3}). These errors are evaluated as the systematic source in the inefficiency analysis, and found to be negligible.

Calorimeter

For the calorimeter, we evaluate the difference between the extrapolated position and the clustered position. The distribution of the difference in the x direction (left) and that in the y direction (right) are shown in Fig. 6.1.5. The peak position in the distribution is defined as the offset of the calorimeter. The offsets of the calorimeter are (x, y) = (10.5±0.2, -7.8±0.08), and the errors are statistical.

[3)]The four of inner most and outer most modules have no edge in x axis. The two of outer most modules of the hodoscope have no edge in y axis

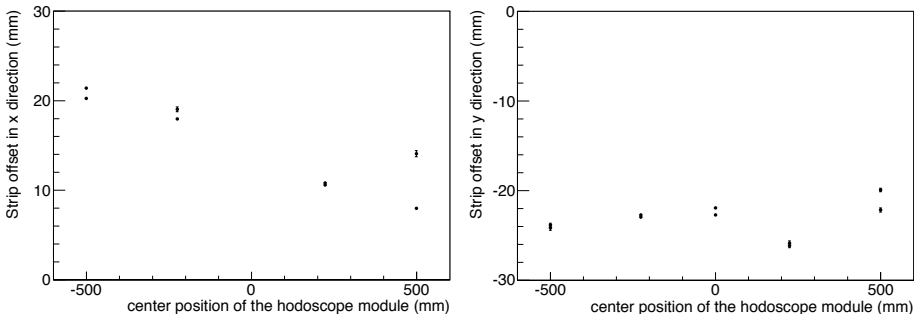

Figure 6.1.4: The x offset of the hodoscope for 8 modules (left). The y offset for ten modules (right).

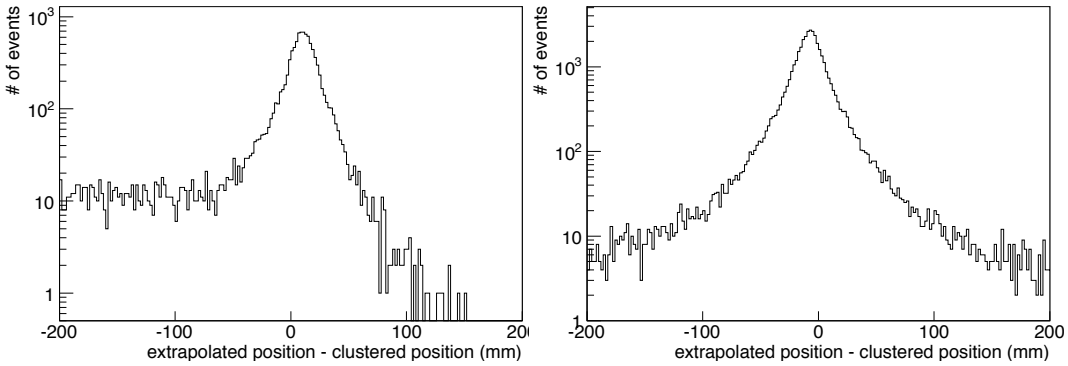

Figure 6.1.5: The difference between the extrapolated position and the clustered position in the x direction (left) and in the y direction (right). The extrapolated position in the x axis is limited to be ~ 0 mm since we require the incident angle of the track within ± 0.1 degree to reject angle dependence of the difference, while the clustered position varies from 50 mm to 850 mm as shown in Fig. 2.3.2. As a result, there is asymmetry in the x direction.

Summary of the offset

Table 6.1.1 shows the offset of each detector for the extrapolated position. The correction is applied to the data, and each detector is shifted with each offset in a simulation.

Table 6.1.1: List of the offsets.

detector	offset (x, mm)	offset (y, mm)
Hodoscope	+13.94	-23.6
Front CV	$+9.8^{+1}_{-0.8}$	$-6.9^{+0.6}_{-0.9}$
Rear CV	$+9.1^{+0.6}_{-0.6}$	$-7.9^{+0.3}_{-0.5}$)
Calorimeter	10.5±0.2	-7.8±0.08

6.2 Basic performance of the CV

The CV is required to have light yield of more than 10 p.e./100 keV and the timing resolution better than 3 ns. Since the light yield of the CV strip depends on the hit position of a charged particle, we evaluate the light yield as a function of the extrapolated position. We also check the timing resolution of the CV.

6.2.1 Light yield

The light yield is calculated from the waveform recorded with the 125 MHz ADC. The ADC records 64 samples of pulse height in one waveform. We first integrate the ADC values corresponding to one photoelectron of the MPPC. Second, we integrate ADC values for the waveform of the CV signal by a charged particle. The light yield is obtained from the integration of the waveform normalized by that of one photoelectron.

We integrate the ADC value of the one-photoelectron signal from the dark count noise. Fig. 6.2.1 shows an example of the waveform of the one-photoelectron signal. In Fig. 6.2.1, we first find the sample that has the maximum ADC value in the waveform. Around the point, we integrate the ADC values of 24 samples shown as the red region[4)]. The pedestal is subtracted from the ADC value of each sampling point in pulse by pulse, and the region in blue is used to set the pedestal[5)]. The distribution of the integrated ADC for one channel in one run is shown in Fig. 6.2.2. The peak corresponding to one-photoelectron signals is not found due to large noise in the KOTO experimental area. By introducing the special RMS cut explained in the following sentence, the peak of one-photoelectron signals is clearly observed. The RMS is defined as the fluctuation of the ADC value from the mean ADC value in the 24 samples. Figure 6.2.3 shows the distribution of the RMS for each set of the 24 samples[6)] where we clearly observe the one-photoelectron signal.

Next, the ADC values of 64 samples in the signal waveform are integrated as shown in Fig 6.2.4 (red region). Blue region is defined as a pedestal in this plot[7)]. Light yield is 42 p.e. in Fig 6.2.4.

The light yield is calculated for each channel. One CV strip has two channels corresponding to both ends of the WLS fibers. The light yield of the CV strip is calculated by adding the light yields of

[4)]We integrate from a hit time -6 samples to the hit time +18 samples. The hit time is the time where a value reaches the half maximum ADC value in the leading edge.

[5)]The pedestal is defined as mean ADC value of the 5 samples: first or last 5 samples whose RMS is smaller than that of other 5 samples. The mean ADC value in the right blue region is defined as the pedestal in this plot. This calculation method was used in the first physics run of the KOTO experiment.

[6)]In this figure, the first peak corresponds to pedestal, the second peak corresponds to one photoelectron, the third peak corresponds to two photoelectron. The peak corresponds to the pedestal is not equal to zero since we carry out peak search.

[7)]The mean ADC values of 8 consecutive samples are calculated in the range from the first to 64th samples. The minimum of the mean ADC values is selected as a pedestal.

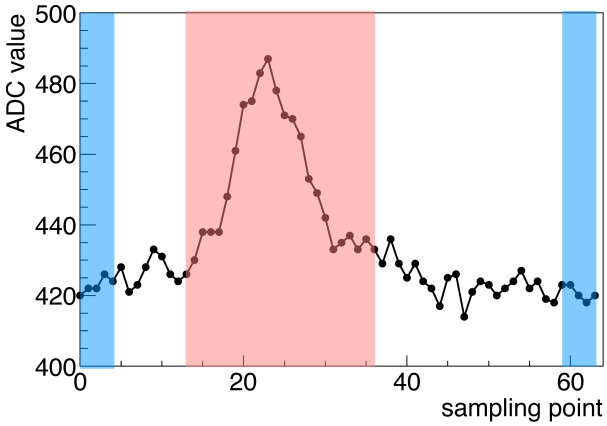

Figure 6.2.1: Waveform of the one photoelectron. Red region shows the integrated area of 24 samples. Blue region shows the region used for the calculation of pedestal.

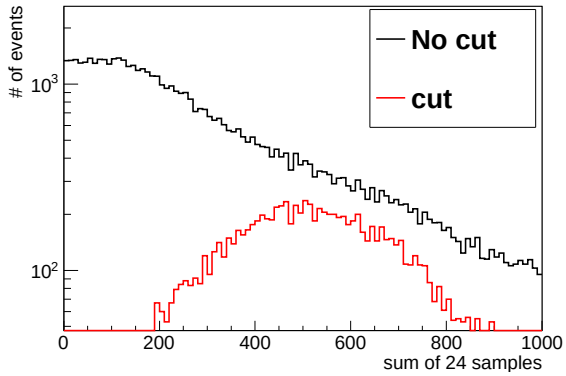

Figure 6.2.2: The distribution of the integrated ADC for one channel in one run. The black line shows the distribution with no cut. The red line shows the distribution with the RMS cut.

two channels[8)]. The distribution of the light yield in one strip is shown in Fig. 6.2.5. We calculate the peak in the distribution[9)] and normalize it by the energy deposit: in units of p.e./100 keV. The energy deposit by a charged particle penetrating the CV in a simulation is shown in Fig. 6.2.6. The peak value in Fig. 6.2.5 is 84 p.e., and the peak value in Fig. 6.2.6 is 470 KeV. The light yield is calculated to be 17.9 p.e./100 keV (=84/4.7) for one strip.

The position dependence of the light yield in the front CV and in the rear CV are shown in Fig. 6.2.7.

[8)] We correct the light yield of the strip by a path length in the strip. It is calculated from the trajectory of the reconstructed tracks. Incident angles of charged particles in this study are less than 20°, and thus the correction is a few % effect.

[9)] The distribution is fit with a convolution function of Landau and Gaussian, and the peak is defined as the most probable value of the Landau function. The Gaussian is used for taking account for the resolution of the detector. The sigma of the Gaussian is 14.5 p.e. in this figure.

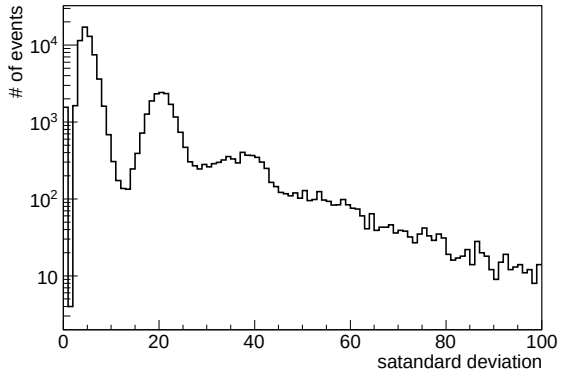

Figure 6.2.3: Distribution of the RMS for each set of the 24 samples.

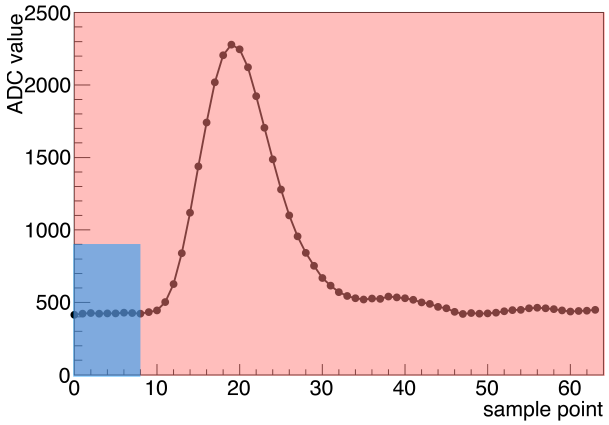

Figure 6.2.4: Waveform of the signal by a charged particle. Red region shows the integrated area. Blue region shows the region used for the calculation of the pedestal in this plot.

The white circle shows the fiducial region of the calorimeter in KOTO. The extrapolated position on the CV strips is separated into every 5-cm step along the fibers in the CV strip, and the light yield is calculated in each 5-cm step. The average light yield inside the fiducial region is 18.6 p.e./100 keV, and the minimum light yield is 12.1p.e./100 keV which satisfies the requirement. As introduced in Sec. 3.3.1, the photostatistics with the light yield of 18.6 p.e./100 keV has a negligible effect to the efficiency for charged particles from the Ke3 and Kπ3 BG, and we ensure the rejection power of the Ke3 and the Kπ3 BG. The average light yield is 14 % higher than that in the production thanks to the high photo detection efficiency by the higher applied voltage[10)]. We conclude that we construct the CV without any decrease of the light yield.

[10)]The expected difference of the light yield is 12 %.

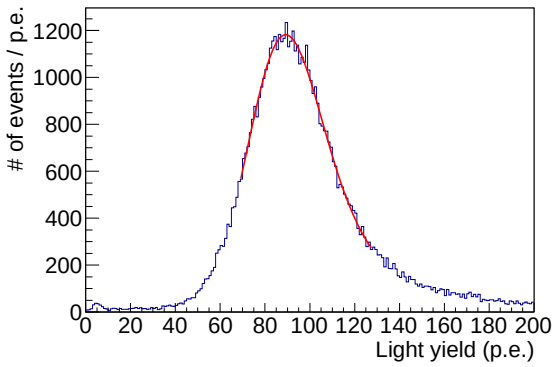

Figure 6.2.5: The distribution of the light yield in one strip. The histogram is the data, and the curve around the peak shows the fit corresponding to the convoluted function of Landau and Gaussian.

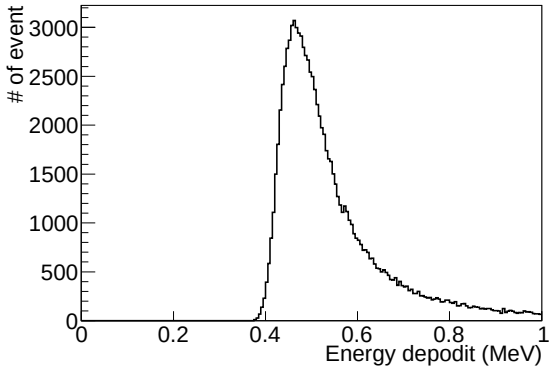

Figure 6.2.6: Energy deposit by a charged particle penetrating the CV in a simulation.

6.2.2 Timing Resolution

The waveform of the CV is sampled every 8 ns. Hit time of one channel is calculated as the time where a value reaches the half maximum ADC value in the leading edge (constant fraction method). The mean of hit timings at both ends is defined as a hit time, while the difference of the hit timings at both ends is used to evaluate the timing resolution in this analysis. The resolution of the mean time (σ_{Mean}) and that of the time difference ($\sigma_{\mathrm{Difference}}$) satisfy the equation:

$$\sigma_{\mathrm{Mean}} = \frac{\sigma_{\mathrm{Difference}}}{2} = \frac{\sqrt{\sigma^2_{\mathrm{Short}} + \sigma^2_{\mathrm{Long}}}}{2}, \tag{6.1}$$

where σ_{Short}, and σ_{Long} show the root-mean-square of the distributions of the hit times at both ends (short and long sides as defined in Fig. 4.1.3), respectively. The time difference of one strip is shown in

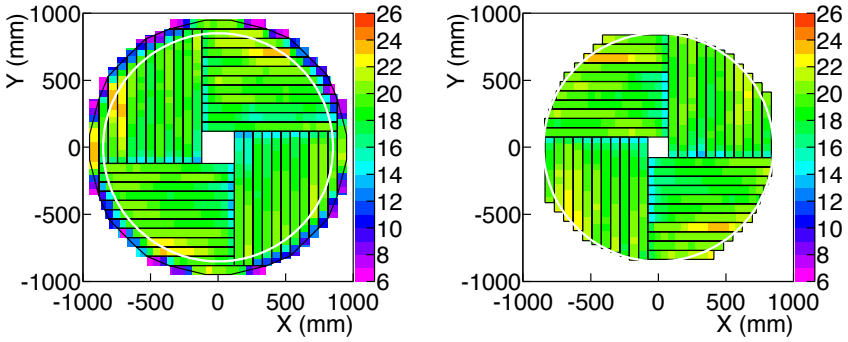

Figure 6.2.7: Position dependence of the light yield in the front CV (left) and in the rear CV (right). Z axis indicates the light yield in units of p.e./100 keV. The white circle shows the fiducial region of the calorimeter in KOTO. Smaller yields are observed at the both ends of the strip where the fibers are not embedded as described in Sec. 4.3.2 (The outer ends of the strips in the rear CV do not have these regions of reduced light yield and thus no decreases are observed.). The light yield at the outer region tends to be higher than that at the inner region since the length of the WLS fibers for the inner strips is $\sim$ 2 m long while the one for the outer strips is $\sim$1 m. Higher light yield in some outer strips comes from fluctuations in the scintillator thickness.

Fig. 6.2.8. The $\sigma_{\mathrm{Difference}}$ is calculated as the sigma of this distribution. For the strip shown in Fig. 6.2.8, $\sigma_{\mathrm{Difference}}$ is 2.5 ns and the timing resolution is 1.25 ns[11)].

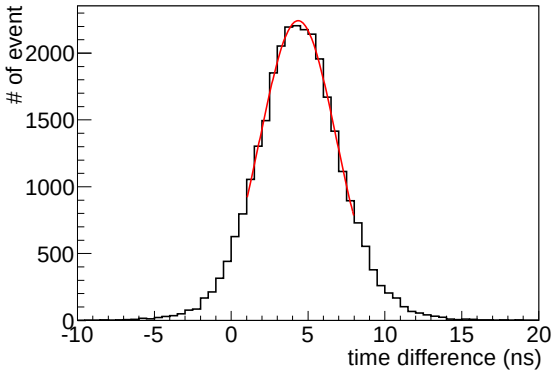

Figure 6.2.8: The time difference of one strip. The curve around the peak shows the fit with the Gaussian.

The position dependence of the timing resolution in the front CV and in the rear CV are shown in Fig. 6.2.9. The envelop of the fiducial region is shown in the white circle. The timing resolution is better than 3 ns in the entire region, and the average is 1.2 ns. The timing resolution is worse in the region where the light yield is smaller. This is due to the fact that a smaller light yield causes a larger

[11)]The time difference depends on the hit position since the propagation times to both ends change; the resolution here includes this contribution. The contribution to σ_{Mean} in the case of a 5 cm region is estimated to be 0.1 ns and is disregarded in this study.

time jitter of the signal pulse.

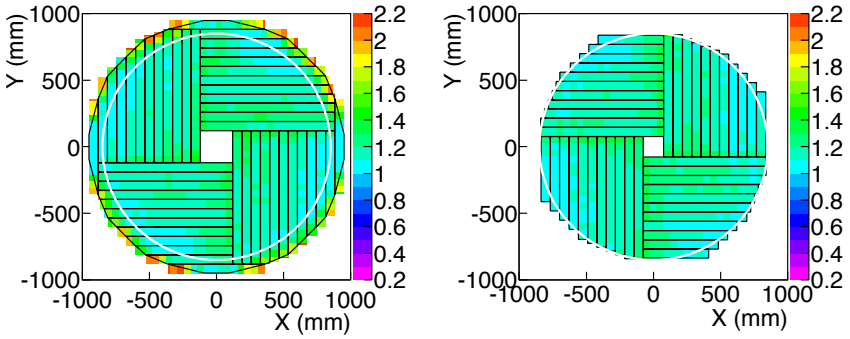

Figure 6.2.9: Position dependence of the timing resolution in the front CV (left) and in the rear CV(right). The z axis shows the timing resolution. The envelop of the fiducial region is shown in the white circle.

We evaluate the effect of the timing resolution to the accidental loss as explained in Sec. 3.3.2 with the dependence of the light yield. The distribution of the light yield as shown in Fig. 6.2.5 is separated into every 10 p.e. interval, and the timing resolution is calculated in each 10-p.e. interval. The timing resolution as a function of the light yield is shown in Fig. 6.2.10. Black points show the timing resolution in the fiducial region. In Fig. 6.2.10, the timing resolution becomes worse than 3 ns when the light yield is less than 20 p.e.. Red line shows a function of the timing resolution[12)], and we apply the function in the simulation. The accidental loss is estimated to be 4.9 % with the function, while the loss with 1.2-ns timing resolution is 2.7 %. The accidental loss with the function becomes larger than the ideal condition. The loss of 4.9 % is acceptable in KOTO[13)].

6.3 Energy calibration

We carry out the energy calibration of the CV, the hodoscope, and the calorimeter for the inefficiency analysis.

6.3.1 CV

Energy deposit of the CV strip (E_{strip}) is calculated from the following equation.

$$E_{strip} = L_{strip} \times \frac{E^{CV}_{peak}}{L_{peak}} \tag{6.2}$$

[12)] The distribution is fit by p0 $\times \sqrt{x}$ + p1.

[13)] As described in Sec. 3.3.2, we set the requirement of the accidental loss to be less than the level of 5 %.

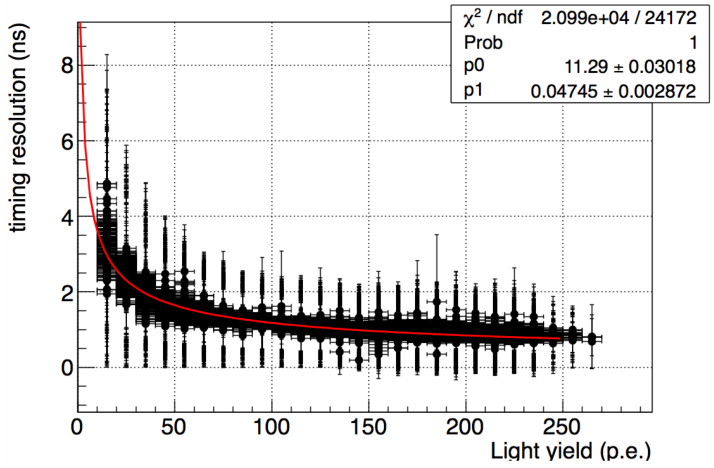

Figure 6.2.10: The timing resolution as a function of the light yield. Each point has the horizontal bar of ± 5 p.e. for the 10-p.e. interval, and has the vertical bar showing the error of the timing resolution. Red line shows a function of the timing resolution.

Here, L_{strip} is the light yield of the CV strip calculated in event by event. E^{CV}_{peak} is the peak value of the energy deposit in the simulation as shown in Fig. 6.2.6. L_{peak} is the peak value of the light-yield distribution in the data. In the calculation of L_{peak}, we use all data points with one strip[14]. In the calculation of E_{strip}, drift of the peak value of the light yield in time, especially temperature dependence, is evaluated. [15]. We measure the light yield of the peak value every 3 hours and convert to the energy deposit (MIP peak). The drift of the MIP peak in the data is shown in Fig. 6.3.1. The fluctuation of the MIP peak is 2.7 % in RMS and it is negligible for the inefficiency measurement.

6.3.2 Hodoscope

We convert the integrated ADC of the hodoscope to the energy deposit in the simulation. An integrated ADC distribution is shown in Fig. 6.3.2 left. The peak value is 7300 ADC count in this figure. Figure. 6.3.2 right shows the energy spectrum of the hodoscope in the simulation. The peak value is 1.7 MeV in this figure. The calibration constant of this module is 0.00023 MeV/ADC count(=1.7/7300).

[14] We do not consider the position dependence of the L_{peak} as shown in Fig. 6.2.7 since we can't resolve the hit position in KOTO and reproduce the same situation in this measurement.

[15] The control system for the readout system as described in Sec. 5.3. is not installed since the development of the control system is not completed. We use temperature monitors and other voltage control system to tune the MPPC gain.

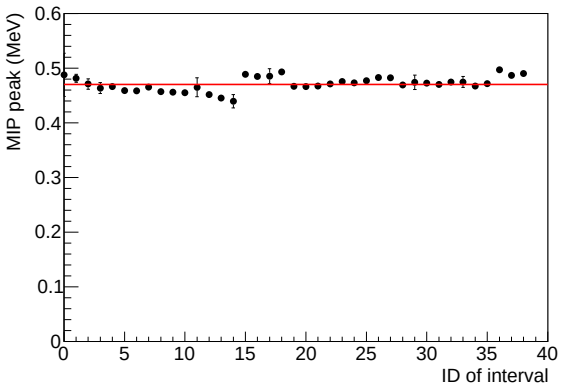

Figure 6.3.1: Drift of the peak value of energy deposit in the data. Red line shows 0.47 MeV.

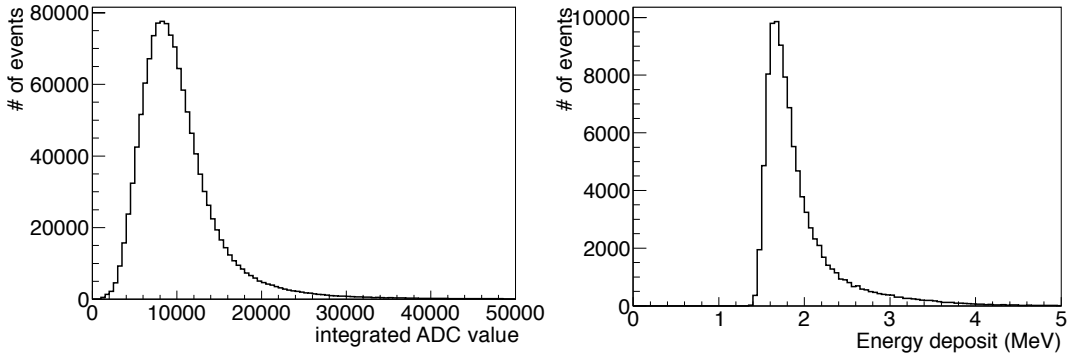

Figure 6.3.2: An integrated ADC distribution of the hodoscope (left). Energy spectrum of the hodoscope in a simulation (right).

6.3.3 Calorimeter

We convert the integrated ADC of the calorimeter to the energy deposit in the simulation. We use a peak of the integrated ADC value by cosmic ray muons. The distribution of the integrated ADC value in a small crystal of the calorimeter is shown in Fig. 6.3.3 [29]. The peak value is 1444 ADC count. We use 14 MeV for the small crystal and 28.15 MeV for the large crystal as the peak energy of the energy deposit by cosmic muons. The calibration constant in Fig. 6.3.3 is 0.0097 MeV / ADC count (=14/1444).

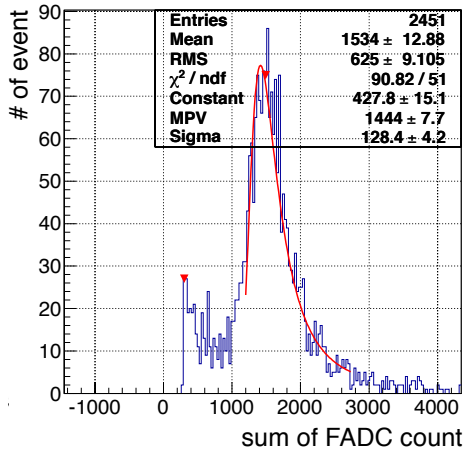

Figure 6.3.3: Distribution of the integrated ADC value in a small crystal of the calorimeter[29].

6.4 Simulation

In the inefficiency analysis, the tracks not penetrating the CV become fake inefficient events and are removed by introducing additional cuts. To check the validity of these cuts and to estimate the fake inefficient events, we carry out simulations. We first simulate the trajectory of charged particles. Second, we correct the detector response of the CV, the drift chambers, and the hodoscope[16]. Third, we consider the effects of electrical noise and accidental hits in the detectors.

6.4.1 Trajectory of charged particles

We study three main decay modes: $K_L \to \pi^{\pm}e^{\mp}\nu$, $K_L \to \pi^{\pm}\mu^{\mp}\nu$, and $K_L \to \pi^{+}\pi^{-}\pi^{0}$. Since it is not practical to simulate all the trajectories including non interesting one, we perform the simulation with three steps: the simulation with the chamber, the simulation with the CV, the hodoscope and the calorimeter, and the simulation of the electromagnetic shower in the calorimeter.

In the first step of the simulation, the K_L are shot from z = -1000 mm with momentum spectrum as shown in Fig. 6.4.1. The total number of the K_L is 1.2×10^{10}. We put only three chambers to reconstruct the tracks. All particles are stopped on the downstream surface of the third chamber. With requiring more than two hits in the first chamber, the events with no kaon decays before the first chamber are rejected.

In the second step of the simulation, we add the CV, the hodoscope, and the calorimeter. All the particles are shot from the third chamber and stopped the upstream surface of the calorimeter.

[16] For the calorimeter, no correction is applied since the calorimeter generates no systematic source.

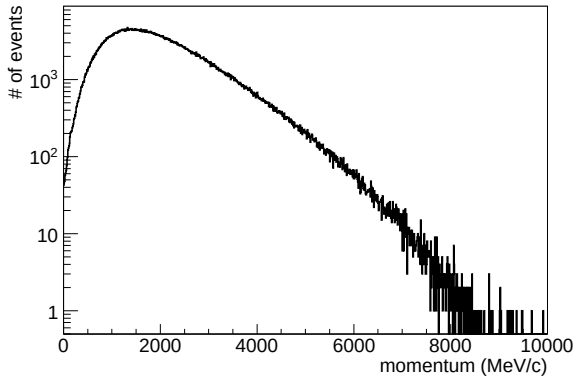

Figure 6.4.1: The momentum spectrum of the K_L used in the simulation.

Events which are not triggered on the hodoscope are removed by requiring more than two hits on the hodoscope.

In the third step of the simulation, all the particles are shot to the calorimeter, and the electromagnetic shower in the calorimeter is simulated.

6.4.2 Correction of detector response

We first describe the correction method of hit positions in the chambers. Next, we describe the correction methods of energy spectrum for the CV, and the hodoscope.

Hit position in the chambers

We reproduce hits of the chambers by smearing the hit position with the resolution effect studied in the reference [29]. Figure 6.4.2 shows the resolution of the chambers. The position resolution of the chambers is ~0.3 mm in the figure.

Energy spectrum of the CV

We adjust the light yield in the simulation to match with the data. The energy deposit is converted to the number of photons with the light yields shown in Fig. 6.2.7, and then smeared according to the Poisson distribution. Second, we recalculate the energy deposit as described in Sec. 6.3.1.

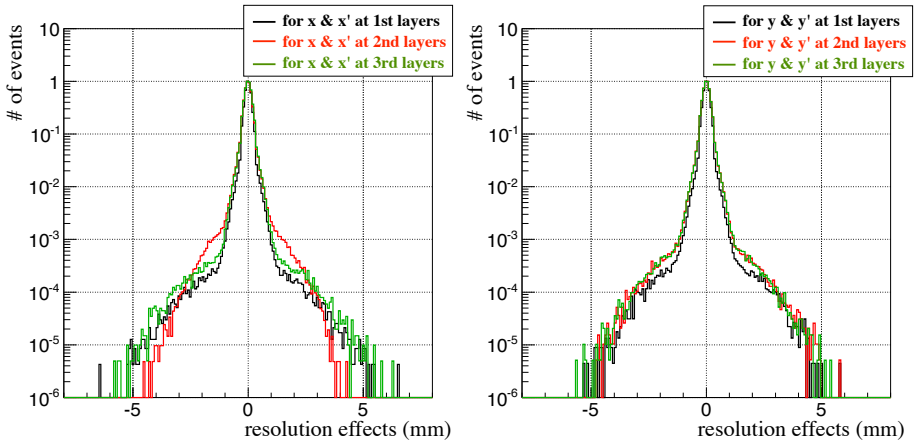

Figure 6.4.2: The resolution of the chambers studied in [29].

Energy spectrum of the hodoscope

The energy spectrum is corrected with position dependence of a PMT output and the energy resolution obtained from the data. The details of these methods are described in App. C.1.

6.4.3 Correction of electrical noise and accidental hits

We take clock trigger runs to check detector activities uncorrelated with the event trigger. The activities are caused by the accidental hits stemming from the beam or electrical noise in detectors. Figure 6.4.3 shows the energy spectrum of the CV (left), that of the hodoscope (middle), and that of the calorimeter (right) with the clock trigger runs. Most events in each detector have no activity except for the electrical noise, and some events have an activity stemming from the beam. We add the accidental activity to the energy deposit in the simulation.

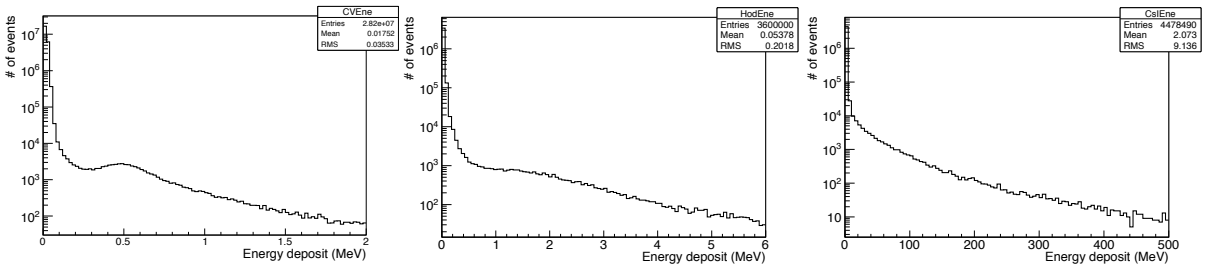

Figure 6.4.3: Energy spectrum with all the clock trigger runs. The left is that in the CV, the middle is the hodoscope, and the right is calorimeter.

6.5 Study of the inefficiency

We apply the event topology selection to ensure that the tracks of the charged particles are correctly reconstructed. Then, we check the energy deposit in the CV. We apply the track selection to ensure that the charged particles penetrate the CV. We describe the result of the inefficiency measurement. We study corrections of the fake inefficient events by using the simulation.

6.5.1 Event topology selection

We determine a correct pair of two tracks with tighter selection. We collect pairs of two tracks where one track goes into the CsI active region ("near track") and the other into the opposite side ("far track"). We select the correct pair of two tracks by requiring two conditions.

- Each extrapolated position on the hodoscope matches with the hodoscope module whose energy deposit is greater than 0.8 MeV[17)].
- The CV strips pointed by the far-track have an energy deposit of greater than 100 keV.

We select events where only one pair of two tracks satisfies the conditions. Only the near tracks are used to measure the inefficiency.

6.5.2 CV hit decision

We examine the energy deposit of the CV strips pointed by the near track. The actual hit position of a charged particle deviates from the pointed strips by the resolution of the extrapolated position on the CV. To cover the deviation, we examine 2 to 5 strips[18)]. We then take the maximum energy deposit among these strips as the CV energy deposit. The near track with the energy deposit in the front or rear CV less than 100 keV is categorized as the inefficient track.

6.5.3 Track selection

We remove events of which a charged particle does not hit the examined strips by introducing the variables of ΔR and CVR explained below. The "non-penetrating" events occur when a charged particles decays in flight or scatters in the materials between the chambers and the CV. The ΔR is a

[17)] We allow ±2.5 cm uncertainty of the extrapolated position on the hodoscope.

[18)] We collect strips which have an overlap with a virtual square surrounding the extrapolated position on the CV. The size of the square is14 cm ×14 cm, and it is enough to cover the deviation. The number of the examined strips is depending on the hit position.

distance between the clustered position and the extrapolated position on the calorimeter. The CVR is a distance between the extrapolated position on the CV and the center position of the CV in the xy plane. Each cut value is determined so that its systematic uncertainty for the inefficiency is negligible.

The ΔR distributions of the near tracks in the data and in the simulation are shown in Fig. 6.5.1 (a)[19]. The ΔR cut is set to be less than 30 mm. Thirty percent of the near tracks are removed by this cut. The data and simulation agree within 18% in the ratio between the data and the simulation as shown in the bottom of Fig. 6.5.1 (a). In the simulation, the non-penetrating tracks are shown by green line in the plot. The portion of the non-penetrating tracks becomes larger with the larger ΔR. The ΔR distribution for the inefficient tracks in the data and in the simulation are shown in Fig. 6.5.1 (b). The data and simulation agree within the statistical uncertainty in the data-MC ratio as shown in the bottom of Fig. 6.5.1 (b). The 98.5% of the inefficient events are removed by this cut. The portion of the non-penetrating tracks becomes $\sim$ 100 % when the ΔR becomes larger than 70 mm[20]. Some non-penetrating tracks survive the cut in the simulation. It occurs when the photon(s) from a π^0 hits near the extrapolated position on the calorimeter in the $K_L \to \pi^+\pi^-\pi^0$ decay. It also occurs when a charged particle scatters by producing Bremsstrahlung photon(s). The contribution of those residual non-penetrating track is corrected in the analysis of the inefficiency.

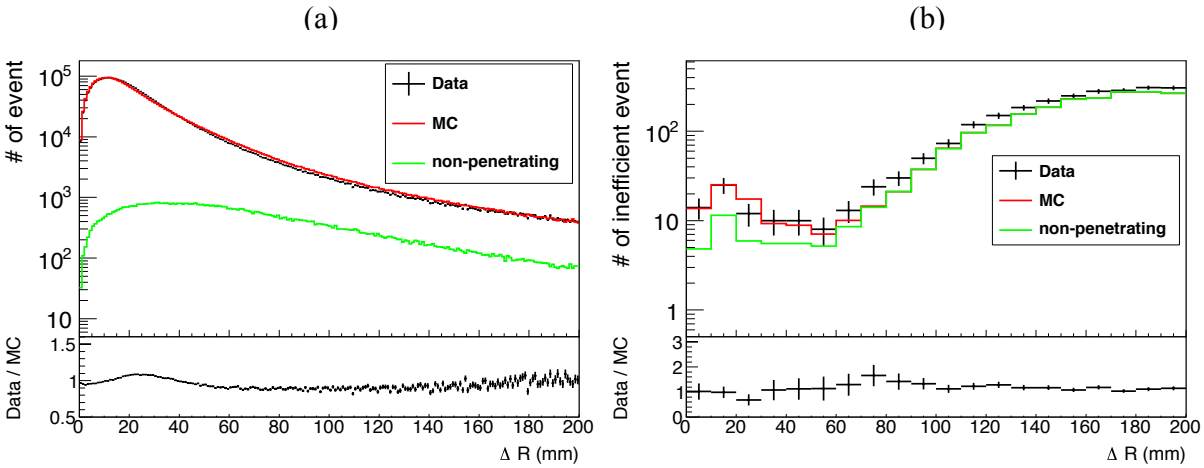

Figure 6.5.1: (a) ΔR distribution for the near tracks. (b) ΔR for the inefficient tracks. All the distributions of the simulations in (a) and (b) are normalized with the number of events of the data in (a).

The CVR distribution with the near tracks in the data and in the simulation are shown in Fig. 6.5.2 left. The CVR cut is set to be more than 200 mm. Ten percent of the near tracks are removed by this cut.

[19] Only events with single cluster is selected since the ΔR should be determined uniquely. Energy threshold for the cluster is 200 MeV.

[20] There are no hit in the examined strips when the actual hit position of a charged particle deviate more than 70 mm in the vertical direction to the fibers of the CV strip.

The data and simulation agree within 11% in the data-MC ratio as shown in the bottom of Fig. 6.5.1 left. Green line shows the non-penetrating tracks in the simulation. The CVR distribution for the inefficient tracks in the data and in the simulation are shown in Fig. 6.5.2 right. The 96.4% of the inefficient events are removed by this cut. The portion of the non-penetrating tracks becomes larger with the CVR cut smaller than 170 mm as shown in Fig. 6.5.2 right[21)].

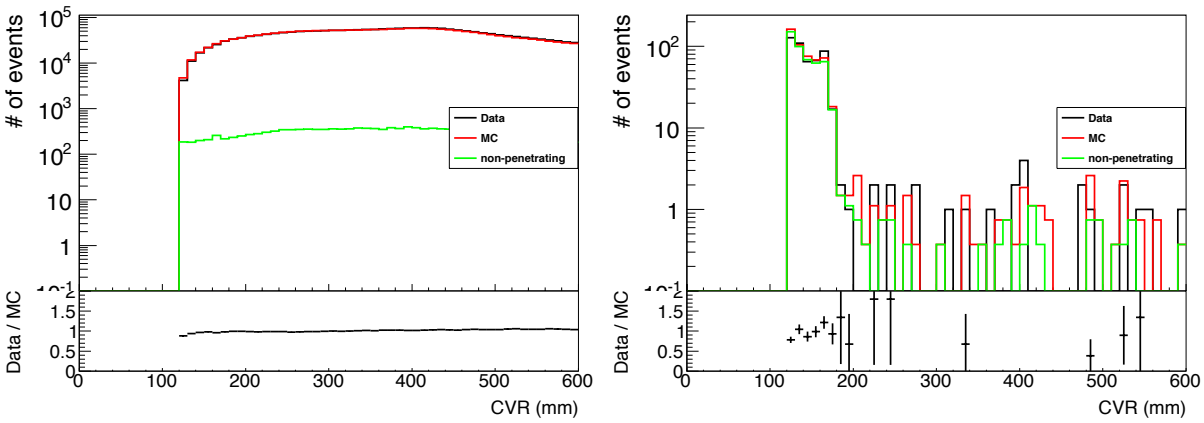

Figure 6.5.2: CVR distribution for the near track (left). CVR for the inefficient tracks (right). Definition of normalization are in the same way as Fig. 6.5.1.

Sixty six percent of total events remain with the ΔR cut and the CVR cut, while 98.8% of the inefficient events are removed. Most of the removed inefficient events are the fake inefficient events found in the simulation.

6.5.4 Result of the inefficiency measurement

The distribution of the extrapolated position on the front CV with all the cuts is shown in Fig. 6.5.3 left. The one on the rear CV is shown in Fig. 6.5.3 right. The fiducial region around the beam hole is determined by the CVR cut. The other limit of the fiducial region is determined by the fiducial region of the calorimeter. We investigate the inefficient events in the CV fiducial region. We first calculate the raw inefficiency. Then, we correct the fake efficient/inefficient events in the raw inefficiency. We also investigate the hit position of the inefficient tracks on the CV. Finally, we set the upper limit of the inefficiency since the statistics of inefficient events are not large.

The energy distribution in the front CV for the data and the simulation are shown in Fig. 6.5.4 left. The agreement between data and the simulation is good[22)]. The CV inefficiency is defined as the ratio

[21)]Intuitively, it is understood as half of the size of the maximum length of the beam hole (diagonal direction~170 mm).

[22)]Since we select the maximum energy deposit of the strips, the inefficient events has small energy deposit due to accidental activity. Small discrepancy in the region around 300 keV are due to the reproducibility of the response in the region where

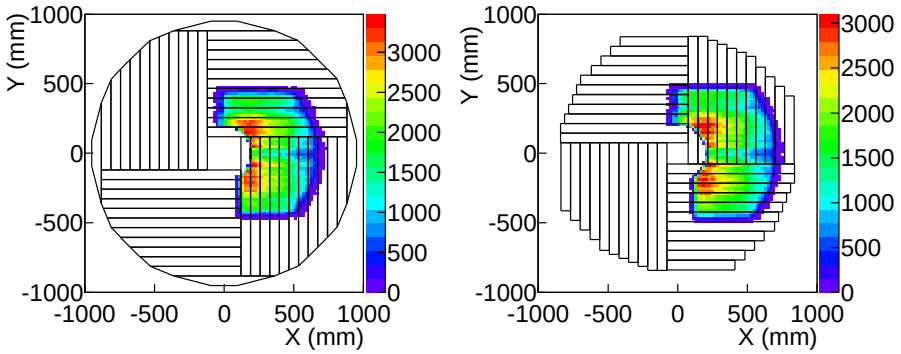

Figure 6.5.3: Distribution of the extrapolated position on the front CV (left). Distribution of the extrapolated position on the rear CV (right). The black line shows the envelop of the CV strips.

of the inefficient tracks to the near tracks. Table 6.5.1 shows the summary of the numbers of the near tracks and inefficient tracks. In the data, the inefficiency (I_{raw}) is $(1.13 \pm 0.24) \times 10^{-5}$ for the front CV, and $(1.43 \pm 0.26) \times 10^{-5}$ for the rear CV. The errors indicate statistical uncertainties. In the simulation, the estimated inefficiency is $(1.36 \pm 0.16) \times 10^{-5}$ for the front CV, and $(1.64 \pm 0.18) \times 10^{-5}$ for the rear CV. The inefficiency of data and MC agree well within the statistical uncertainty. Each CV layer achieves the required inefficiency of less than 10^{-3}.

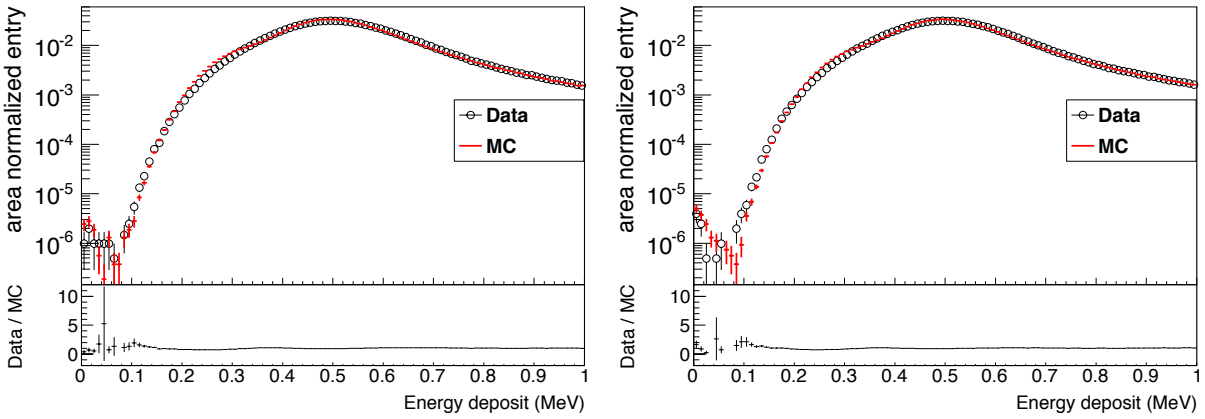

Figure 6.5.4: The energy distribution in the front CV (left). That in the rear CV (right). The spectra are normalized to the area over a full energy range.

Since there are the contamination of the fake "inefficient" events and the fake "efficient" events, we

the WLS fibers are embedded. In addition, the discrepancy at the region lower than 150 keV is due to the reproducibility in the boundary of the scintillator.

Table 6.5.1: Summary of the number of the near tracks and inefficient tracks

source of inefficient track	inefficient track	near track
Front CV (data)	23	2.0×10^6
Front CV (MC)	73	5.4×10^6
Rear CV (data)	29	2.0×10^6
Rear CV (MC)	88	5.4×10^6

correct the $I_{\rm raw}$ by using the following equation.

$$I_{\rm corr} = I_{\rm raw} \times (1 - C_{\rm n.p}) \times (\frac{1}{1 - C_{\rm acc}}). \tag{6.3}$$

$C_{\rm n.p}$ is estimated in the simulation as the ratio of non-penetrating tracks to all the tracks in the inefficient events. Among 73 (88) inefficient tracks in the front (rear) CV with $\Delta R < 30$ mm, there are 27 (42) non-penetrating tracks. $C_{\rm n.p}$ is $0.37^{+0.19}_{-0.18}$(=27/73) for the front CV, and $0.48^{+0.21}_{-0.19}$ (=42/88) for the rear CV. The errors indicate systematic uncertainties.

$C_{\rm acc}$ is defined as the ratio of the events with the energy deposit of the CV by the accidental activity greater than 100 keV to the events with the energy deposit greater than 100 keV. Hit multiplicity[23] of the front CV and rear CV among the examined strips in the data (black line) and in the simulation (red line) are shown in Fig 6.5.5. The average multiplicity is ~ 0.05, and it is the effect of the accidental activities. We estimate the accidental loss with the simulation to include the effect of the correlated activities due to a delta ray from a charged particle and/or a backsplash from the calorimeter. $C_{\rm acc}$ is 0.031 ± 0.006 for the front CV, and 0.043 ± 0.006 for the rear CV[24]. The errors indicate systematic uncertainties.

The corrected inefficiency is $(0.74 \pm 0.15^{+0.21}_{-0.22}) \times 10^{-5}$ for the front CV, and $(0.77 \pm 0.14^{+0.28}_{-0.31}) \times 10^{-5}$ for the rear CV. The first errors are statistical and the second errors are systematic. The source of the systematic errors are dominated by $C_{\rm n.p}$. The systematic errors are described in Sec. 6.6.

The inefficient points on the front CV and the rear CV are shown in Fig. 6.5.6. The crosses show the inefficient points. The squares on the edges of the strips indicate the position of the cutouts of the scintillators[25]. The majority of the inefficient points are found near the cutouts or on the edges of the scintillator strips, and not in the central region[26]. This is what we expected. We confirm that the CV is built as designed.

We set the upper limit of the inefficiency after all the corrections are applied. Assuming Poisson statistics, the upper limit is 1.32×10^{-5}(90% C. L.) for the front CV, and 1.46×10^{-5}(90% C. L.) for

[23] The definition of the multiplicity is the number of strips which have an energy deposit more than 100 keV.

[24] $C_{\rm acc}$ is smaller than the hit multiplicity since we eliminate events where the δ ray is generated and hits other strips in the

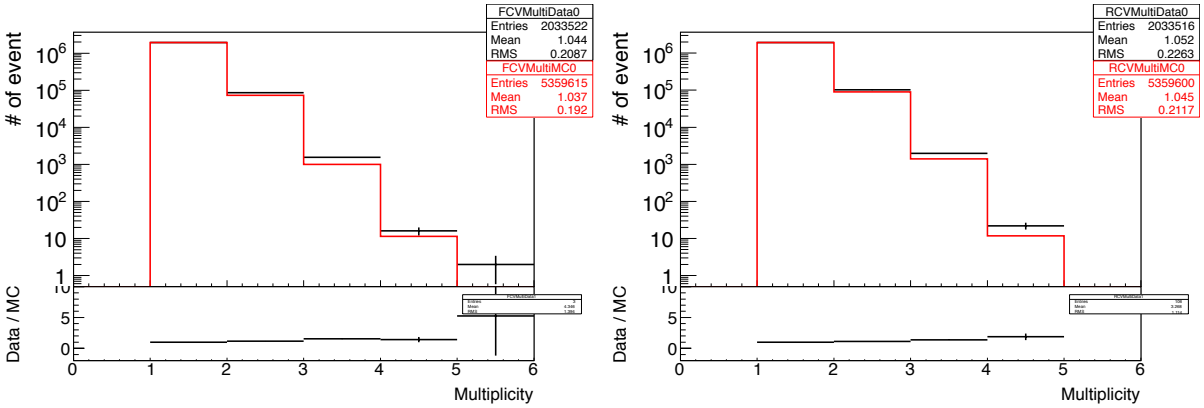

Figure 6.5.5: A multiplicity among the examined strips in the front CV (left) and the rear CV (right).

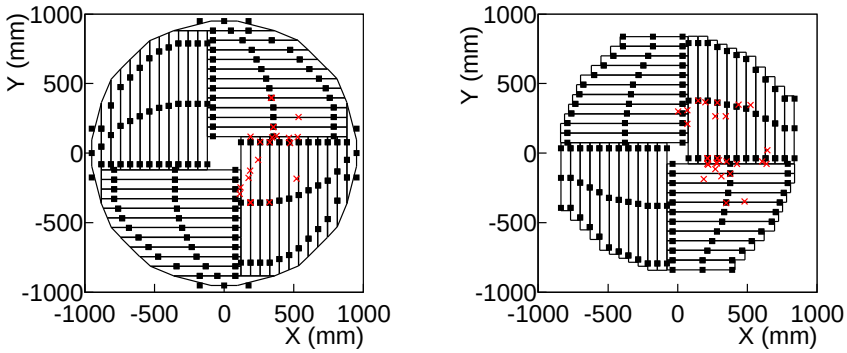

Figure 6.5.6: The inefficient points on the front CV (left). The inefficient points on the rear CV (right). The crosses show the extrapolated positions. The squares on the edges of the strips indicate the position of the cutouts expanded 50 times.

the rear CV. We conclude that the CV achieves high efficiency($< 1.5\times10^{-5}$ of inefficiency) and satisfies the requirement for KOTO.

same layer of the CV.

[25)] They are used to hold the scintillator strips in place. The size of the cutouts is magnified 50 times in these plots.

[26)] From the simulation, because we check the strips in the 14 cm ×14 cm virtual box and width of the strip is 7 cm, the hit position corresponding to the non-penetrating tracks also locates the edges of the scintillator strips.

6.6 Estimation of the systematic uncertainty for the inefficiency

We estimate the uncertainties for $C_{n.p}$ and C_{acc} by using the simulations. Other sources, (i.e. stability of energy deposit) are estimated from the data.

6.6.1 $C_{\mathrm{n.p}}$

There are five sources of systematic error of $C_{\mathrm{n.p}}$: reproducibility of the simulation, cutout size, statistical uncertainty, CVR cut, and ΔR cut.

Reproducibility of the simulation

The number of inefficient events is different between the data and the simulation and it is taken into account as the error of $C_{\mathrm{n.p}}$. $C_{\mathrm{n.p}}$ is defined with the number of the penetrating events (N_{p}) and the non-penetrating events (N_{np}) as

$$C_{\mathrm{n.p}} = \frac{N_{\mathrm{np}}}{N_{\mathrm{p}} + N_{\mathrm{np}}}. \tag{6.4}$$

The uncertainty of $C_{\mathrm{n.p}}$ is hence calculated as below.

$$\Delta C_{\mathrm{n.p}} = (1 - C_{\mathrm{n.p}}) \times C_{\mathrm{n.p}} \times \sqrt{\Delta N_{\mathrm{p}}^2 + \Delta N_{\mathrm{np}}^2}. \tag{6.5}$$

Here, ΔN_{p} is assigned as the discrepancy of the penetrating tracks between data and simulation, and ΔN_{np} is the discrepancy of the non-penetrating tracks. To estimate ΔN_{p} and ΔN_{np}, we prepare two control samples: penetrating enriched sample and non-penetrating enriched sample.

The penetrating enriched sample is selected as the inefficient event in the front CV by requiring the activity in the rear CV[27)]. The non-penetrating enriched sample is selected as the inefficient event in the front CV by requiring no activity in the strip pointed by the near track[28)]. The ΔR distributions with the penetrating enriched samples and the non-penetrating enriched one are shown in Fig. 6.6.1. Black points show the data, red line shows the simulation, and green line shows the non-penetrating tracks in the simulation. Table. 6.6.1 shows the number of inefficient events in $\Delta R < 30$ mm. The difference between the data and the simulation is 4.1 ± 4.1 for the left plot, 1.8 ± 1.9 for the right plot. The data and simulation agree within the statistical uncertainty. We calculate conservatively the square root of the

[27)] We focus the region where the rear CV is segmented every 7 cm in x direction to enrich the penetrating tracks. The non-penetrating tracks are removed when the strip in this region is pointed by the track and has an activity. The non-penetrating track deviates from the trajectory of a charged particle in x direction since the hodoscope is not separated in x direction. The energy deposit in the front CV is checked in the same way as described in Sec. 6.5.2, and we collect inefficient tracks.

[28)] The track becomes the non-penetrating tracks when the strip pointed by the track has no activity in both the front CV and rear CV. We collect inefficient tracks by the front CV in the same way as the penetrating enriched sample.

sum between the first term and the second term as ΔN_{p} or ΔN_{np} since statistics is small for each sample. ΔN_{p} is 33 % and ΔN_{np} is 55 %. We assume that ΔN_{p} and ΔN_{np} are the same in $\Delta C_{\mathrm{n.p}}$ for the front CV and the rear CV, and calculate $\Delta C_{\mathrm{n.p}}$ by using $C_{\mathrm{n.p}}$ of each CV layer. The systematic uncertainty of $C_{\mathrm{n.p}}$ is ±41% for the front CV, ±33% for the rear CV.

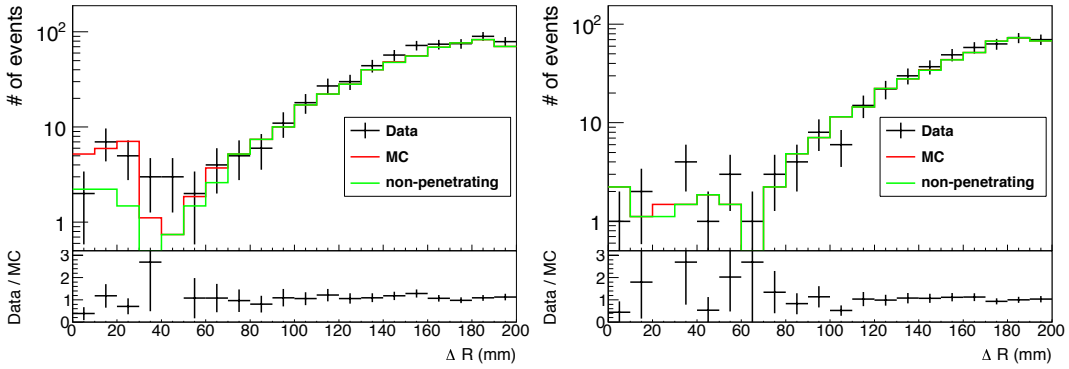

Figure 6.6.1: ΔR distributions with the penetrating enriched samples (left) and the non-penetrating enriched samples (right).

Table 6.6.1: The number of inefficient events. The values in the parentheses are the number of the non-penetrating tracks.

	nominal sample	penetrating enrich sample	non penetrating enrich sample
data	23	14	3
MC	27(10.7)	18.1(5.9)	4.8(4.4)

Cutout size in the simulation

The uncertainty of the cutout size of the scintillators affects the number of inefficient events. We estimated the uncertainty of $C_{\mathrm{n.p}}$ caused by the cutout size[29)]. The uncertainty is +24% and −19% for the front CV, +21% and −15% for the rear CV.

Statistical uncertainty

The statistical uncertainty in the simulation is taken into account as a source of the systematic error on $C_{\mathrm{n.p}}$. The uncertainty is ±22% for the front CV, ±19% for the rear CV.

[29)]The cutout size of 0.6 mm × 0.4 mm is varied within ±0.1 mm since it is machining accuracy.

CVR cut

$C_{\mathrm{n.p}}$ is affected by the systematic uncertainty of the CVR cut. The detail is described in App. C.2.1. The systematic uncertainty is 2.4% for the front CV, 0% for the rear CV (no changes are observed).

ΔR cut

$C_{\mathrm{n.p}}$ is affected by the systematic uncertainty of the ΔR cut. The detail is described in App. C.2.2. The systematic uncertainty is found to be negligible.

Summary of uncertainty for the $C_{\mathrm{n.p}}$

Table. 6.6.2 shows the list of systematic sources for $C_{\mathrm{n.p}}$. We define the square root of the sum for all systematic sources as the total systematic uncertainty.

Table 6.6.2: List of the systematic source at $C_{\mathrm{n.p}}$.

source	uncertainty (front CV)	uncertainty (rear CV)
reproducibility of the simulation	± 0.15	± 0.16
cutout size in the MC	$+0.088/-0.066$	$+0.098/-0.066$
statistical uncertainty of the MC	± 0.083	± 0.090
CVR cut	+0.0089	0
ΔR cut	0	0
total	+0.19/-0.18	+0.21/-0.19

6.6.2 C_{acc}

The C_{acc} is affected by the systematic uncertainty of the accidental activity. We check the difference of the multiplicity between the data and the simulation as shown in Fig. 6.5.5[30)]. The difference is assigned as the systematic uncertainty. The uncertainty for the C_{acc} is ± 0.006 for the front CV and ± 0.006 for the rear CV. These uncertainties are enough small and the contribution to the final value of the systematic uncertainty is negligible.

[30)] We first integrate the number of events whose multiplicity is more than 2. Second, we calculate the discrepancy of the multiplicity between the data and the simulation.

6.6.3 Other sources of the systematic uncertainty

We estimate the uncertainty of the raw inefficiency (I_{raw}) in the corrected inefficiency (I_{corr}). In the estimation, $C_{\mathrm{n.p}}$ and C_{acc} are fixed to the nominal values.

We first evaluate the systematic uncertainty of the energy threshold of the CV. This energy threshold affects the raw inefficiency. We monitor the drift of the energy peak in the CV as the source of the uncertainty of the energy threshold. We calculate the energy peak every 50000 events interval in the same way as described in Sec. 6.3.1 [31]. The drift is calculated as the following equation.

$$\mathrm{drift} = \frac{P_{\mathrm{each}} - P_{\mathrm{all}}}{P_{\mathrm{all}}} \tag{6.6}$$

Here, P_{each} is the energy peak in every 5000 events interval, and P_{all} is the energy peak calculated from all the data. Figure 6.6.2 left shows the drift of the energy peak as a function of the event interval corresponding to the time. Figure 6.6.2 right shows the distribution of the drift. From these figure, the RMS of the drift is ∼0.02 MeV. The energy threshold of the CV is varied from 0.098 MeV to 0.102 MeV with the RMS. The uncertainty is -0.042×10^{-5} for the front CV, and $(+0.058/-0.043) \times 10^{-5}$ for the rear CV.

We evaluate the systematic uncertainty caused by the energy threshold of the hodoscope, that of the calorimeter, the allowed region in the matching of the hodoscope, and misalignment of the hodoscope. Their systematic uncertainties are negligible. The systematic uncertainties by the raw inefficiency of the data are enough small and the contribution to the final value of the systematic uncertainty is ∼5%. We ignore all the systematics by the raw inefficiency.

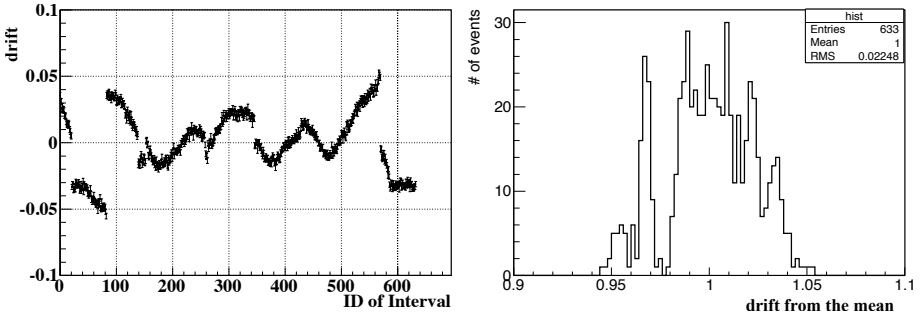

Figure 6.6.2: Drift of the energy peak as a function of the time (left). Distribution of the drift (right).

[31] We collect the energy deposit of the strip pointed by the near tracks without an identification of strips.

6.6.4 Summary of systematic uncertainty

The systematic uncertainty is dominated by the systematic uncertainty of the C_{np}. Other sources are negligible. The uncertainty for the corrected inefficiency is $(+0.21/-0.22) \times 10^{-5}$ for the front CV, and $(+0.28/-0.31) \times 10^{-5}$ for the rear CV.

Chapter 7

Discussion on $\mathrm{K_L} \to \pi^0\nu\bar{\nu}$ search with the background study

We discuss $K_L \to \pi^0\nu\bar{\nu}$ search by using the evaluated performance of the CV. We first discuss the neutron backgrounds in the first physics run of KOTO. Second, we discuss the rejection of K_L decay backgrounds including charged particles by using the results reported in Chap. 6. Third, we estimate the signals with the accidental loss by the CV and discuss the sensitivity of KOTO.

7.1 Neutron backgrounds

We compare the numbers of the neutron backgrounds between the first physics run of KOTO and the final result of E391a in the scatter plot for the identification of $K_L \to \pi^0\nu\bar{\nu}$. The $K_L \to \pi^0\nu\bar{\nu}$ signal is identified by the decay position of the π^0 reconstructed with the calorimeter and the transverse momentum of the π^0 as described in Sec. 2.1.2. The scatter plot of the decay position on the K_L beam versus the transverse momentum for E391a (left) [4] and KOTO (right) [42] are shown in Fig. 7.1.1. The black square in Fig. 7.1.1 left shows the signal region in E391a. Inner most black square in the right plot shows the signal region in the first physics run of KOTO. We achieve the single event sensitivity of 1.29×10^{-8} [42] with the signal region, while that of E391a is 1.11×10^{-8} [4].

In Fig. 7.1.1, there are several regions to classify the background sources. In E391a, 101 events are observed around Z = 550 cm and the number of the estimated neutron event is 77.2±5.6 [4], while no event is found in KOTO. We find the neutron events in the KOTO experiment is largely suppressed by at least two orders of magnitude with respect to the E391a experiment in the same level of the sensitivity. The suppression is considered to be due to improvement in two components: the KL beamline and the CV. As described in Sec. 2.2, we design the KL beamline to minimize the number of neutrons in beam halo, and the number of neutrons hitting the CV is reduced. As described in Sec. 3.2, we remove inner

modules of the E391a CV in the design of the KOTO CV, and the number of neutrons interacting with the CV is reduced. We confirm that KOTO achieves the sensitivity of 1×10^{-10} from the point of the neutron backgrounds.

In Fig. 7.1.1, no events are observed in the signal region of E391a, while one event is observed in KOTO. The number of expected background in the signal region of KOTO is estimated to be 0.36 ± 0.16 from the simulation [42], and the remaining event is estimated to be background. The main source of background is estimated to be an event where a single neutron interacts with the calorimeter and generates two clusters through several hadronic interactions in the calorimeter. We should reduce this background although the neutron backgrounds related to the CV is well suppressed. New cuts to remove hadronic clusters are being developed by using hit pattern of crystals in the cluster or waveforom information.

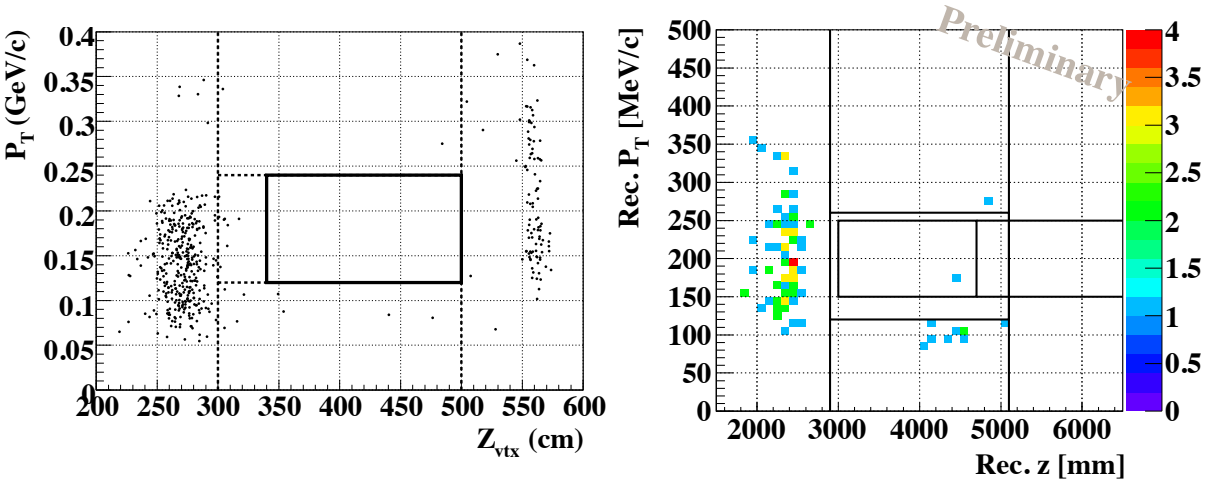

Figure 7.1.1: The scatter plot of the decay position of the reconstructed π^0 on the K_L beam versus the transverse momentum of the π^0 for the result of E391a (left) [4] and that for KOTO (right) [42]. Black square in the left plot shows the allowed region of the signal in E391a. Inner most black square in the right plot shows the signal region in the first physics run. Dotted lines in the left plot and other black lines in the right plot indicate boundaries to classify events for the background study.

7.2 K_L decay backgrounds including charged particles

There are three types of K_L decay backgrounds with charged particles as described in Sec 3.1.2: the Ke3 BG, the Kπ3 BG, and the penetrating BG. The rejection of the Ke3 BG and the Kπ3 BG is ensured by the high light yield of the CV as reported in Sec. 6.2.1, and the number of these backgrounds are well suppressed as shown in Table 2.2.1. The number of the penetrating BG is expected to be $O(10^{-11})$ from the achieved inefficiency of 1.5 $\times 10^{-5}$, and well suppressed. The inefficiency for a charged particle

from the penetrating BG is affected by high rate environment in KOTO, and the high rate effect is not taken into account in the estimation of the penetrating BG described in Sec. 3.3.1. First, we describe the mechanism of the rate effect. Second, we describe a method to reduce the rate effect that is used in the first physics run of KOTO. Third, we evaluate the inefficiency with the rate effect by using the data analyzed in Chap.6. Fourth, we apply the inefficiency to estimate the penetrating BG.

7.2.1 Masking effect

When the π^0 is reconstructed in the calorimeter, energy deposit in the CV is checked in a time span of several tens of ns. The hit time of the CV is calculated by the constant fraction method as explained in Sec. 6.2.2, and the time span is called veto window. When the hit time is mis-measured outside the veto window, a charged particle from the K_L is not vetoed by the CV. The source of the mis-measurement is the shift of the hit timing caused by a "masking effect" where a waveform of an accidental hit overlaps with that of a charged particle to be vetoed. An example of the waveform of the CV with the masking effect is shown in Fig. 7.2.1. The "true pulse" in the figure is a hit caused by a charged particle to be vetoed. The "accidental pulse" is a hit caused by a charged particle which accidentally hits the CV. The purple box shows the veto window of the CV, and the veto window is set to be within ± 15 ns from the hit time of the true pulse[1)]. The "summed pulse" is the observed pulse with the overlap of the accidental pulse. The "true pulse" is not vetoed since the hit time of the summed pulse is shifted to outside of the veto window. The inefficiency for a charged particle is increased by the masking effect. The probability of the masking effect increases as the beam intensity increases with more accidental hits. As a result, the inefficiency increases with the beam intensity.

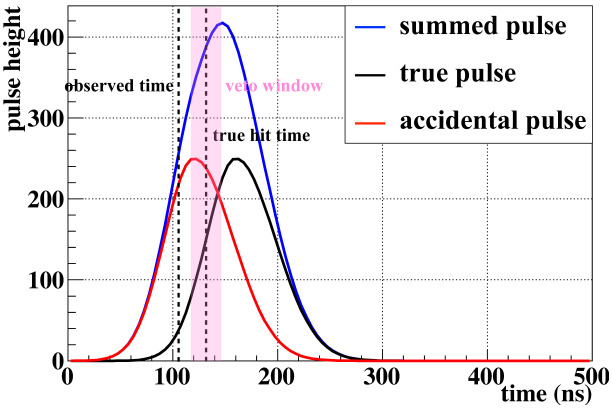

Figure 7.2.1: An example of the waveform of the CV in the masking event.

[1)]Since the mean of the hit time difference between the CV and the calorimeter is zero as shown in Fig. 3.3.6, the center of veto width is set to the hit time of the calorimeter. In this plot, the hit time difference is assumed to be zero.

An event topology with the masking effect occurring in both layers of the CV is shown in Fig. 7.2.2. The track of the “true pulse” penetrating both layers of the CV is shown. The true pulse is not vetoed since the accidental charged particle hits near the hit position of the “true pulse” on both layers of the CV. This phenomenon is called “correlated masking effect”. The number of the penetrating BG is increased by the correlated masking effect since the total inefficiency of the CV is not assumed with the fourth power of the single-layer inefficiency.

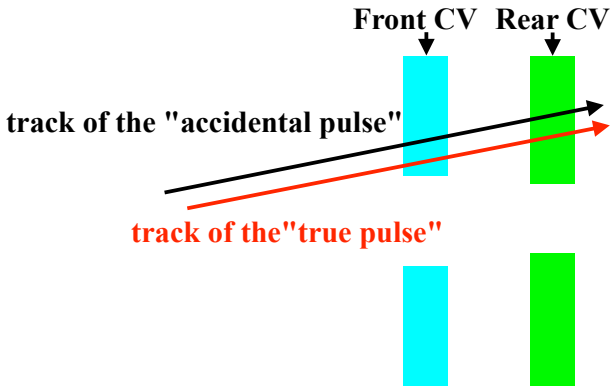

Figure 7.2.2: An event topology with masking effect occurring in both layers of the CV.

7.2.2 Parabola fitting method

The constant fraction method is used to calculate the hit timing in the waveform as described in Sec. 6.2.2, and a parabola fitting method is another method to calculate the hit timing. In the parabola fitting method, we collect consecutive three samples in the waveform where the second sample has the maximum ADC value among three. Next, we select two sets of the three samples with the highest and the second highest ADC values among possible sets. Each sample of two sets is fit by a parabola function individually, and the hit time is defined as the peak time of the parabola function. With two signals at both ends from one strip, there are four hit timings in one strip with the parabola fitting. The event is vetoed when one of the four hit timings locates within the veto window with energy deposit greater than 100 keV. The parabola fitting prevents the timing shift when two overlapped pulses are identified as separate peaks, while the timing shift occurs with the constant fraction method where the leading edge of the pulses are not separated. Even in an unseparated case for the parabola fitting, the shift in the hit time can be smaller compared to the constant fraction as in Fig. 7.2.1. In Fig. 7.2.1, the hit time shift with the parabola fitting is 12 ns, while that with the constant friction is 25 ns. The parabola fitting reduces the masking effect by resolving two overlapped pulses or by reducing the shift in the hit time of the unseparated overlapped pulses. The parabola fitting was used in the first physics run to reduce the masking effect.

We evaluate the timing resolution in the parabola fitting method in the same way as described in Sec. 6.2.2. The position dependence of the timing resolution in the parabola fitting for the front CV (left) and for the rear CV (right) are shown in Fig. 7.2.3. The mean of the timing resolution is 1.6 ns in the fiducial region. This resolution is worse than that in the constant fraction whose value is 1.2 ns. The parabola fitting reduces the masking effects, and worsens the timing resolution. We use the parabola fitting to estimate the masking effect since the timing resolution in the parabola fitting is better than the required value that is 3 ns as described in Sec. 3.3.2.

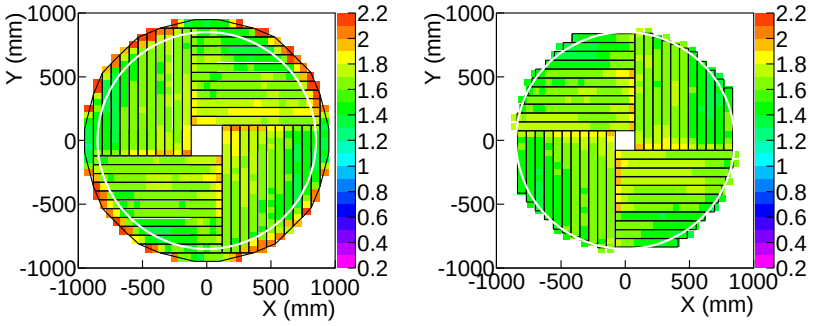

Figure 7.2.3: The position dependence of the timing resolution by using the parabola fitting in the front CV (left) and in the rear CV (right). White circle shows the fiducial region of the CV. Z axis indicates the timing resolution in units of ns.

7.2.3 Estimation of the inefficiency with the masking effect

We evaluate the inefficiency with the masking effect in the data. In the experiment for evaluation of the CV performance, the CsI timing information is not available, and we do not use the time difference between the hit time of the calorimeter and that of the CV as the veto window. We use the time difference between the hit of the CV by the near track and that by the far track. The near track and the far track are defined in Sec. 6.5.1, and are the pair of tracks where one goes to the active region of the calorimeter (near track) and other goes to the in-active region of the calorimeter (far track). The near track is used to evaluate the inefficiency, and the far track is used in the event selection.

We calculate the hit timings corresponding to two tracks by the following two methods. We first calculate the hit timing corresponding to the far track. We use the hits of two strips in the front and rear CV pointed by the far track. The hit time of the far track is defined as the mean time of the two strips with the time-of-flight (TOF) correction[2)]. We select events where the hit time difference between the

[2)]We calculate the TOF between the vertex position of two tracks and the extrapolated position on the front or rear CV with assuming the speed of the light. We correct the hit time difference between two strips by the difference of the TOF.

two strips is within ± 2.6 ns[3)] and the energy deposits of two strips are between 0.25 MeV and 0.7 MeV equivalent to single charged particle passing the strip.

We calculate the hit time by the near track. We examine the hit time of several strips extrapolated from the near track on the CV as described in Sec. 6.5.2. The CV hit time in the front or rear CV is defined as the hit time of the strip that has the closest time to the far track hit among the extrapolated strips with energy deposit greater than 100 keV. Figure 7.2.4 shows the time difference between the CV hit time and the far track with the TOF correction. We set the veto window around the peak of this distribution. We use the two sets of the veto width: 30 ns and 80 ns. The 30-ns width is the default value for the designed beam intensity of KOTO, while the 80-ns width was used in the first physics run. The RMS in Fig. 7.2.4 is 2.4 ns, and both veto width are long enough to achieve the measured inefficiency of 1.5×10^{-5} if there is not the long tail by the masking effect.

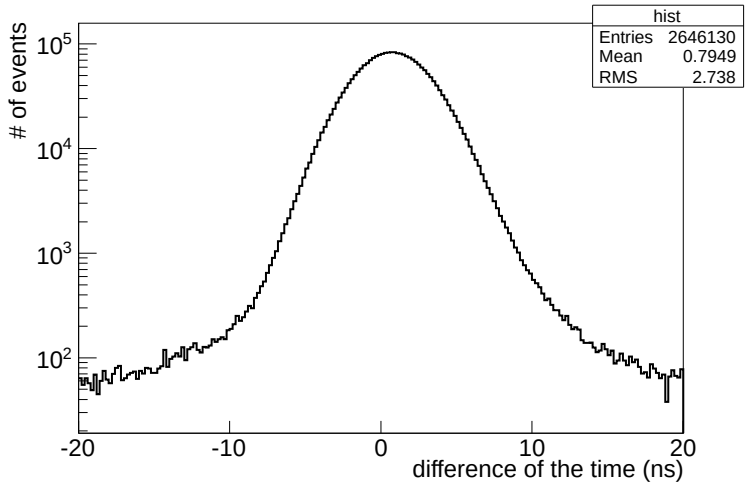

Figure 7.2.4: Time difference between the CV hit time and the far track with the TOF correction.

We estimate the inefficiency with the veto window cut. We examine the energy deposit of the strips corresponding to the CV hit time. Figure 7.2.5 shows the energy spectrum in the front CV (left) and in the rear CV (right). The red line shows the energy deposit with 30-ns veto window. The green line shows the energy deposit with 80-ns veto window. The black line shows the energy deposit without the veto window cut. The events with the energy deposit less than 100 keV are counted as the inefficiency. Table 7.2.1 shows the summary of the inefficiency[4)]. The inefficiency for the front and rear CV are shown. We find that these inefficiency with the timing cut is worse than that without timing cut by

[3)]It is equivalent to the RMS in the distribution of the time difference.

[4)]All the inefficiency with the veto window cut are twice of the real condition at most since they include the correlated masking effects in the far track. In the real condition, we use the time difference between the calorimeter and the CV, and the masking effect does not occur in the calorimeter as described in the reference [28].

the making effect[5)]. We also find that the inefficiency decreases by expanding the veto window. The inefficiency as a function of the veto width is shown in Fig. 7.2.6 for both the front and rear CV. The red line shows an exponential function. The inefficiency varies as the exponential function from the 30-ns veto window to 80-ns veto window since the probability of the event overlapping with an accidental pulse (overlapping probability) depends on an exponential function. The overlapping probability is calculated to be $5 \times 10^{-3} = 1 - exp(-50 \times 10^3 \times 100 \times 10^{-9})$ since the accidental rate of the examined strips is ~50 kHz and the width of the signal waveform is 100 ns. From Fig. 7.2.6, the probability of the masking effect (masking probability) is defined as the inefficiency at the veto width equal to zero, and calculated to be $(4 \pm 0.2) \times 10^{-3}$. The masking probability is same as the overlapping probability in this analysis.

We count the events where both layers of the CV are inefficient as the correlated inefficiency, and which is shown as "correlated" in Table 7.2.1. By the correlated masking effect as described in Sec. 7.2.1, the correlated inefficiency of 3.3×10^{-4} (or 3.4×10^{-6}) is worse than the multiplication of the inefficiency between the front and rear CV that is 1.7×10^{-6} (or 3.4×10^{-8}).

We use 10 times of the inefficiency shown in Table 7.2.1 for the background estimation with the designed beam intensity of KOTO since the accidental rate is ~ 2 MHz with the designed beam intensity, while it is ~ 200 KHz in this measurement.

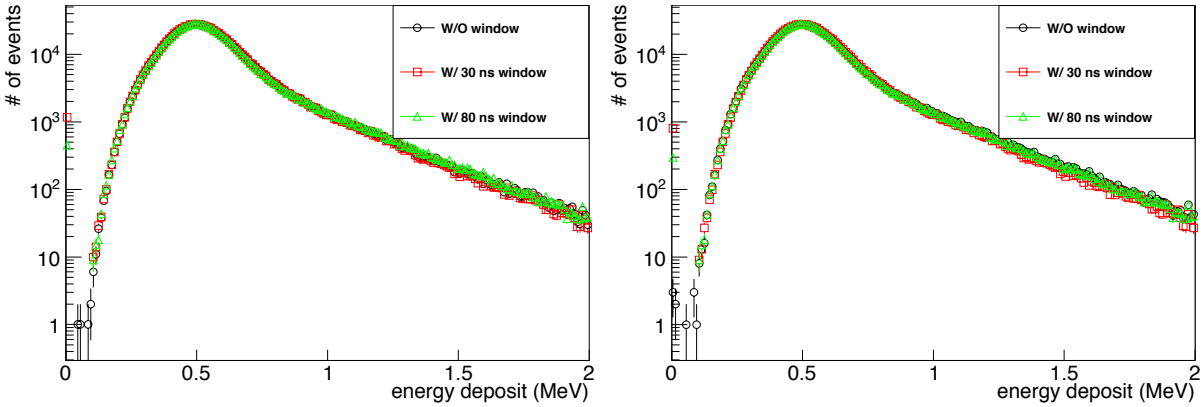

Figure 7.2.5: Energy spectrum of the front CV (left) and of the rear CV (right).

[5)]There are the contamination of the fake inefficiency in these inefficiency as described in Sec. 6.5.4. The fake inefficiency is order of 10^{-6} and much smaller than the inefficiency caused by the masking effect, we neglect the contamination of the fake inefficiency.

Table 7.2.1: summary of the inefficiency with the data analyzed in Chap. 6.

condition	without veto window	30 ns window	80 ns window
front CV	$0.57 \pm 0.26 \times 10^{-6}$	$1.4 \pm 0.04 \times 10^{-3}$	$2.1 \pm 0.2 \times 10^{-4}$
rear CV	$1.2 \pm 0.4 \times 10^{-5}$	$1.2 \pm 0.04 \times 10^{-3}$	$1.6 \pm 0.1 \times 10^{-4}$
correlated	non	$3.3 \pm 0.2 \times 10^{-4}$	$3.4 \pm 0.2 \times 10^{-6}$

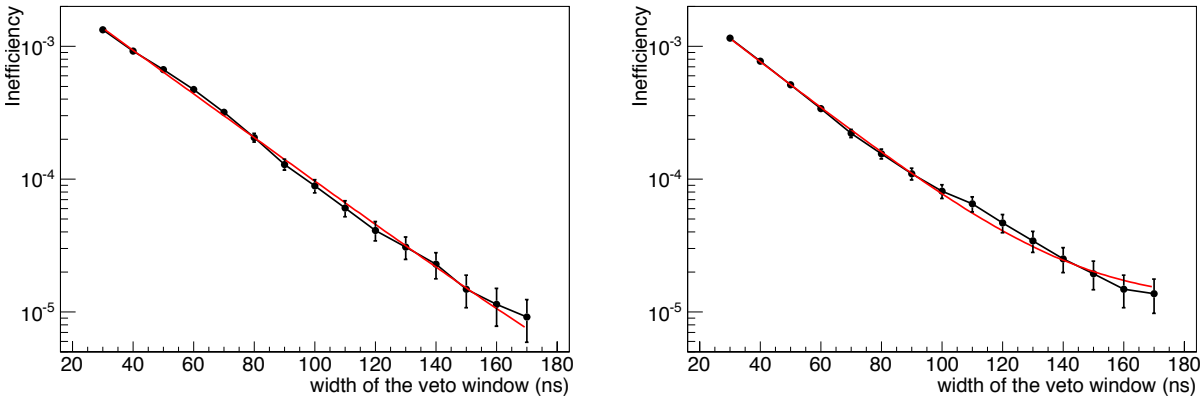

Figure 7.2.6: The inefficiency as a function of the veto width in the front CV (left) and in the rear CV (right). The red line shows an exponential function.

7.2.4 Estimation of penetrating BG

We carry out more precise background simulation to estimate the number of the penetrating BG. Since it is not practical to carry out full simulation with $\sim 5 \times 10^{12}$ K_L decays that we expect to collect in KOTO. We perform the simulation with 2 steps: collection of events where two charged particles hit the CV, and simulation of the electromagnetic shower in the calorimeter.

The $K_L \to \pi^{\pm} e^{\mp} \nu$ decay is generated from z=-1000 mm. We put the CV and the Neutron Color Counter (NCC)[6]. We collect events where two charged particles hit the CV with no activities in NCC. The charged particles are stopped on the surface of the front or rear CV. When the charged particle hits the front CV, the number of hits in the CV layers is calculated by extrapolating the trajectory of a charged particle from the front CV to the rear CV.

Two charged particles are shot to the calorimeter. We put the calorimeter, the Color Counter 03 (CC03), the Color Counter 04 (CC04), and the Outer Edge Veto (OEV)[7]. The CV is removed in this

[6] The NCC is shown in Fig. 2.1.1 and Table.2.1.1. The NCC limits the acceptance of the CV for charged particles from the K_L which decays upstream of it. The energy threshold of NCC is 2 MeV.

[7] They are shown in Fig. 2.1.1 and Table.2.1.1. They reject events where the shower leak from the calorimeter occurs. The energy threshold of the CC03 is 3 MeV, that of the CC04 is 3 MeV, and that of the OEV is 2 MeV.

simulation since evaluated values are used as the CV inefficiency. Clusters are formed and the π^0 is reconstructed in the calorimeter. We apply the hit pattern cut described in App. A, and examine events in the signal region as described in Sec 3.3.1.

We estimate the number of the penetrating BG with the inefficiency estimated in Sec. 7.2.3. The number of hits on the CV without applying the inefficiency of the CV is shown in Fig. 7.2.7. We find that there are three types of events: two-hit events, three-hit events, and four-hit events. Two-hit event occurs when two charged particles hit only the rear CV[8)]. Three-hit event occurs when one charged particle hits both layers of the CV and other charged particle hits only the rear CV. Four-hit event occurs when both charged particles hit both layers of the CV. We find that the four-hit events dominate. These events are weighted with the evaluated inefficiency of the single layer (W_s) without considering the correlated masking effect.

$$expected\ backgrounds = (N_4 \times W_s^4 + N_3 \times W_s^3 + N_2 \times W_s^2) \times R_{DS}. \tag{7.1}$$

Here, N_4 is the number of the four-hit events, N_3 is that of the three-hit events, and N_2 is that of the two-hit events. R_{DS} is the normalization factor between the number of K_L in the designed statistics and that of K_L in this simulation. The correlated masking effect in the inefficiency should be taken into account for the estimation of the penetrating BG. N_4 and N_3 are weighted by using the inefficiency with the correlated masking event (W_c). The number of background is in the following equation.

$$expected\ backgrounds = (N_4 \times W_c^2 + N_3 \times W_c \times W_s + N_2 \times W_s^2) \times R_{DS}. \tag{7.2}$$

The value of W_s is 1.2×10^{-2} with the 30-ns veto window, and 1.6×10^{-3} with the 80-ns veto window. The value of W_c is 3.3×10^{-3} with the 30-ns veto window, and 3.4×10^{-5} with the 80-ns veto window. W_s and W_c are 10 times of the values shown in Table 7.2.1 as mentioned in Sec. 7.2.3. The number of the penetrating BG is estimated to be $(5.3 \pm 0.6) \times 10^3$ with the 30-ns veto window, and 0.64±0.07 with the 80-ns veto window. The errors indicate the statistical uncertainty. The penetrating BG is found to be main source of the background by charged particles from the K_L decay since the number of the Kπ3 BG is estimated to be 0.11 and that of the Ke3 BG is estimated to be 0.07 as shown in Table 2.2.1.

7.3 Signals with the accidental loss of the CV

7.3.1 Estimation of the signals

We estimate the number of signals in consideration of the accidental loss by the CV. The number of signals (N_{sig}) is calculated with the following equation.

$$N_{sig} = N_K \times Br(K_L \to \pi^0 \nu\bar{\nu}) \times A_{KOTO} \tag{7.3}$$

[8)]The beam hole of the front CV is wider than that of the rear CV to reduce the interaction between the CV and neutrons.

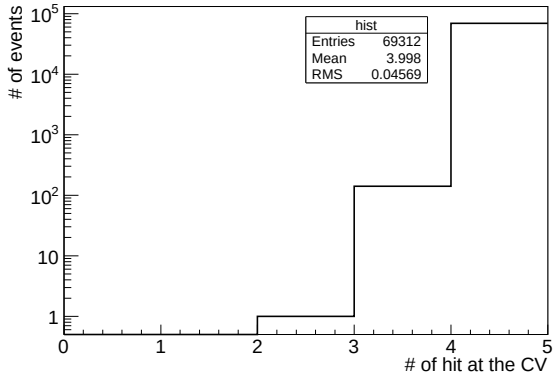

Figure 7.2.7: The number of hits on the CV without applying the inefficiency of the CV.

Here, N_K is the number of K_L in the designed statistics, Br($K_L \to \pi^0\nu\bar{\nu}$) is assumed to be 3.0×10^{-11}, and A_{KOTO} is an acceptance of KOTO for the $K_L \to \pi^0\nu\bar{\nu}$ decay. A_{KOTO} is the product of four components: the decay probability, the geometrical acceptance, the cut efficiency, and the acceptance loss. The decay probability is the fraction of events where K_L decays in the KOTO detector. The geometrical acceptance is the fraction of events where 2 photons from $K_L \to \pi^0\nu\bar{\nu}$ hit the calorimeter. The cut efficiency is the fraction of events where the reconstructed π^0 is satisfied with all the criteria described in Sec. 2.1.2 and App. A. The acceptance loss is the fraction of events which are removed by veto process. There are two kinds of the acceptance loss: the loss by the accidental hit (accidental loss), and the loss by the backsplash from the calorimeter (backsplash loss).

We carry out a simulation to estimate the decay probability, the geometrical acceptance, and the cut efficiency[9)]. The value of A_{KOTO} and the number of expected K_L are shown in Table 7.3.1. The acceptance loss is calculated as follows. The acceptance loss is studied in the reference [24], and the value is 50% where the accidental loss of the CV is estimated to be negligible. The acceptance loss in this study is the sum between the acceptance loss in the reference and the estimated accidental loss as described in Sec. 3.3.2. The accidental loss of the CV is expected to be 6 % for 30-ns veto window, and 15 % for 80-ns. The number of signals is expected to be 3.2 ± 0.3 with 30-ns veto window, and 2.6 ± 0.3 with 80-ns. The errors indicate the uncertainty from the branching ratio of $K_L \to \pi^0\nu\bar{\nu}$.

[9)] We perform the simulation with two steps. First, we put all the detectors and shot the $K_L \to \pi^0\nu\bar{\nu}$ decay 10^6 times at z = -1000 mm. Particles are stopped on the surface of the calorimeter. The decay probability and the geometrical acceptance are calculated from the trajectory of $K_L \to \pi^0\nu\bar{\nu}$. Second, all the particles are shot to the calorimeter. All the cuts are applied, and the cut efficiency is calculated.

Table 7.3.1: The value of A_{KOTO} and the number of expected K_L.

	value
Number of K_L	1.746×10^{14} [28]
Decay probability of K_L	3.7%
Geometrical acceptance	29%
Cut efficiency	13%
Acceptance loss with 30-ns veto window	56 %
Acceptance loss with 80-ns veto window	65 %

7.3.2 Discussion on the number of signals and backgrounds

The number of signals and that of the penetrating BG are shown in Table 7.3.2. The number of backgrounds is much larger than that of the signals with 30-ns veto window, and KOTO can not achieve the sensitivity of $K_L \to \pi^0\nu\bar{\nu}$ predicted in the SM. With 80-ns veto window, the number of backgrounds is 4 times smaller than that of the signals, and the accidental loss with 80-ns veto window is found to be acceptable in KOTO. We confirm that KOTO achieves the sensitivity of $K_L \to \pi^0\nu\bar{\nu}$ predicted in the SM from the point of backgrounds by the K_L decay including charged particles. On the other hand, to achieve more sensitivity, it is better to reduce the accidental loss of the CV.

Table 7.3.2: The number of signals and that of penetrating BG.

	30 ns window	80 ns window
$K_L \to \pi^0\nu\bar{\nu}$	3.2 ± 0.3	2.6 ± 0.3
penetrating BG	$(5.3 \pm 0.6) \times 10^3$	0.64±0.07
S/N	6×10^{-4}	4.1

7.3.3 Discussion on future improvements

We should reduce the accidental loss of the CV by narrowing the veto window to increase the sensitivity. The inefficiency can be reduced by eliminating the masking effect with new two methods of pulse-identification. These methods will be applied to the CV in the future.

Remove a pulse shaper and install a high-frequent sampling ADC The output of the CV is currently shaped to a Gaussian-like pulse in the ADC. The rise time of the pulse is $\sim$ 15 ns at the MPPC output, and becomes $\sim$ 30 ns in the ADC. The masking effect can be reduced by removing the shaper[10)].

[10)]The output waveform becomes narrower and the probability occurring the masking effect is decreased.

A 500 MHz sampling ADC is the candidate to record a narrow waveform without the shaper.

Template fitting We resolve overlapped pulses with the masking effect into two pulses by using a template of the overlapped pulses with the masking effect. The template pulses with various energy deposit should be prepared.

Chapter 8

Conclusion

Search for new physics beyond the Standard Model (SM) is a key to access new CP-violating process which explains the imbalance between matter and antimatter in our universe. The $K_L \to \pi^0 \nu\bar{\nu}$ decay is one of the powerful tools for new physics search since some new physics models predict a larger branching ratio than that in the SM and $K_L \to \pi^0 \nu\bar{\nu}$ is strongly suppressed in the SM (branching ratio is $O(10^{-11})$).

The KOTO experiment is a dedicated experiment to observe the $K_L \to \pi^0 \nu\bar{\nu}$ decay for the first time. We upgrade the detector from KEK-PS E391a which is the pilot experiment for KOTO. The signature of $K_L \to \pi^0 \nu\bar{\nu}$ is two photons from a π^0 decay with no other particles detected. For the identification of the final state, the energy and position of two photons are measured by an electromagnetic CsI calorimeter. To ensure that there are no particles except for a π^0, charged and neutral particle detectors are installed as veto counters. Since the K_L decay with charged particles occurs approximately 3×10^{10} times more frequently than the signal, we develop the Charged Veto detector (CV) to achieve high detection efficiency for the charged particles. The K_L beam contains a large number of neutrons, and neutrons in the beam halo produce a serious background by interacting with the CV. The CV is designed to remove the K_L decays with charged particles and to reduce the neutron interactions.

The CV has two separated layers of plastic scintillators. The thickness of the scintillator is 3 mm, where amount of the materials is minimized in order to reduce neutron interaction. To reject the background from the K_L decays including charged particles with thin scintillators, small inefficiency, high light yield, and good timing resolution are essential, and we estimate the requirements by using MC simulations. The CV is required to have less than 10^{-3} inefficiency including geometrical acceptance for charged particles penetrating the CV. The CV is required to have more than 10 p.e./100 keV light yield to keep high efficiency. The CV is required to have better than 3 ns timing resolution to keep the loss of the signal at 5% level.

The CV consists of $\sim$ 50 scintillator strips, and we design the CV strip to minimize the loss of geometrical acceptance without increasing the thickness of the scintillators, and to maximize the light yield with thin scintillators. Wavelength shifting (WLS) fibers are embedded in the scintillators, and the both-end readout by WLS fibers is adopted. We develop the components, and we decide to use BC404 for the scintillator, Y11 (350) for fibers, and MPPC for readout. We develop the connection method between fibers and MPPC with the light loss less than 10 %. We produce the CV strips, and measure their light yield. The light yield on average is 16.3 p.e./100 keV, and satisfies the requirement of the light yield with thin scintillators. After the measurement, we construct the CV, and the CV is installed in the KOTO experimental area for its performance test.

We develop the readout system for the CV. The readout system consists of three components: the MPPC, the preamplifier, and the 125 MHz ADC. We develop the MPPC integrated with the Peltier cooler to stabilize its gain and photon detection efficiency, and to reduce the dark count noise. We also develop the preamplifier to record one-photoelectron signal of the MPPC by the 125 MHz ADC. We develop the control system for the readout system to control applied voltage and the temperature of the MPPCs individually. After the installation of the CV, we operate the MPPCs and the preamplifiers by using the control system in the engineering run and the first physics run of KOTO. The MPPCs are kept to be 10$\pm$0.01 °C over the whole experiments, and the readout system and its control system work well. The drift of the outputs of the CV is less than 2 % and the dark count noise rates are less than 500 kHz. We confirm that the gain and photon detection efficiency of the MPPC are stable and the dark count noise rate is acceptable in the experiments.

We evaluate the performance of the constructed CV to the three requirements in the special experimental setup. We measure the light yield, the timing resolution, and the inefficiency for charged particles penetrating the CV by using the drift chambers. The light yield per 100 keV energy deposit is measured to be 18.6 p.e. on average, and the timing resolution of the scintillator strips is 1.2 ns. To measure the inefficiency of the CV at the level of $O(10^{-5})$, the charged tracks from K_L decays are carefully chosen by the drift-chambers and the fine-segmented CsI electromagnetic calorimeter. The inefficiency per layer is less than 1.5×10^{-5}. The CV achieves high efficiency, high light yield, and good timing resolution with thin scintillators, and satisfies all the requirements in the KOTO experiment.

We discuss the sensitivity of $K_L \to \pi^0 \nu\bar{\nu}$ search by using the evaluated performance of the CV. We compare the numbers of the neutron backgrounds between the first physics run of KOTO and the final result of E391a. There are no background events in KOTO, and the number of neutron events is found to be 1/100 smaller than that in E391a at least. We confirm that the KOTO experiment achieves the sensitivity of 1×10^{-10} from the point of the neutron backgrounds. For the K_L decays with charged particles, we estimate the number of penetrating BG with the designed beam intensity to take into account a high rate effect. The penetrating BG is found to be a main source of backgrounds from the K_L

decay with charged particles, and the number of the penetrating BG is estimated to be 0.64 ± 0.07 with the 80-ns veto window. We also estimate the number of signals with the accidental loss of the signal by the CV. The accidental loss is 15%, and the number of signals is expected to be 2.6 ± 0.3. The number of backgrounds from the K_L decay with charged particles is 4 times smaller than that of the signals, and it is found to be acceptable in the KOTO experiment.

Through this thesis, we succeed in the development of the high efficiency charged particle detector with low material and its operation. For the application in the KOTO experiment, we confirm that the CV achieves its requirements and the number of backgrounds from the K_L decay with charged particles is suppressed enough to achieve the sensitivity of $K_L \to \pi^0 \nu\bar{\nu}$ in the SM.

Appendix A

Event selection in KOTO

We introduce the event selection for the reconstructed π^0 in the calorimeter.

E-total cut

The energies of two photons should be greater than 0.65 GeV to avoid the effect of the online energy threshold of 0.5 GeV in the calorimeter.

Center of energy cut

The center of energy should be more than 200 mm to avoid the effect of the online threshold of 165 mm for the center of energy.

Vertex time cut

The vertex time is a hit time of a photon on the calorimeter corrected by the TOF. We first calculate the TOF between the decay position of the reconstructed π^0 and the hit position of a photon on the calorimeter. The TOF is subtracted from the hit time of the photon on the calorimeter. We set the requirement of the vertex time difference to be less than 2 ns. Figure A.0.1 shows the difference of the vertex time between two photons form the π^0 in $K_L \to \pi^0\nu\bar{\nu}$ with the E-total cut and the COE cut in a simulation. The RMS in Fig. A.0.1 is 0.1 ns, and is small enough to the cut value of 2 ns.

Extra cluster veto

The event is rejected when there are extra clusters whose hit time on the calorimeter is closer than 10 ns to the vertex time.

E_γ cut

The energy of two photons are required to be between 100 MeV and less than 2000 MeV to qualify the two photons from the π^0 in $K_L \to \pi^0\nu\bar{\nu}$. Energy of a photon from the π^0 in $K_L \to \pi^0\nu\bar{\nu}$

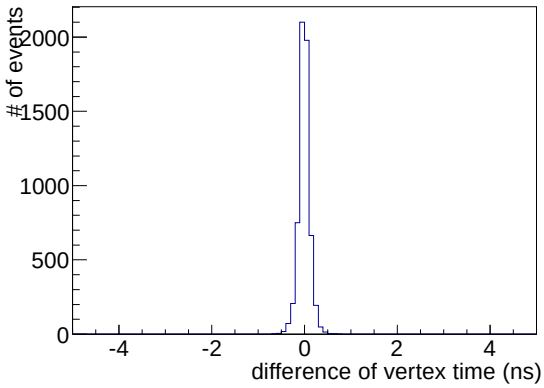

Figure A.0.1: The difference of the vertex time between two photons form the π^0 in $K_L \to \pi^0\nu\bar{\nu}$ with the E-total cut and the COE cut in a simulation.

is shown in Fig. A.0.2. The cut value of the E_γ cut is suitable to qualify the photon from π^0 in $K_L \to \pi^0\nu\bar{\nu}$.

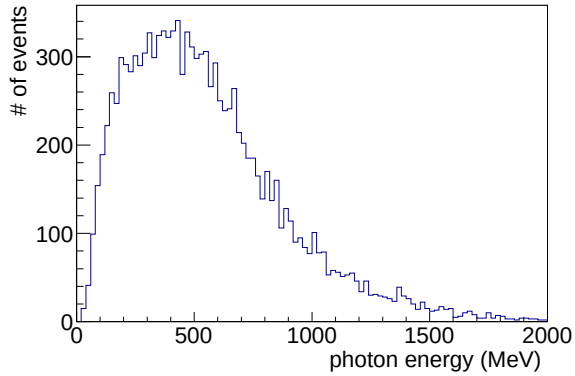

Figure A.0.2: Energy of a photon from π^0 in $K_L \to \pi^0\nu\bar{\nu}$ with the E-total cut and the COE cut in a simulation.

E-θ cut

E-θ is a multiplication between the energy and the polar angle of a photon, and E-θ of a photon from the π^0 in $K_L \to \pi^0\nu\bar{\nu}$ is shown in Fig. A.0.3. The mean of E-θ is 6000 MeV· degree, and E-θ of both photons are required to be more than 2500 MeV· degree in order to reject two photons which are decayed from $K_L \to \pi^0\pi^0$ [31].

γ distance cut

The distance between two photons on the calorimeter should be more than 300 mm. It is to remove events where the shower leak of one cluster affects the energy and the position recon-

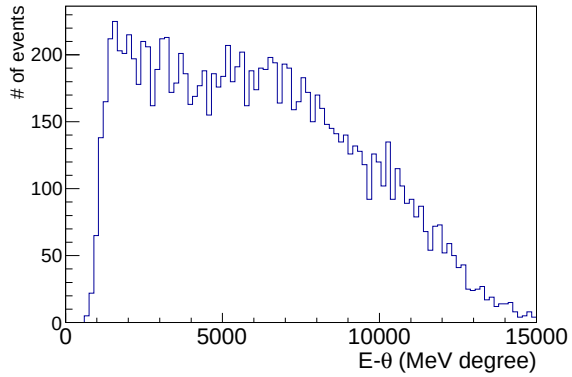

Figure A.0.3: E-θ of a photon from the π^0 in $K_L \to \pi^0\nu\bar{\nu}$ with the E-total cut and the COE cut in a simulation.

struction of other cluster. The distance between two photons from the π^0 in $K_L \to \pi^0\nu\bar{\nu}$ is shown in Fig. A.0.4. The mean of the two-photon distance is 660 mm, and the γ distance cut is set so that the signal loss by the γ distance cut is less than 3%.

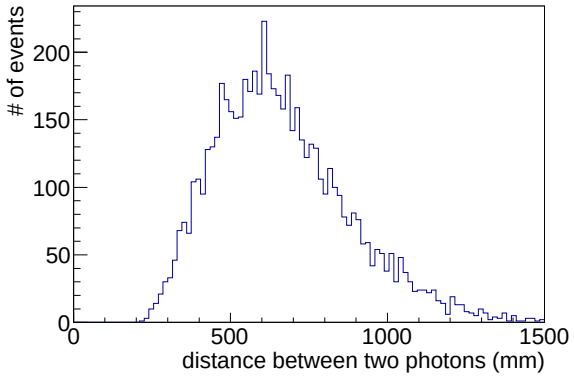

Figure A.0.4: The distance between two photons from the π^0 in $K_L \to \pi^0\nu\bar{\nu}$ with the E-total cut and the COE cut in a simulation.

Fiducial cut

The hit positions of the two photons on the calorimeter should be outside of 300 mm × 300 mm in xy coordinate. The distance between the hit position and the origin in XY plane should be less than 850 mm. We set the fiducial to be the size of the calorimeter - 3×20 mm (3σ of the radiation length of CsI). We avoid the shower leaks at the edge of the calorimeter.

E-ratio cut

The ratio between the lower and the higher energies of the two photons should be greater than

0.2. We avoid events where an accidental hit participates in the one of two clusters. Figure. A.0.5 shows the energy ratio between two photons from the π^0 in $K_L \to \pi^0\nu\bar{\nu}$. The mean of the energy ratio is 0.47, and the cut value of the E-ratio cut is set to reject two photons which are decayed from $K_L \to \pi^0\pi^0$ [31].

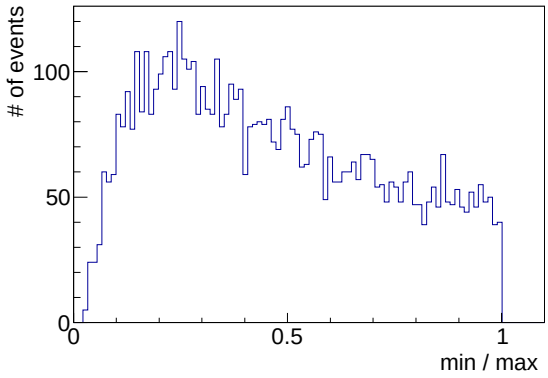

Figure A.0.5: The energy ratio between two photons from the π^0 in $K_L \to \pi^0\nu\bar{\nu}$ with the E-total cut and the COE cut in a simulation.

Projection angle cut

Projection angle is the projected angle between the momenta of the two photons on the surface of the calorimeter in XY plane. Figure A.0.6 shows the projection angle between two photons from the π^0 in $K_L \to \pi^0\nu\bar{\nu}$. The mean of the projection angle is 88 degree, and the projection angle is required to be smaller than 150° in order to reject two photons which are decayed from $K_L \to 2\gamma$ [31].

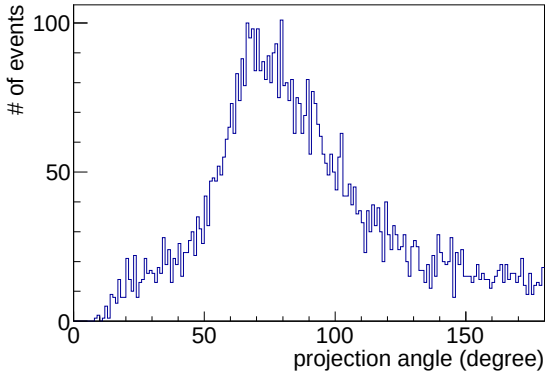

Figure A.0.6: The projection angle between two photons from the π^0 in $K_L \to \pi^0\nu\bar{\nu}$ with the E-total cut and the COE cut in a simulation.

P_t/P_z-Z_{vtx} correlation

P_t is the transverse momentum of the reconstructed π^0, and P_z is the momentum of the reconstructed π^0 in z direction. Z_{vtx} is the decay position of the reconstructed π^0 in the z direction. Figure A.0.7 shows the scatter plot of P_t/P_z versus Z_{vtx} in a simulation of $K_L \to \pi^0\nu\bar{\nu}$. The inner region of the black line in Fig. A.0.7 shows the allowed region. We qualify the two photons from $K_L \to \pi^0\nu\bar{\nu}$ to reject two photons from a η which is generated from the interaction between the CV and neutrons [31].

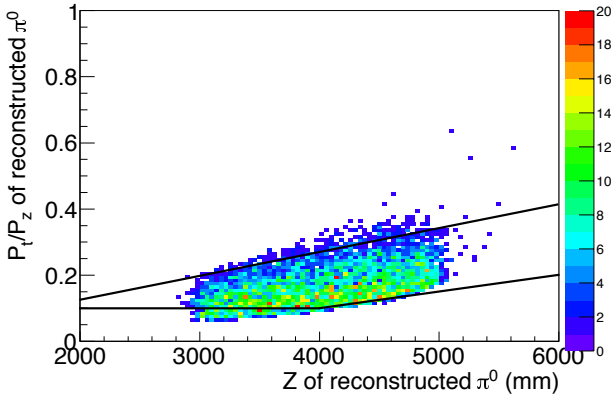

Figure A.0.7: The scatter plot of P_t/P_z versus Z_{vtx} with the E-total cut and the COE cut in a simulation of $K_L \to \pi^0\nu\bar{\nu}$. The inner region of the black line shows the allowed region.

E_π-Z_{vtx} correlation

E_π is the energy of the reconstructed π^0. Figure A.0.7 shows the scatter plot of the E_π versus Z_{vtx} in a simulation of $K_L \to \pi^0\nu\bar{\nu}$. The upper region of the black line in Fig. A.0.7 shows the allowed region. We qualify the two photons from $K_L \to \pi^0\nu\bar{\nu}$ to reject two photons from the η [31].

Single crystal veto

Any activity except for the two clusters should be vetoed in the calorimeter. The cut efficiency for the signal event becomes worse when all the activities are vetoed since the shower leaks from the two clusters are also vetoed. Figure A.0.9 shows the energy of the CsI crystal as a function of the distance between the center of the CsI crystal and the position of the nearest cluster in a simulation of $K_L \to \pi^0\nu\bar{\nu}$. The red line shows the functional energy threshold. The event is rejected when there is a crystal which locates in the upper region of the function in Fig. A.0.9.

Shower quality cut

In a simulation of $K_L \to \pi^0\nu\bar{\nu}$, the scatter plot of the number of crystals which participate in single cluster versus the RMS of the energy weighted position of crystals in single cluster is shown in Fig. A.0.10. The right upper region of the black line shows the allowed region. We apply this cut

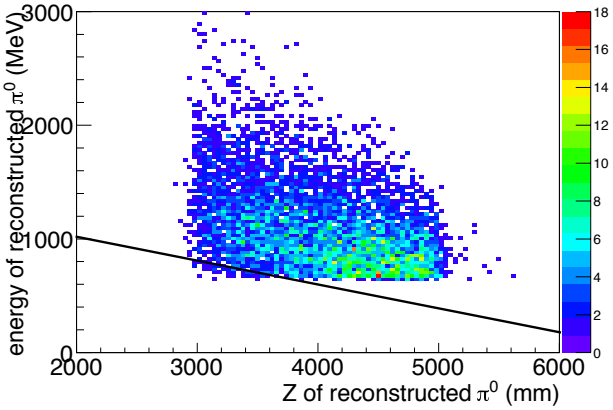

Figure A.0.8: The scatter plot of the E_π and Z_{vtx} with the E-total cut and the COE cut in a simulation of $K_L \to \pi^0\nu\bar{\nu}$. The upper region of the black line shows the allowed region.

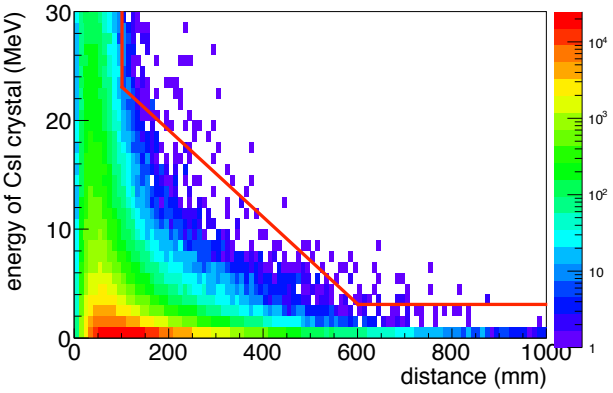

Figure A.0.9: The energy of the CsI crystal as a function of the distance between the center of the CsI crystal and the position of the nearest cluster with the E-total cut and the COE cut in a simulation of $K_L \to \pi^0\nu\bar{\nu}$. The red line shows the functional energy threshold.

to qualify the cluster by the electromagnetic shower.

Cluster-χ^2 cut

The pattern of the energy deposit among the crystals in one cluster is compared with a template which is made from gamma simulations [44]. Figure. A.0.11 shows the normalized χ^2 to the cluster of a photon from the π^0 in $K_L \to \pi^0\nu\bar{\nu}$. The normalized χ^2 is required to be less than 2.5, and the cut value is suitable to qualify the cluster by the electromagnetic shower.

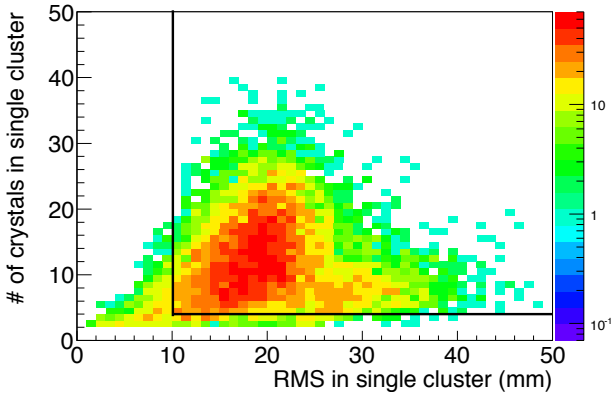

Figure A.0.10: The scatter plot of the number of crystals which participate in single cluster versus the RMS of the energy weighted position of crystals in single cluster with the E-total cut and the COE cut in a simulation of $K_L \to \pi^0 \nu\bar{\nu}$. The right upper region of the black line shows the allowed region.

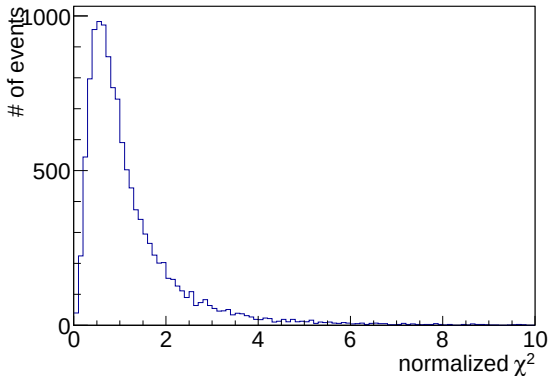

Figure A.0.11: The normalized χ^2 to the cluster of a photon from π^0 in $K_L \to \pi^0 \nu\bar{\nu}$ with the E-total cut and the COE cut in a simulation.

Appendix B

Simulation for the estimation of the requirements

B.1 Estimation of the penetrating BG

The simulation method is the same as described in Sec. 7.2.4. We use Eq. 7.1 to estimate the number of background.

B.2 Estimation of energy deposit

B.2.1 Estimation of energy deposit for the penetrating BG

As mentioned in Sec. 2.3, the energy deposit by charged particles penetrating the CV is almost equivalent to Minimum Ionizing Particle (MIP). Electrons with 500 MeV kinetic energy are then shot to the CV, and the events where the electrons penetrated the CV are collected.

B.2.2 Estimation of energy deposit for the Ke3 BG and the Kπ3 BG

To obtain enough statistics for the estimation, we perform the simulation with three steps: collection of the charged particles hitting the CV, the simulation in the calorimeter, the simulation in the CV.

In the first step of the simulation, the $K_L \to \pi^- e^+ \nu$ decay and the $K_L \to \pi^+ \pi^- \pi^0$ decay are shot from $z = -1000$ mm individually. We put the CV and the Neutron Color Counter (NCC). All the particles hitting the CV are stopped on the surface of the CV. We collect events where at least one charged particle hits the CV with no activities in NCC.

In the second step of the simulation, all the particles stopped on the CV are shot to the calorimeter.

We put the CV, the calorimeter, the Color Counter 03 (CC03), the Color Counter 04 (CC04), and the Outer Edge Veto (OEV). The hits in the calorimeter are formed to clusters in the same way as described in the reference [28], and we reconstruct a π^0 in the same way as described in Sec. 2.1.2. We collect events where the π^0 is successfully reconstructed in the calorimeter with no activities in the veto detectors. Table. B.2.1 shows a list of an energy threshold of the veto detectors. To obtain enough statistics, E-total cut, vertex time cut, γ distance cut, E_γ cut, and fiducial cut are applied to the π^0.

Table B.2.1: summary of the for the energy threshold for the each detector.

	threshold (MeV)
NCC	2
CC03	3
CC04	3
OEV	2

In the third step of the simulation, we estimate the energy deposit of the CV by using the hit informations on the CV recorded in the first step of the simulation. Momentum distribution of the charged particles of the $K_L \to \pi^- e^+ \nu$ decay and of the $K_L \to \pi^- e^+ \nu$ decay are shown in Fig. B.2.1. We shot charged particles to the CV according to Fig. B.2.1, and obtain the energy spectra.

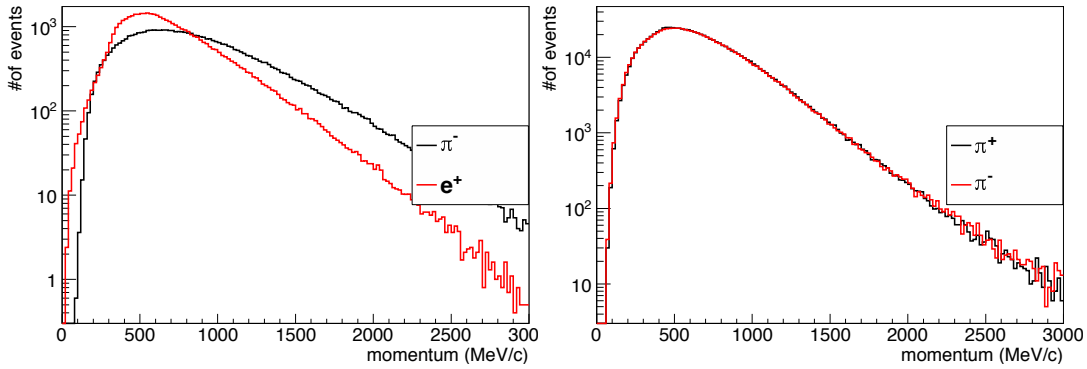

Figure B.2.1: Momentum distribution of the charged particles of the $K_L \to \pi^- e^+ \nu$ decay (left) and of the $K_L \to \pi^+ \pi^- \nu$ decay (right).

B.3 Calculation of a hit timing for a distribution of the hit time difference

The simulation method is same as Sec. B.2.2. We examine the hit timing of the CV strip with energy deposit greater than 100 keV for the hit time of the CV. The hit time of the CV is defined as the hit time of the CV strip that is closest to the hit time of the calorimeter. The hit time on the calorimeter is defined as the energy weighted mean time between two clusters on the calorimeter.

B.4 Calculation of the accidental rate

We estimate the accidental rate of the CV with the designed beam power of KOTO. First, we carry out the target and beamline simulation. After that, the K_L, gammas, and neutrons generated in the target and beamline simulation are shot to all the detectors from z = -1000 mm. Figure B.4.1 shows the energy spectrum of the CV with the accidental hits. The black line shows the energy deposit including all the particles. The red line shows the energy deposit by charged particles from K_L decays. The green line shows the energy deposit by neutrons in the beam. The blue line shows the energy deposit by photons in the beam. In the black and the red plots, two minimum-ionizing peaks corresponding to the two different thickness of the scintillator, which is explained in Sec. 3.2, are seen. The charged particles from the K_L decay dominate the energy spectrum. We normalize the number of the events where the CV has an energy deposit greater than 100 keV (N_{acc}) by the number of spills of the beam injection corresponding to the statistics of the simulation (N_{spill}). N_{acc} is 7673, and N_{spill} is 5.32. The normalized events are then divided by the injection time of the one spill of 0.7 ns.

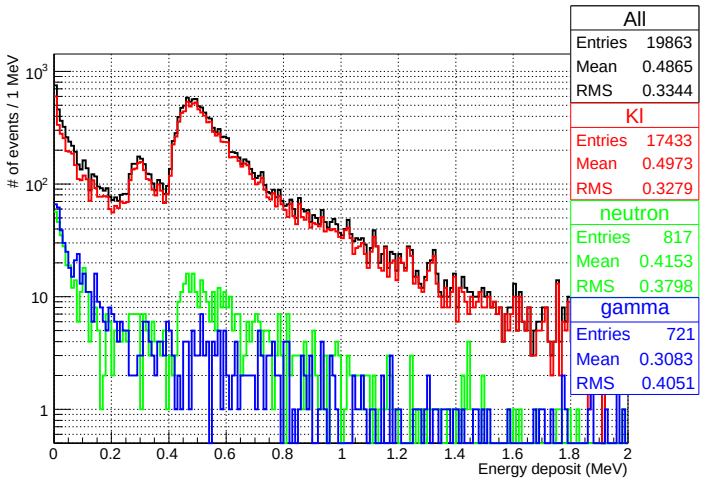

Figure B.4.1: Energy spectrum of the CV with the accidental hits with the designed beam power of KOTO in a simulation.

Appendix C

Detail of the inefficiency analysis

C.1 Energy spectrum of the hodoscope in the simulation for the evaluation of the CV performance

The energy spectrum is corrected with position dependence of a PMT output and the energy resolution obtained from the data. We first calculate the position dependence of the peak value in the distribution of the PMT output of the hodoscope in the same way as the light yield of the CV described in Sec.6.2.1. We separate the extrapolated position on the hodoscope into every 10 cm $\times$ 5cm region. We calculate a energy peak in each region. Figure C.1.1 shows the position dependence of the peak value. The Z axis shows the ratio of the peak in each region to the peak with the whole data. The energy deposit is corrected by this ratio. The energy spectrum is then corrected by using energy resolution as shown in Fig.C.1.2. We adjust parameters of a Gaussian and Poisson function, and the energy spectrum is smeared by this functions. In this figure, the energy deposit of the hodoscope (E_{Hod}) is smeared by the Poisson function whose mean is $E_{Hod}\times$6.7 p.e./MeV and the Gaussian whose sigma is $0.1\times\sqrt{E_{Hod}}$.

C.2 Calculation of the systematic uncertainty for the inefficiency measurement of the CV

C.2.1 Systematic uncertainty by the CVR Cut to $C_{\mathrm{n.p}}$

$C_{\mathrm{n.p}}$ is affected by the systematic uncertainty of the CVR Cut. We consider systematic uncertainties caused by the uncertainty of the position resolution and the misalignment in the CV.

The position resolution of the extrapolated position on the CV is shown in Fig. C.2.1. This position resolution is the sigma of the fitting function which is evaluated in Sec. 6.1.2. The horizontal axis shows the center of y (x) in each 5-cm step as defined in Sec. 6.1.2. The vertical axis shows the position

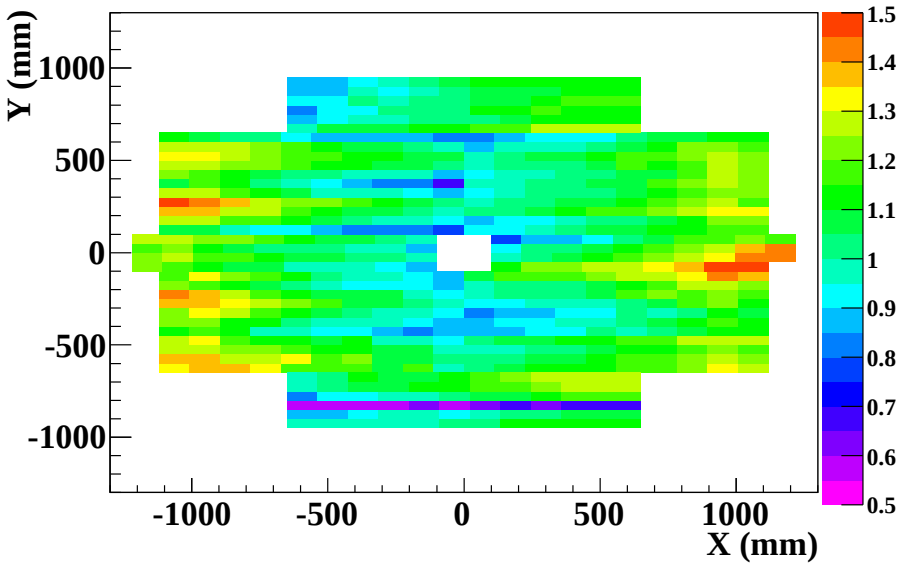

Figure C.1.1: Position dependence of the peak value in the distribution of the PMT output of the hodoscope.

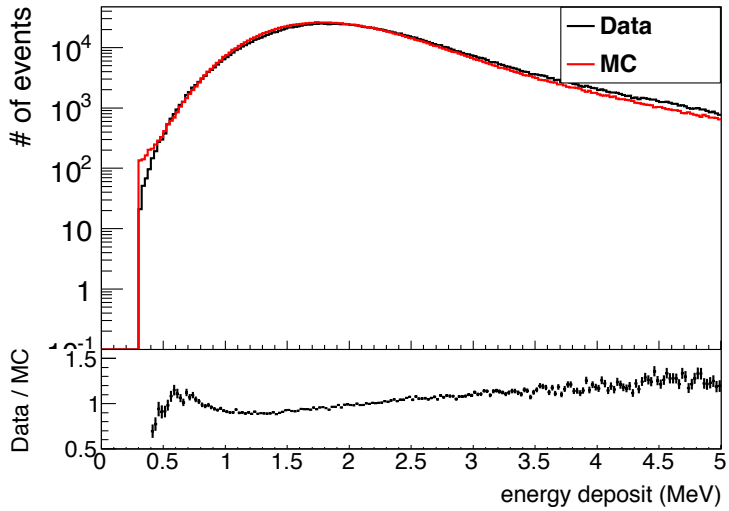

Figure C.1.2: Energy spectrum after the smearing of a Gaussian and Poisson distribution.

resolution. The left plot shows that in x direction, and the right plot shows that in y direction. The black points show the position resolution of the data. The red points show that of the MC. There is position dependence on the resolution stemming from an effect of multiple scattering. The detail of the mechanism is described in the last of this chapter. The maximum difference of the position resolution

between the data and the simulation is 0.5 mm in CVR < 720 mm [1)].

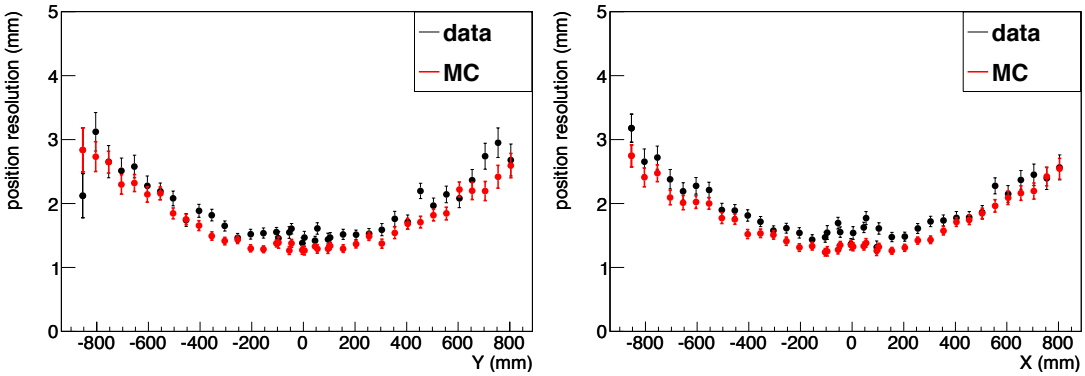

Figure C.2.1: Position resolution of the extrapolated hit position on the CV. The left plot shows that in x direction, and the right plot shows that in y direction.

We check the position where the CV locates as the uncertainty of the misalignment. The maximum difference of the center position in the same strip is ±1 mm as shown in Fig. 6.1.3, while the CV in the simulation is not considered these difference. We define ±1 mm as systematic uncertainty of the misalignment.

We change the cut value of the CVR from 199 mm to 200 mm, and evaluate the variation of the $C_{\mathrm{n.p}}$.

C.2.2 Systematic uncertainty by the ΔR cut to $C_{\mathrm{n.p}}$

$C_{\mathrm{n.p}}$ is affected by the systematic uncertainty of the ΔR cut. We consider systematic uncertainties caused by the uncertainty of the position resolution.

The difference between the extrapolated position and the clustering position on the calorimeter is shown in Fig. C.2.2. The left plot shows the difference in x direction, the right plot shows the difference in y direction. We define the σ of these distribution [2)] as the position resolution. The sigma in the x direction is 11.7±0.02 mm for the data and 11.8±0.02 mm for the simulation, and the sigma in the y direction is 11.5±0.01 mm for the data and 11.9±0.02 mm for the simulation. The difference of the sigma between the data and simulation is 0.13 ± 0.028 mm in x direction, and 0.43 ± 0.022 mm in y direction. We then define ±0.45 mm [3)] as the systematic uncertainty by the position resolution.

We change the cut value of the ΔR from 29.55 mm to 30.45 mm, and evaluate the variation of the $C_{\mathrm{n.p}}$.

[1)] CVR is limit in this region as described in Sec.6.5.4.
[2)] We fit Fig. C.2.2 with a Gaussian function, evaluate the difference of the sigma.
[3)] $= \sqrt{0.13 \times 0.13 + 0.43 \times 0.43}$

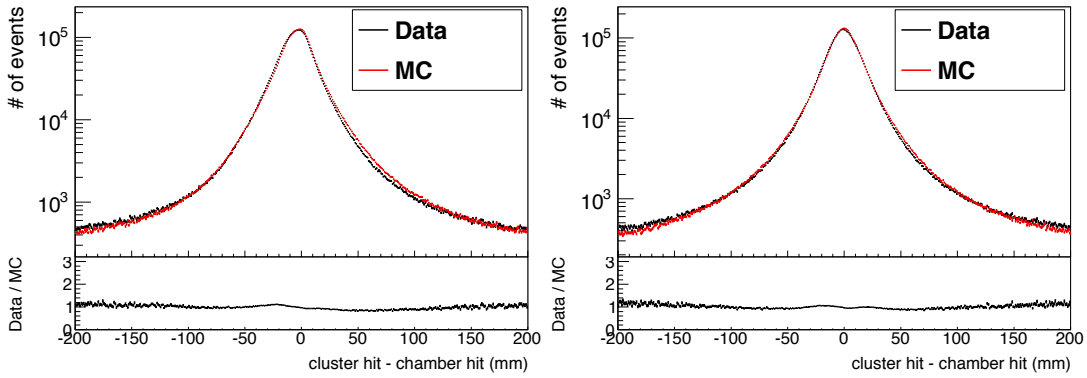

Figure C.2.2: The difference between the extrapolated position and the clustering position on the calorimeter. The left plot shows the difference in x direction, the right plot shows the difference in y direction.

C.2.3 Mechanism of the position dependence of the position resolution

The momentum distribution of the charged particles hitting the CV as a function of the hit position of the charged particles on the surface of the CV in the simulation is shown in Fig. C.2.3. The horizontal axis shows the distance between the beam center and the hit position of the charged particles on the surface of the CV obtained from the true information of a charged particle. The vertical axis shows momentum of the charged particle. When the momentum of the initial kaon is small, the boost factor of the charged particles is small and the angle from the beam direction becomes large. As a result, the momentum becomes smaller in the outer region. When the momentum is small, the effect of multiple scatter becomes larger. From these reason, the position resolution becomes worse as a function of radius.

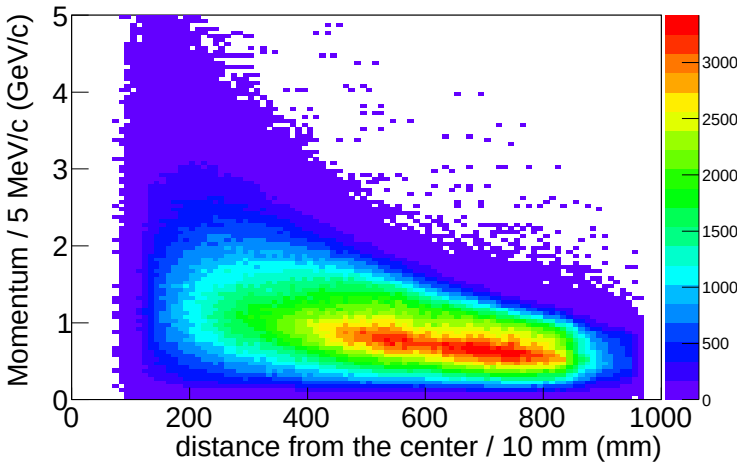

Figure C.2.3: The momentum distribution of the charged particles hitting the CV as a function of the hit position of the charged particles on the surface of the CV in the simulation.

Bibliography

[1] A.D.Sakharov, Pizma ZhETF, **5**. 32 (1967).

[2] M. Kobayashi and T. Maskawa, Prog. Theor. Phys. **49**, 652 (1973).

[3] G.R. Farrar and M.E. Shaposhnikov, Phys. Rev. D **50**, 774 (1994).

[4] J.K. Ahn, et al., E391a Collaboration, Phys. Rev. D **81** 072004 (2010).

[5] E. Abouzaid et al., Phys. Rev. D **83**, 092001 (2011).

[6] V. V. Anisimovsky et al. (E949), Phys. Rev. Lett. **93**, 031801 (2004).

[7] Monika Blanke. New Physics Signatures in Kaon Decays. volume PoS.(KAON13)010. Proceedings of 2013 Kaon Physics International Conference, SISSA, May 2013.

[8] Andrzej J. Buras, Dario Buttazzo, Jennifer Girrbach-Noe, and Robert Knegjens, JHEP **1511** (2015) 033, hep-ph/1503.02693.

[9] Japan Proton Accelerator Research Complex, http://j-parc.jp. Web. 6 March. 2015.

[10] Lincoln Wolfenstein. Parametrization of the Kobayashi-Maskawa Matrix. Phys. Rev. Lett. **51**, (1983).

[11] Andreas Hocker, Zoltan Ligeti, CP violation and the CKM matrix, hep-ph/0605217.

[12] F. Mescia and C. Smith, Phys. Rev. D **76**, 034017(2007)

[13] J. Brod, M. Gorbahn, and E. Stamou, Phys. Rev. D **83**, 034030 (2011).

[14] Y.Grossman and Y.Nir, Phys. Lett. B**398**, 163 (1997).

[15] David M. Straub, New physics correlations in rare decays, hep-ph/1012.3893.

[16] M. Blanke, A. J. Buras, B. Duling, S. Recksiegel and C. Tarantino, Acta Phys. Polon. B**41** (2010) 657, hep-ph/0906.5454.

[17] M. Blanke et. al., Rare and CP-violating K and B decays in the Littlest Higgs model with T-parity, JHEP **01** (2007) 066, hep-ph/06102982.

[18] Monika Blanke, Andrzej J. Buras, Bjoern Duling, Katrin Gemmler, Stefania Gori, JHEP **0903** (2009) 108, hep-ph/0812.3803.

[19] Andrzej J. Buras et al., JHEP **09** (2010) 106, hep-ph/1002.2126.

[20] Tobias Hurth, Gino Isidori, Jernej F. Kamenik, and Federico Mescia, Nuclear Physics B, **808**(1-2):326-346 (2009).

[21] Monika Blanke. New Physics Signatures in Kaon Decays. volume PoS.(KAON13)010. Proceedings of 2013 Kaon Physics International Conference, SISSA, May 2013.

[22] L. S. Littenberg, Phys. Rev. D **39**, 3322 (1989).

[23] T. Yamanaka, for the KOTO Collaboration, Progress of Theoretical and Experimental Physics **2012** 02B006 (2012).

[24] Proposal for$K_L \to \pi^0 \nu\bar{\nu}$ Experiment at J-PARC.

[25] K. Shiomi. Measurement of KL flux at the J-PARC neutral-kaon beam line for the $K_L \to \pi^0 \nu\bar{\nu}$ experiment. PhD thesis, Kyoto University, 1 2012.

[26] R. Murayama, "Main Barrel upgrade" the slide prepared for the KOTO informal domestic meeting at 12th May, 2012, password protected, contact person: R. Murayama, Physics Department, Osaka University, Toyonaka, Osaka 560-0043, Japan.

[27] T. Shimogawa, Nuclear Instruments and Methods in Physics Research Section A **623** 585 (2010).

[28] T. Masuda. Development and Experimental Study of the KOTO Detector System using Three K_L Neutral Decay Modes. PhD thesis, Kyoto University, 1 2013.

[29] K. Sato. Measurement of the CsI calorimeter performance and K_L momentum spectrum for the J-PARC KOTO experiment. PhD thesis, Osaka University, 1 2015.

[30] J. Beringer et al.(PDG). Phys. Rev. D **86**, 010001 (2012).

[31] K. Shiomi. Master thesis (in Japanese), Kyoto University, 2008 (in Japanese).

[32] Saint-Gobain,
http://www.crystals.saint-gobain.com .

[33] KURARAY Co., LTD.,
http://www.kuraray.co.jp/en/ .

[34] Hamamatsu Photonics K. K.,
http://www.hamamatsu.com/jp/en/index.html .

[35] Oike & Co., Ltd.,
http://www.oike-kogyo.co.jp/english/index.html .

[36] Hamamatsu Photonics catalog, Cat. No. KAPD0002J05, Aug. 2009.

[37] ELJEN Technology,
http://www.eljentechnology.com/index.php .

[38] "HAMAMATS OPTO-SEMICONDUCTOR HANDBOOK", chapter03, p3, figuer 1-1.

[39] Y. Maeda, "work reports" the slide prepared for the KOTO informal domestic meeting at 12th Dec, 2011, password protected, contact person: Y. Maeada, Kobayashi-Maskawa Institute, Nagoya University, Nagoya 464-8602, Japan.

[40] D. Naito. Master thesis (in Japanese), Kyoto University, 2010 (in Japanese).

[41] M. Bogdan, et al., in Nuclear Science Symposium Conference Record, Honolulu, HI, 2007, NSS Ó7, vol. 1, IEEE, pp. 133–134; M. Bogdan, et al., in 16th IEEE-NPSS Real Time Conference, RT Ó9, 2009, pp. 443–445.

[42] K. Shiomi., Proceedings of the 8th International Workshop on the CKM Unitarity Triangle (CKM 2014), Vienna, Austria, September 8-12, 2014

[43] E. Iwai. CsI calorimeter fot the J-PARC KOTO experiment. PhD thesis, Osaka University, 10 2012.

[44] K. Sato. CsI Calorimeter for KOTO experiment. In Calorimetry for High Energy Frontiers - CHEF 2013, 2013.